UNIVERSITEIT VAN PRETORIA
UNIVERSITY OF PRETORIA
YUNIBESITHI YA PRETORIA

The effect of ternary alloying on the shape memory properties of titanium-platinum alloys

By

Pfarelo Daswa

Supervised by

Prof C.W. Siyasiya and Dr S. Chikosha

Dissertation submitted in partial fulfilment of the requirements for the degree
Master of Engineering (Metallurgical Engineering)

In the

Department of Materials Science and Metallurgical Engineering

Faculty of Engineering, Built Environment and Information Technology

UNIVERSITY OF PRETORIA

Pretoria

Republic of South Africa

August 2020

Preface:

This dissertation is submitted for the degree of Master in Engineering (Metallurgical) in the Faculty of Engineering, Built Environment and Information Technology at the University of Pretoria.

The text contained herein is, to the best of my knowledge, the result of my own work, except where acknowledgements and references have been made to previous work done by other researchers. It has not been submitted before for any degree or examination in any other University.

Acknowledgements

Firstly, I would like to thank the Almighty God for being my pillar of strength and providing me with good health throughout my studies. I would like to acknowledge the support, assistance and motivation of almost everyone I know. To all my friends and family for keeping me inspired and helping out in any way possible. To the CSIR staff, for motivating and being extremely helpful throughout the journey

To my supervisors, Prof C.W. Siyasiya and Dr S. Chikosha for the initiation of this project and constructive guidance, advice, encouragement, life coaching, supervision and valuable inputs into this research project and making it possible to be published. They were wonderful supervisors, and always available. I learnt a lot from them, including technical and communication skills, professional practice from their experiences and insight during this work, for that I thank you so much.

I would like to thank the School of Materials Science and Metallurgical Engineering at the University of Pretoria for taking me on as a part-time student. I would like to thank CSIR for granting me the opportunity to do this dissertation part-time and thank them for their wonderful facilities and incredible staff. I would like to thank my manager, Dr Sagren Govender for his support and encouragement.

Thanks to the CSIR personnel: Ndumiso Mnguni, Prof Ronald Machaka, Stephen Masete, Mandy Seerane, Dr Kalenda Mutombo, Dr Sylvester Bolokang, Pierre Rossouw and Zizo Gxowa-Penxa for assistance and advice. Most special thanks to Ms Linda Mahlatji for the consistent support, assistance and advices on the work.

Special thanks to my mom, for the unconditional support towards my studies. This dissertation is proudly dedicated to you. To my family and friends for the constructive support and words of encouragement.

I would like to acknowledge the AFSOR for funding this work through the US Air Force Office of Scientific Research (Programme Manager Ali Sayir on Award FA9550-16-1-0253).

Abstract

Among many shape memory alloys, Ti-Pt alloys have potential as a high temperature shape memory alloy. The alloy undergoes a reversible martensitic transformation at temperatures above 1000 °C. However, the alloy's negligible shape memory effect could limit its application. Solid solution strengthening has been suggested as an alternative to improve the shape memory properties of Ti-Pt. In this study, the effect of partially substituting either platinum (Pt) or titanium (Ti) with vanadium (V) on the shape memory properties of Ti-Pt was investigated in the as-cast and solution heat treated conditions. The study focused on investigating the effect of V on the structure, phase transformation, mechanical properties and shape memory behaviour of Ti-Pt alloy using scanning electron microscope with an energy dispersive spectrometer (SEM-EDS), X-ray diffraction analysis (XRD), differential scanning calorimeter (DSC), compression tests and a macro Vickers hardness tester. Ti-Pt$_{50-x}$-V$_x$ and Ti$_{50-x}$-V$_x$-Pt (x = 0, 6.25, and 12.5 at.%) alloys were produced by an arc melting method using elemental powders of Ti, Pt and V. Solution heat treatment (SHT) was carried out at a temperature 1250 °C for 72 hours, followed by ice water quenching.

The SEM-EDX revealed that the addition of V to Ti-Pt resulted in multiple phase microstructures in both the as-cast and solution heat treated conditions. The partial substitution of Pt with V did not occur, since the alloy composition was within in a three-phase region of the Ti-Pt-V ternary phase diagram with increasing V content. Solution heat treatment increased the amounts and size of the other phases with increasing V content. The partial substitution of Ti with V resulted in alloy compositions that were in a single TiPt phase region. The addition of 6.25 and 12.5 at.% V did not change the structure of B19 martensite phase and this phase was the major matrix phase in all compositions.

The partial substitution of Pt with V decreased the transformation temperatures of the Ti(Pt,V) phase with increasing V content, while the partial substitution of Ti with V increased the transformation temperatures of (Ti,V)Pt phase with increasing V content. Both substitutions widened the thermal hysteresis compared to TiPt, with Ti(Pt,V) exhibiting the highest.

For mechanical properties, the addition of V to Ti-Pt exhibited a single yielding behaviour and, the yield strength and hardness of Ti-Pt were significantly increased with the increasing V content. Ternary alloying with V degraded the ductility and plastic strain of Ti-Pt-V with increasing V content. The partial substitution of Pt with V did not improve the shape memory effect and shape recovery of Ti-Pt-V in the as-cast condition. However, the partial substitution of Ti with 6.25 at.% V improved the shape memory effect and shape recovery of Ti-V-Pt in the as-cast condition. The SHT improved the shape recovery of Ti-Pt-V and Ti-V-Pt alloys with increasing V content, but were still lower than in the as-cast condition.

Table of Contents

List of Figures

List of tables

List of Equations

List of Abbreviations

A – Austenite
M – Martensite
BCC –Body centred cubic
SMAs – Shape memory alloys
HTSMAs – High temperature shape memory alloys
MT – Martensite transformation
OM – Optical Microscopy
XRD – X-ray diffraction
SEM –Scanning electron microscopy
EDS – Energy dispersive X-ray spectrometer
DTA –Differential thermal analysis
DSC –Differential scanning calorimetry
TEM –Transmission electron microscopy
HRTEM – High-resolution transmission electron microscopy
SHT – Solution heat treatment
SME – Shape memory effect
SIM – Stress induced martensite
VGC – Variable geometry chevron
TWSME – Two way shape memory effect
TRIP – Transformation Induced Plasticity
DFT – Density functional theory
L - Liquid
PGMs – Platinum group metals
LP – Low period structure
SMM –Shape memory strain
SRR – Strain recovery ratio
VHN – Vickers hardness
SRR – Shape recovery ratio
BEI – Backscattered electron imaging / image
SEI – Secondary electron imaging/image
SRR – Strain recovery ratio

List of Symbols

Ti – Titanium
Pt – Platinum
V – Vanadium
Cu – Copper
Ni – Nickel
Co - Cobalt
Zr – Zirconium
Pd – Palladium
Au – Gold
Ar – Argon
He – Helium
Ru – Ruthenium
Al – Aluminium
Cd – Cadmium
Cl - Chloride
Zn – Zinc
Nb – Niobium
Fe – Iron
Si - Silicon
β – Beta
α –Alpha
γ – Gamma
σ_y – Yield strength
σ_{det} – Detwinning stress
σ_f – Fracture strength
A_s –Austenite start temperature
A_f – Austenite finish temperature
M_s – Martensite start temperature
M_f – Martensite finish temperature
ΔT – Transformation thermal hysteresis
ΔH – Latent heat of transformation
$\Delta G^{a\text{-}m}$ – Free energy for martensite transformation
$\Delta G^{m\text{-}a}$ – Free energy for austenite transformation
ΔG_c – Chemical free energy
ΔE_e – Elastic strain energy
$\Delta E_i^{a\text{-}m}$ – Undercooling energy for martensite transformation
$\Delta E_i^{m\text{-}a}$ – Superheating energy for austenite transformation
C_v – Concentration of valence electrons

^{o}C – Degree Celsius
K – Kelvin
ε_{sme} – Shape memory strain
ε_{irr} – Irrecoverable strain
ε_{p} – Plastic strain
B2 – Lattice notation for austenite parent phase
B19 – Lattice notation for martensite phase

List of Publications

Conferences

- Daswa P., Chikosha S., Mahlatji M.L., Siyasiya C.W. 2019. The effect of ternary alloying with vanadium on Ti-Pt shape memory alloy. Conference of South African Advanced Materials Initiative (CoSAAMI), Vaal, South Africa, 15-18 October 2019

- Daswa P., Chikosha S., Mahlatji M.L., Siyasiya C.W. 2020. Comparative study of transformation behaviour of (Ti43.75V6.25)Pt and Ti(Pt43.75V6.25) ternary alloys. ICOMAT, To be held at Jeju, Korea on 11-16 July 2021

Journal

- Daswa P., Chikosha S., Siyasiya C.W. 2020. Shape memory properties of Ti-V-Pt alloy. Submitted to Intermetallics Journal, August 2020

CHAPTER 1: INTRODUCTION

1. INTRODUCTION

1.1. Background of the study

The high demand for smart materials has attracted much research for their application in industries such as the biomedical, automotive and aerospace. Smart materials (also called intelligent or stimulus responsive materials) are materials that change their physical properties due to a change in temperature, stress and electrical field/ magnetic field [1,2]. The change is reversible and happens because the structure of the material undergoes a transformation from a high temperature cubic structure to a low temperature martensitic structure. This characteristic offers the opportunity for their use as sensors and force actuators since they are able to convert one type of energy to another.

Shape memory alloys (SMAs) are a type of smart materials that are stimulated to change between shapes by a change in temperature. They are thermo-responsive materials that can hold different shapes at varying temperatures such that they can be deformed and returned to the original predeformed shape by heating. Currently, the commercially available and successful shape memory alloy is Nitinol (Ni-Ti). Nitinol is attractive in the medical, biomedical, automotive and aerospace industries due to good corrosion resistance, biocompatibility, good workability, superior shape memory and pseudoelasticity [3–5]. Nitinol is used to make superelastic spectacle frames and stents for veins in the medical and biomedical industry [6]. Nitinol is used in actuation for smooth gear shifting in automatic motor vehicles in the automotive industry [6]. In the aerospace industry, Boeing Company developed a variable geometry chevron (shape memory alloy-actuated morphing aero-structure, also known as VGC) using Nitinol and has been installed on a jet engine for Boeing 777-330 ER commercial aircraft [7,8]. Previously, airplanes with larger exhaust nozzles produced minimum noise but less efficiency in cruise mode. Boeing installed a variable geometry chevron on the jet engine for noise reduction in aeroplanes during take-off by maximising the chevron deflection and also increasing the cruise efficiency by minimising the chevron deflection [7-9]. The above-mentioned applications of Nitinol are at temperatures lower than 100 °C.

There is a need for shape memory alloys for high temperature applications of over 100 °C where Ni-Ti alloy does not suffice. To increase the application temperature, research on alloying of this binary system has been ongoing ranging from ternary through to quinary additions [4,10–13]. Some Ni-Ti alloys that have more than 4 elements have been studied as multicomponent or high entropy alloys [11]. Macro-additions of hafnium (Hf), zirconium (Zr), palladium (Pd), platinum (Pt) and gold (Au) have shown to increase the martensitic transformation temperatures when replacing either Ni, Ti or both [3,10–16]. To date, the maximum martensitic transformation temperature for the Ni-Ti based alloys achieved still remains below 750 ^{o}C, which still limits their application in the aerospace industry where higher temperatures are needed [11,17,18].

For application temperatures of approximately 1000 ^{o}C, titanium-platinum (Ti-Pt) alloys have been identified as potential candidates due to their high transformation temperature of about 1050 ^{o}C [12]. However, the alloy possesses negligible shape memory effect (SME) behaviour and the high cost of Pt may limit its practical application as a high temperature shape memory alloy [19]. Alloying Ti-Pt by partial substitution of Ti or Pt could be an alternative of improving its functional properties. Partial substitution for Pt with cheaper metals could have an added advantage of lowering the cost of the alloys [12,20,21]. Ternary additions of ruthenium (Ru), Hf and cobalt (Co) while replacing for Pt with less than 7 at.%, have shown to decrease the martensitic transformation temperature of the Ti-Pt alloy to below 1000 ^{o}C [15-16], except for iridium (Ir) [20,22,23]. In addition, the partial substitution of Ti with either Zr and Hf decreased the martensitic transformation temperature of the Ti-Pt alloy to below 1000 ^{o}C [20,24]. However, these transformation temperatures were above that of alloyed Ni-Ti alloys, which qualifies them for possible applications between 750 and 1000 ^{o}C if required functional properties were to be achieved. There is not much work done to consider the effect of increasing the amount of ternary alloying elements beyond 7 at.% on the functional properties of the Ti-Pt binary alloy.

1.2. Research problem

The negligible shape memory effect and high cost of Pt may limit the practical application of the binary Ti-Pt alloy. Hence, the need to improve the SME while reducing the cost of these alloys.

1.3. Aim of the study

The aim of this study was to investigate the effect of ternary alloying Ti-Pt with varying contents of vanadium (V = 0-18.25 at.%) on the shape memory properties of the alloy while replacing either Pt or Ti, thereby reducing the cost of Pt if the Pt replacement achieves better functional properties.

1.4. Scope of the study

The scope of this research was to investigate the effect of increasing ternary alloying with V on the shape memory properties of the Ti-Pt alloy. Vanadium replaced both Ti and Pt during ternary alloying. The effect of the resulting microstructures (phases, compositions), crystal structure, thermal behaviour (transformation temperature, hysteresis and latent heat), mechanical and shape memory properties of the ternary alloy were studied. The alloys were processed by arc melting, and both the as-cast and solution heat treated conditions were investigated by comparing the ternary alloys to the binary Ti-Pt.

CHAPTER 2: LITERATURE REVIEW

2. Literature Review and Background

2.1. History of shape memory alloys (SMAs)

Shape memory alloys have a memory that remembers their original shape after deformation, when heated above the martensitic transformation temperature. Heating above the martensitic transformation temperature can result in shape recovery, even under high applied loads. This shape memory behaviour makes them very attractive for the aerospace, biomedical, automotive and oil industries where they can be used as actuators, pipe couplings and sensors [25]. The first shape memory effect behaviour was discovered by a Swedish metallurgist Olander who reported a unique "rubber like effect" behaviour on gold-cadmium (Au-Cd) alloys at a Swedish Metallurgical Society meeting in May 1932 using metallographic observations and resistivity changes [26,27]. Benedicks did further investigation on this alloy in 1940 and Bystrom and Almin studied it in 1947. Many years later in 1951 after the discovery of shape memory behaviour in Au-Cd alloy, Chang and Read [28] reported that a Au-Cd straight rod having a cubic phase acquired a different shape while cooled through the transformation under stress. However, the latter disappeared and the rod straightened again when heated into the cubic phase [28]. In 1938, Greninger and Mooradian [29] reported the shape memory behaviour in copper-zinc (Cu-Zn) alloys. Kurdjumov and Khandros [30] then experimentally observed the shape memory behaviour in Cu-Zn and Cu-Al alloys in 1949 and in In-Tl alloys by 1953 [25,30,31] .

Although these shape memory characteristics were observed early, shape memory alloys only attracted much research after the observation of the shape memory behavior in Ni-Ti alloys, also known as Nitinol, by Buehler and co-workers in 1963 while investigating materials useful for heat shielding [32]. The strong research interest of this alloy was due to good mechanical properties, shape memory effect capability, biocompatibility and good corrosion resistance [26,31,33]. The discovery of Ni-Ti alloys led to many research studies focusing on the effect of composition, heat treatments and microstructure on the shape memory properties of the alloy. Its low transformation temperatures of up to a maximum of 100 ^{o}C brought forth the idea of the addition of a third alloying element such as Co, Nb and Fe, hoping to increase the transformation temperature so that the alloy can be used for high temperature applications [31]. However, the transformation temperatures were enormously decreased to a point where no actuation occurred [31].

In the early 1970s, high temperature shape memory alloys (HTSMAs) such as the titanium-palladium (Ti-Pd), titanium-platinum (Ti-Pt) and titanium-gold (Ti-Au) with transformation temperatures above 100 °C were developed [31]. All these had transformation temperatures above that of the Ni-Ti alloys and this made them potential alloys for applications at higher operating temperatures in aerospace, automotive and oil industries. These alloys continue to attract much research to date [14,17,26–30]. Of all three alloys, Ti-Pt showed the highest transformation temperature of about 1070 °C [25], Figure 2.1.1.

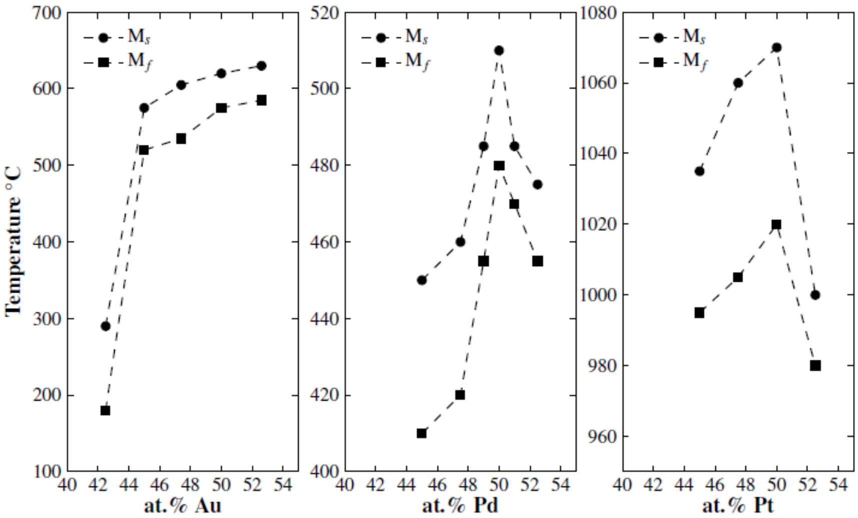

Figure 2.1.1 : The martensitic transformation temperatures of Ti-Au, Ti-Pd and Ti-Pt binary alloys at varying compositions [25].

2.1.1. Thermoelasticity of shape memory alloys

Martensite transformations are displacive, shear–dominant solid-to-solid state phase transformations where atoms carry out a cooperative movement resulting in a change in lattice structure and a shape change with respect to temperature [38,39]. During the transformation, martensite plates/needles form in the matrix along a plane of contact between the two phases (austenite and martensite) and this plane separates the austenite from the martensite phase. The latter is an undistorted plane, called a habit plane. Shear is produced by either slip or twinning along the habit plane during the transformation.

When slip occurs in a crystal, the crystal planes glide over each other, which make it impossible to return the crystal into its exact original structure, making it an irreversible process. Metals or alloys that display the latter property are associated with non-mobile martensite-austenite interfaces pinned by permanent structural defects [38]. They do not exhibit the shape memory behavior and they undergo non-thermoelastic martensite transformations. Crystal structures that show twinning and very little slip have a capability to exhibit the shape memory behavior, where there is a coordinated motion of planes of atoms in a lattice. This movement is parallel to a specific plane such that the lattice is divided into two symmetrical parts possessing a mirror image of each other producing twin martensite variants (twinning plane) [39]. Metals or alloys that exhibit this property are associated with mobile interfaces between the martensite and austenite phases which makes them capable of going back to their original shape upon heating by shrinkage of the martensite plates, known as a reversible process. The latter undergoes a thermoelastic martensite transformation, which is a unique property of shape memory alloys. Thermoelastic transformations or thermoelasticity is a transformation in which martensite plates grow or shrink with respect to change in temperature (lowered or increased). The transformation is reversible and produces a volumetric and a shear strain along defined planes. Stress and temperature play a significant role on the martensitic transformation. Thermoelastic martensitic transformations were first observed by Kurdjumov *et al.* [40] on Au-Cd shape memory alloys.

2.2. Crystal structure of shape memory alloys

Shape memory alloys usually consist of two phases, each with a different crystal structure: a cubic high temperature austenitic phase and a low temperature martensitic phase that has either a tetragonal, orthorhombic or monoclinic crystal structure, Figure 2.2.1. The transformation from one structure to the other is a diffusionless process involving the rearrangement of atoms within the crystal lattice. The main characteristic of this transformation is that it is a displacive transformation involving the shearing or displacing of atoms to create a significant increase of the new phase in an instant [41]. When a shape memory alloy undergoes a martensitic transformation, it transforms from its high temperature cubic austenitic phase to a low temperature martensitic B19′monoclinic / B19 orthorhombic phase by shear distortion [27,31], Figure 2.2.1. The transformed martensite structure can have different orientation directions which are called variants [31]. These martensitic variants can exist as twinned and detwinned martensite. Twinned martensite is a combination of self-accommodated martensitic variants and detwinned/reoriented martensite takes place when a specific variant is dominant where certain variants grow at the expense of others by means of a moving interface with the application of shear stress [31].

Martensitic transformations take place by a shear mechanism where the parent B2 structure shears along a particular direction to give a martensite phase [25]. The high temperature B2 cubic structure is associated with right angles of 90° ($\alpha = \beta = \gamma$) and same values of lattice parameters ($a = b = c$). Shear takes place in the closest packed plane and direction which is the (111) plane and [110] direction for the Ti-Pt alloys [25,36]. The resultant crystal structure due to shearing can be orthorhombic, tetragonal or monoclinic martensite at low temperatures. If the resultant low temperature structure is orthorhombic (two-fold symmetry), then, the angles of the unit cell will still be right angles but the values of the lattice parameters will be different ($a \neq b \neq c$).

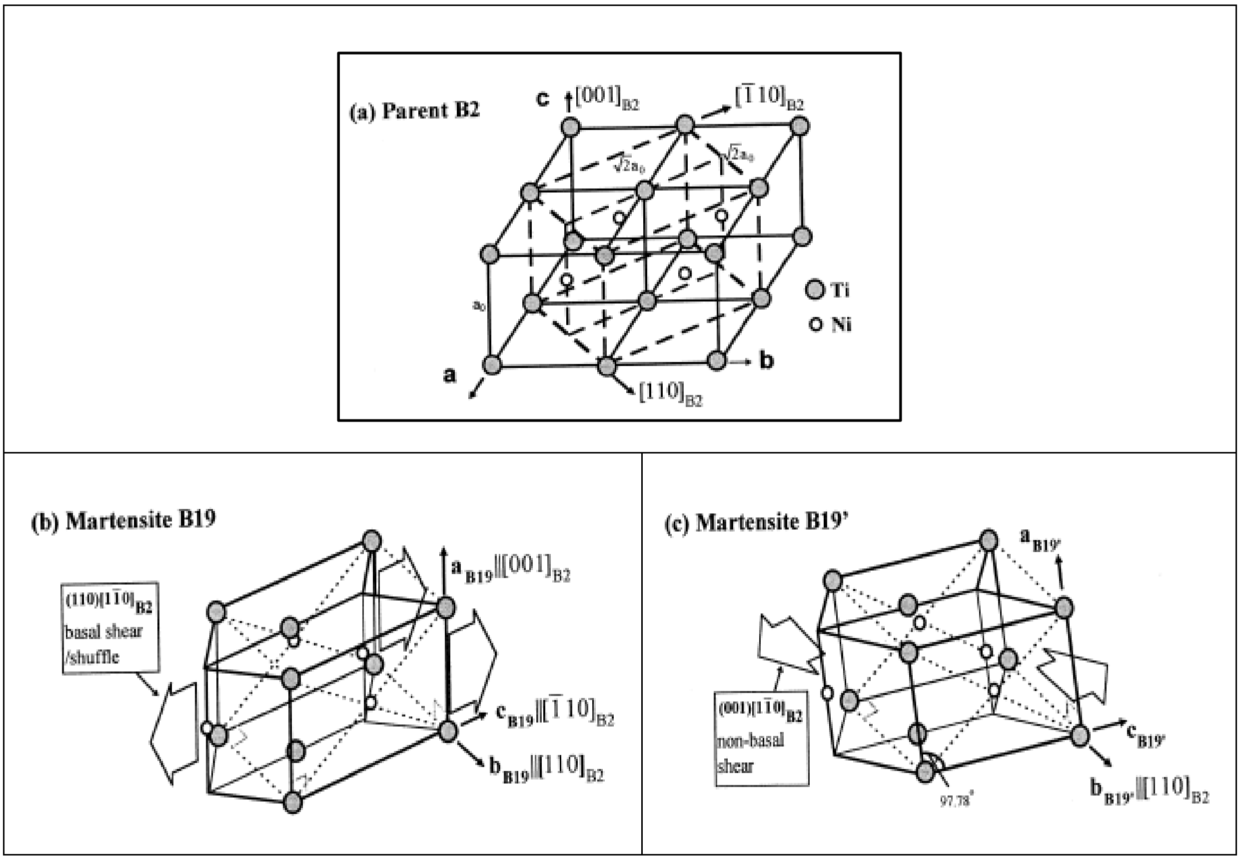

Figure 2.2.1 : Transformation relationship between the parent B2-austenite phase and B19 /B19’ martensite phase [25, 42].

The phase transition from austenite to martensite crystal structure during cooling is known as a forward transformation and the transition from martensite to austenite structure during heating is a reverse transformation. Transformation behaviours of shape memory alloys can be analysed and characterised by various techniques such as mechanical testing, electrical resistance measurements, differential thermal analysis (DTA), differential scanning calorimetry (DSC), internal friction measurements and microscopic observations [16,17].

2.2.1. Thermodynamics of shape memory alloys

The thermodynamics of the transformation in shape memory alloys is described using Figure 2.2.2. The thermoelastic transformation can be controlled by a free energy balance expressed as [25,43]:

$$\Delta G^{a-m} = \Delta G_C^{a-m} + \Delta E_e^{a-m} + \Delta E_i^{a-m} \qquad (2.1.1)$$

$$\Delta G^{m-a} = \Delta G_C^{m-a} + \Delta E_e^{m-a} + \Delta E_i^{m-a} \qquad (2.1.2)$$

In the equations, ΔG_c is the chemical free energy change associated with the transformation. ΔE_e is the non-chemical part of the transformation, which involves the elastic strain energy involved in the transformation, and ΔE_i is the irreversible energy consumed during the transformation, related to undercooling and superheating for the martensitic transformation in the forward and reverse reaction.

During thermoelastic transformations, the elastic strain energy is stored in the system during the forward reaction with the increasing volume fraction of the martensite and released during the reverse reaction with the reduction in martensite volume fraction [45]. The changes in the elastic strains are due to the lattice distortion of the martensite and strains involved during the formation of twinned and detwinned martensite. The irreversible energies are due to internal resistance to phase boundary movement caused by the formation of structural defects, which could result in thermal hysteresis losses reduction [43].

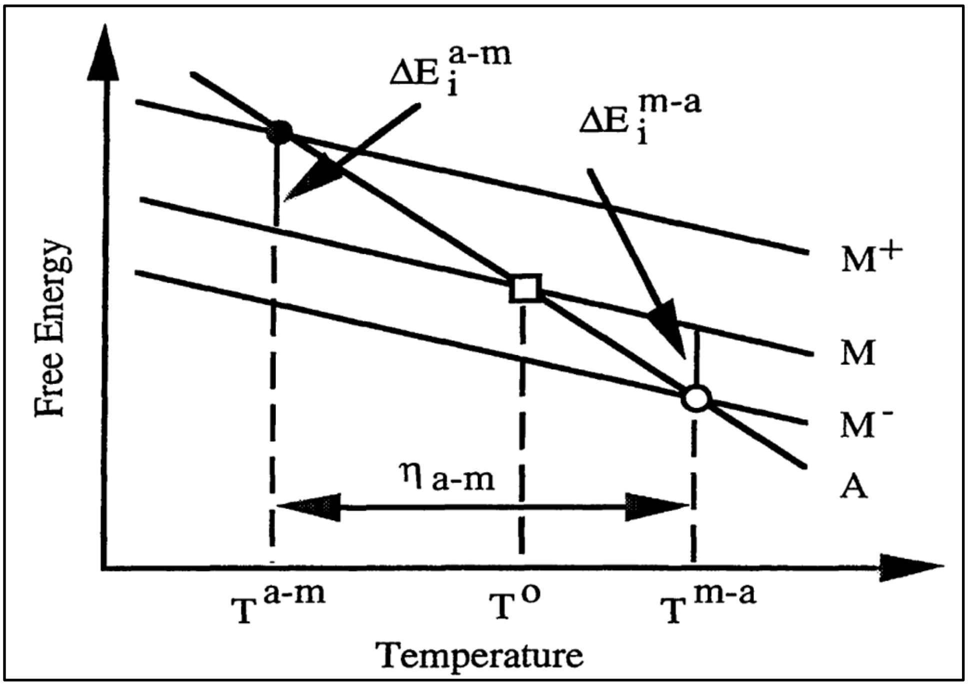

Figure 2.2.2: Schematic diagram showing the thermodynamics of the transformation in shape memory alloys [43]. The lines A and M represent free energies of the austenite and martensite transforming phases as a function of temperature, T_o is the equilibrium temperature of the transformation, while ΔE_i^{a-m} is associated with the undercooling required for the martensite transformation to proceed and ΔE_i^{m-a} is associated with the superheating required for the austenite transformation to proceed. M^+ and M^- is the martensite's free energy level lines for the forward and reverse transformation.

2.2.2. Transformation temperatures

The four characteristic temperatures associated with the phase transformation should be determined before designing and optimising the system in order to have an idea of possible operating temperatures for applications of the shape memory alloys [27,31,42], Figure 2.2.3. These phase transformation temperatures are austenite start (A_s), austenite finish (A_f), martensite start (M_s) and martensite finish (M_f) [25,31,46]. A_s is the temperature, at which the martensite to austenite transformation begins and A_f is the temperature at which the martensite to austenite transformation is completed when heating the shape memory alloy. M_s is the temperature at which the transformation from austenite to martensite begins and M_f is the temperature at which the transformation of martensite from austenite phase is completed on cooling of the shape memory alloy. The M_s temperature is used to determine the application/ operating temperature of the alloy because that is where the phase transition to martensite begins.

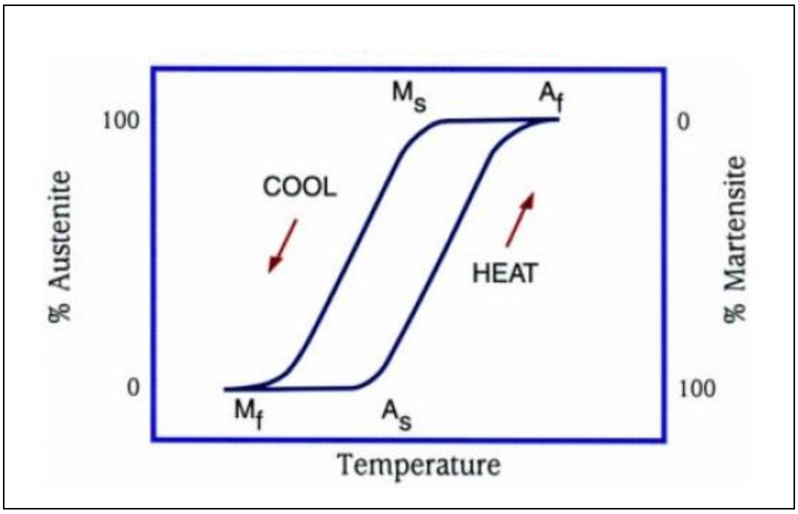

Figure 2.2.3: Characteristic temperatures involved during the martensitic transformation in shape memory alloys [31].

The thermal hysteresis is a major characteristic of martensitic transformations in shape memory alloys during thermal cycles. Liu *et al.* [43] did an in-depth study of the thermodynamics involved on the hysteretic behaviour of transformations shown in Figure 2.2.2. The forward reaction can only take place when an energy barrier ΔE_i^{a-m} is overcome by undercooling. For the reverse transformation to proceed on heating, a superheating is required to account for the energy barrier ΔE_i^{m-a}. These irreversible energy barriers shift the transformation temperatures to either side of equilibrium, leaving a temperature difference between the forward and reverse transformations, resulting in the formation of a thermal hysteresis. Thermal hysteresis in shape memory alloys is the difference in temperatures between the forward transformation (A→M) and reverse transformation (M→A) [47]. The thermal hysteresis can be calculated using the equation [47]:

$$\Delta T = A_f - M_s \qquad (2.2.1)$$

The thermal hysteresis is due to the reverse transformation taking place at higher temperatures than during the forward transformation under no application of load or stress. This is caused by frictional losses including lattice friction and the generation of defects during phase transformation to accommodate transformation shear and volume change. Upon application of a load / stress, the thermal hysteresis is due to the relaxation of elastic stored energy due to the dislocation generation such as detwinning of the martensite [47]. This transformation hysteresis is influenced by the composition of the material, amount of prior cold work, heat treatment and the texture of the material [43,47]. Reversible martensitic transformation in shape memory alloys should be exhibited by a narrow hysteresis compared to non-reversible martensitic transformation which could offer a possibility for actuation for the matching transformation application [25]. The temperature difference (thermal hysteresis) is indicative of the driving force needed to nucleate the transformation i.e. a narrow hysteresis requires a smaller driving force for the martensitic transformation than a wider hysteresis.

2.3. Functional properties

Shape memory alloys should exhibit four functional properties, namely, shape memory effect, pseudoelasticity, superelasticity and work output. The details of these properties are discussed in the next section.

2.3.1. Shape memory effect

Shape memory effect (SME) is the ability of the material to recover its original shape upon heating after plastic deformation at lower temperatures [9]. During the forward transformation under no applied load, the austenite phase transforms to martensite phase at the M_s temperature and completes the martensitic transformation at the M_f temperature. When the martensite structure is heated at the A_s temperature while following the reverse transformation path, it reverts to the austenite phase and this austenite phase transformation completes at A_f. The associated martensite variant below M_f is twinned martensite because of the very small macroscopic change in shape, Figure 2.3.1(a).

If a mechanical load higher than the detwinned start stress (σ_s) is applied to the low temperature twinned martensite structure below M_f, several martensite variants get reoriented because of the deformation. This results in a detwinned martensite structure with changes in the macroscopic shape, which cannot be retained after unloading. When the detwinned martensite structure is heated to a temperature above A_f, the structure reverts to the austenite phase while going back to its initial shape, Figure 2.3.1(b). The repetition of this transformation behaviour while regaining the original shape is known as the SME (also known as one-way SME).

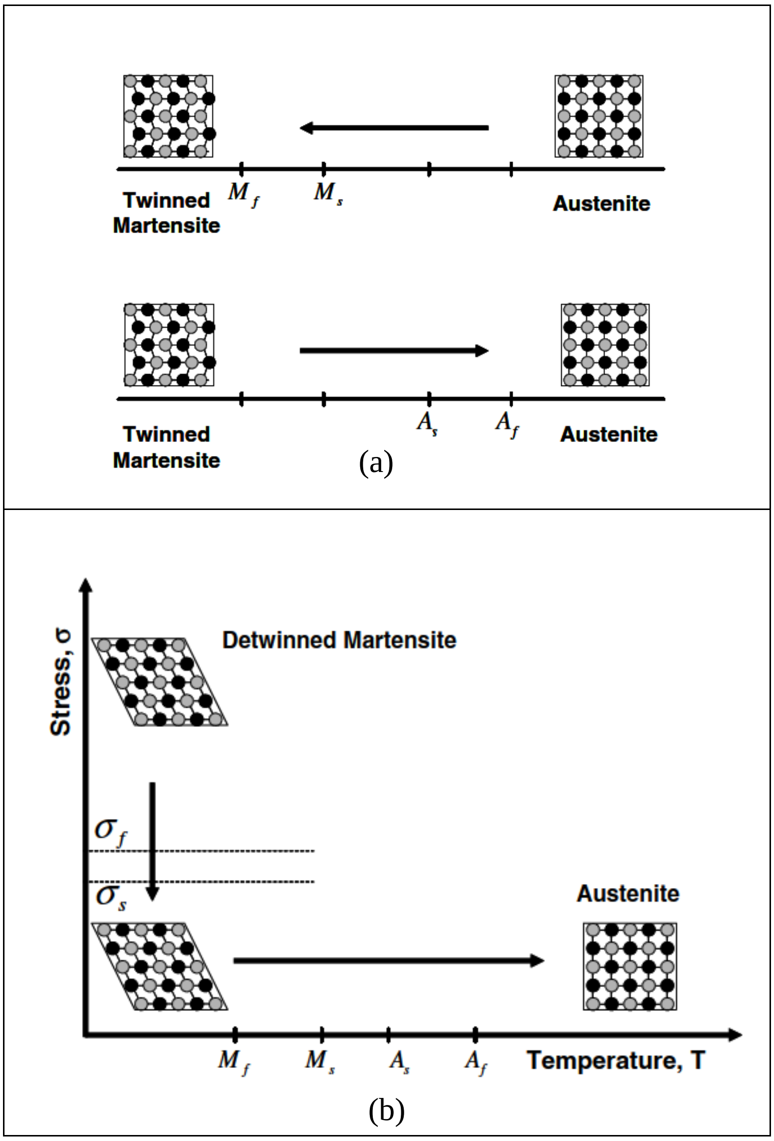

Figure 2.3.1 : Schematic presentation of the shape memory effect (SME) with (a) showing a formation of the low temperature twinned martensite upon cooling without the application of any load and (b) showing the formation of low temperature detwinned martensite upon cooling after the application of a mechanical load [25,31].

The one-way SME behaviour can be described using an experimental loading path for a Ni-Ti wire actuator shown in Figure 2.3.2 as an example. Prior to a loading / application of stress (A), the shape memory alloy in its austenite phase will transform to a twinned martensite phase upon cooling (B). Upon loading / application of stress, the twinned martensite phase gets reoriented into a detwinned martensite where deformation occurs and large macroscopic strains are observed (C, strains of 8% in Figure 2.3.2). The elastic portion of the total strain is recovered and the inelastic strain from detwinned martensite remains (stability of detwinned martensite) during unloading (D). When the same material is heated under no stress, the reverse transformation to the austenite phase begins at the A_s temperature (labelled E) and is completed at the A_f temperature. During this stage, the inelastic strain due to detwinned martensite is recovered and the material goes back to its original shape before any prior deformation (B-C).

During the transformation cycles in shape memory alloys, plastic strains that are irrecoverable could be generated and this phenomenon is known as transformation-induced plasticity (TRIP) [9]. These irrecoverable strains are usually generated quickly during the material's initial cycles and will then stabilize as the number of applied cycles increase. The repetition of applied cycles and stabilization of material's response whereby the shape memory alloy (SMA) stops generating plastic strains after sufficient cycling, is referred to as training. SMAs that exhibit the shape memory effect are used for actuation applications. Training often occurs by applying constant stress to the component and then cycling the temperature until the response has stabilized [9]. The repetition of thermal cycles for several number of times (training) lead to the formation of large strains without any external applied stress, and this behaviour is known as a two-way shape memory effect (TWSME). The TWSME involves the memorization of two shapes with any applied forces. The difference between a one way and two way SME is that no external forces are required to obtain the memorized cold shape in two-way shape memory effect and during subsequent heating, the original hot shape is restored. However, in one-way shape memory effect, an external load is applied to memorize the cold shape.

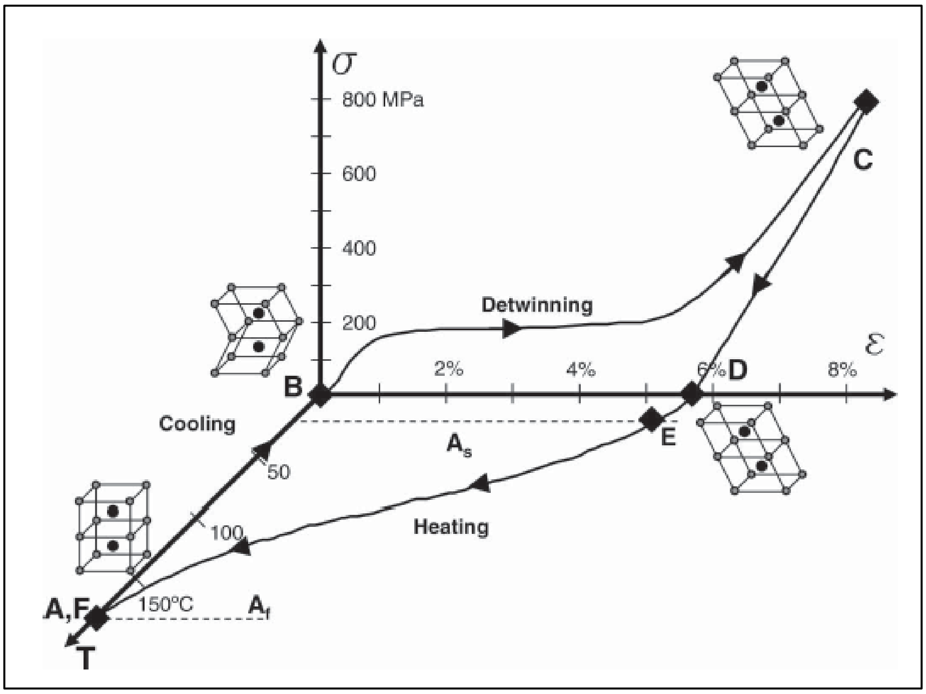

Figure 2.3.2 : Experimental loading path for the shape memory effect of Ni-Ti shape memory alloy using the stress-strain-temperature curve [9].

Figure 2.3.3 shows a schematic diagram of a stress-strain curve used to study the shape memory behaviour of shape memory alloys. The ε_a, ε_{el}, ε_{sme} and ε_{irr} are applied strain, elastic strain, shape memory strain and irrecoverable strain, respectively.

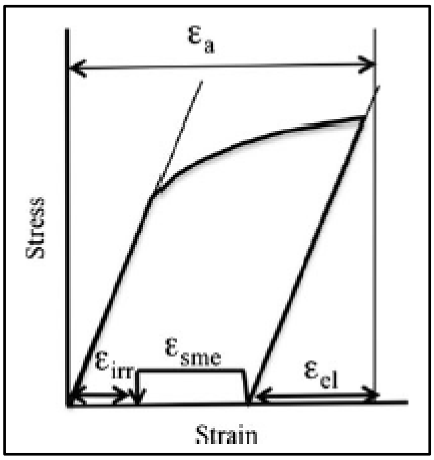

Figure 2.3.3: Schematic stress-strain curves of shape memory alloys [22].

The residual strain ε_r after unloading can be measured by comparison of the initial sample length L_0 and the sample length L' measured after the compression test at the test temperature, using the equation [22]:

$$\varepsilon_r = \frac{L_0 - L'}{L_0} \qquad (2.3.1)$$

The structure obtained during deformation at the test temperature gets heated in a heat treatment at high temperatures above the A_{f+50} temperature for a short period of time to recover the retained strain. Shape recovery occurs by reverse transformation when the alloy sample's temperature reaches the austenitic transformation temperature. The recovered sample length L" is measured at room temperature by quenching after heating the samples in the austenitic region. Then, the irreversible strain is measured by comparing the recovered sample length L" and the initial sample length, L_0 using the equation [22]:

$$\varepsilon_{irr} = \frac{L_0 - L''}{L_0} \qquad (2.3.2)$$

The shape memory / recovery strain ε_{sme} is measured by the difference between the residual strain ε_r after unloading and the irrecoverable strain using the equation [22]:

$$\varepsilon_{sme} = \varepsilon_r - \varepsilon_{irr} \qquad (2.3.3)$$

Therefore, the strain recovery ratio (SRR) (also known as shape recovery ratio) was defined by [22]:

$$\frac{\varepsilon_{sme}}{(\varepsilon_{sme} + \varepsilon_{irr})} \times 100 \qquad (2.3.4)$$

2.3.2. The Pseudoelastic effect

Pseudoelasticity is the ability of the material to recover high applied strains upon unloading of the material above the austenite temperatures [9]. This behavior involves the formation of stress-induced detwinned martensite (SIM) and the subsequent reversal to austenite upon unloading. The formation of SIM also creates inelastic strains similar to reorientation of twinned martensite. However, in pseudoelasticity, the starting phase is austenite and the actual phase transformation to martensite takes place under the influence of stress. The SIM transformation begins and ends in the austenitic region at a constant selected temperature.

Figure 2.3.4 is a schematic diagram showing the loading path used to describe the pseudoelasticity behavior in shape memory alloys. When a material is heated above the A_f temperature, the martensite fully transforms into a stable austenite phase [25, 31]. If a mechanical load above the detwinning finish stress σ_f is applied to this austenite phase above the A_f temperature, the load will result in a fully detwinned martensite structure created from the austenite phase. If the temperature of the material is above A_f, a complete shape recovery of the austenite phase is observed upon unloading, thus the material behavior resembles elasticity.

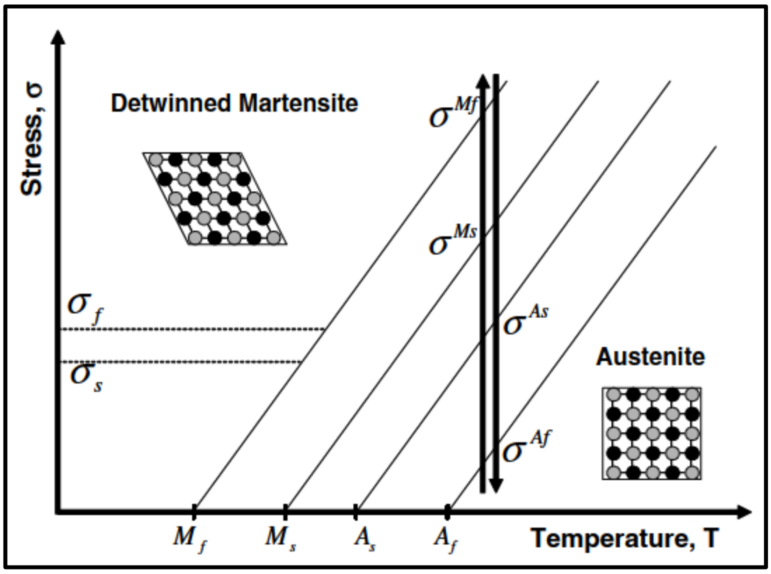

Figure 2.3.4 : Schematic diagram of the pseudoelasticity /superelasticity behavior in shape memory alloys [25,31].

The pseudoelasticity loading path behavior may be described using an experimental stress-strain curve of Ni-Ti alloy where the temperature was maintained at a constant temperature of 80 °C, Figure 2.3.5 [9]. Prior to loading / application of stress, the material is in the austenite phase (above A_f) at point 1. Upon loading or application of stress, at stresses below σ^{Ms}, the material deforms elastically (between point 1 and 2) and when the material's critical stress σ^{Ms} is reached, the transformation and detwinning of the martensite begins at point 2 and the transformation completes when the applied critical stress reaches σ^{Mf}, resulting in a fully detwinned martensite phase at point 3. Large inelastic strains are generated during the transformation to SIM. Further loading will lead to elastic deformation of the detwinned martensite and upon unloading, the reverse transformation starts at a critical stress σ^{As} at point 4 and completes at a stress of σ^{Af} (point 5). By the end of unloading at point 5, the material reverts to the austenite phase and both transformation strain (ε^{t}) and elastic strain (ε^{el}) are recovered. However, the plastic strain (ε^{pl}) generated does not recover.

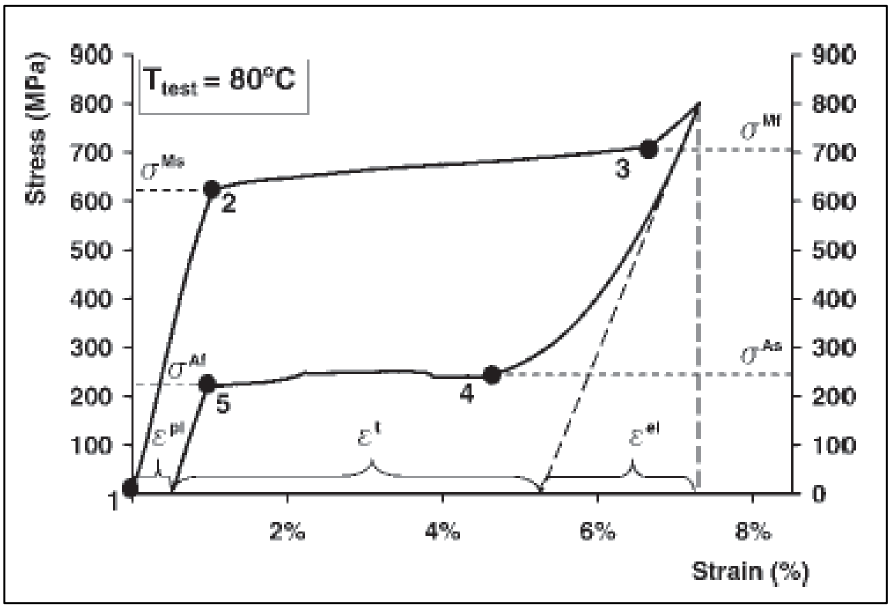

Figure 2.3.5: Experimental results showing the pseudoelastic effect of a Ni-Ti SMA [9].

The SMAs that exhibit pseudoelasticity are used for applications such as vibration isolators and dampers. The stability of the material's response to training is carried out by applying many stress cycles while maintaining a constant temperature [9]. Pseudoelasticity is associated with large recoverable deformations with large hysteresis loops depending on the level of the stress applied [9,48]. The large hysteresis is indicative of some amount of mechanical energy dissipated as thermal energy for every loading cycle.

2.3.3. The superelastic effect

The difference between pseudoelasticity and superelasticity is that pseudoelasticity occurs at high temperatures while superelasticity takes place at low temperatures. Superelasticity is the ability of a material to recover high-applied strains upon unloading of the material at low temperatures [49]. Prior to loading or application of stress, the material is in the twinned martensitic phase. Upon loading or application of stress, the material deforms elastically, resulting in significant deformation strains and macroscopic changes associated with the transformation and detwinning of the martensite, Figure 2.3.6. The transformation completes when the structure is a fully detwinned martensite phase. Further loading will lead to elastic deformation of the detwinned martensite and upon unloading, the material reverts back to its original shape at low temperatures whereby the transformation strain (ε^t) and elastic strain (ε^{el}) is also recovered.

The superelasticity effect has been widely used for medical application as stents and eye glasses where they can be bent and twisted, yet, revert back to their original shape after unloading [42,49].

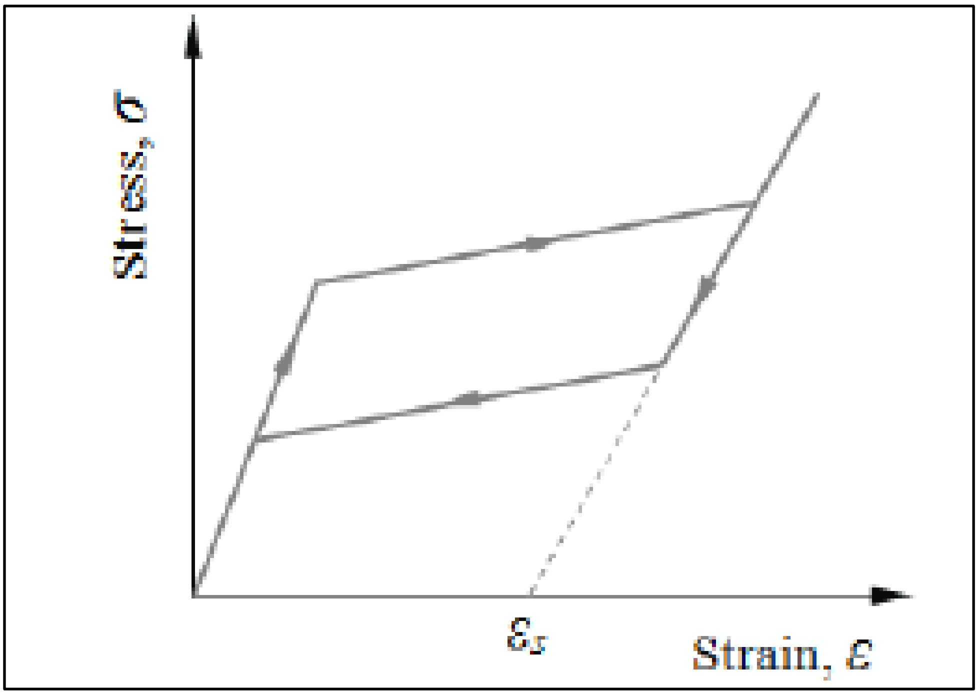

Figure 2.3.6: Stress-strain curve for a shape memory alloy that exhibits the superelastic effect [49].

2.3.4. Work output

Work output is the ability of the material to perform work against an external applied load [16]. If the SMA shows work output capabilities, it can be used as an actuator for temperature applications that match its transformation temperature. Work output characteristics of the SMA can be determined using a constant load strain recovery test (load bias test). Figure 2.3.7 is a schematic diagram of an estimate of work output during one thermal cycling of a shape memory alloy. Initially, the alloy is strained at room temperature until it attains the desired stress. Once the desired load is reached, the stress is kept constant while the specimen is cycled from room temperature to temperatures above the A_f. During the thermal cycle, the strain recovery is recorded continuously and once the cycles are complete, the specimen is unloaded at room temperature. The loading, thermal cycling and unloading behavior is repeated several times in order to study the work output of the material under different applied constant stresses until the sample fails. Padulla ll *et al.* [16] determined the work output characteristics for the Ni-Ti-Pt and Ni-Ti-Pd SMAs by taking the product of the applied bias stress and the strain recovered during the martensite to austenite transformation from the second thermal cycling imposed at each load level, Table 2-1. They found that a maximum output of 10.47 J/cm^3 was achieved by Ni_{30}-Ti_{50}-Pt_{20} with an applied stress level between 350 and 450 MPa, Table 2-1.

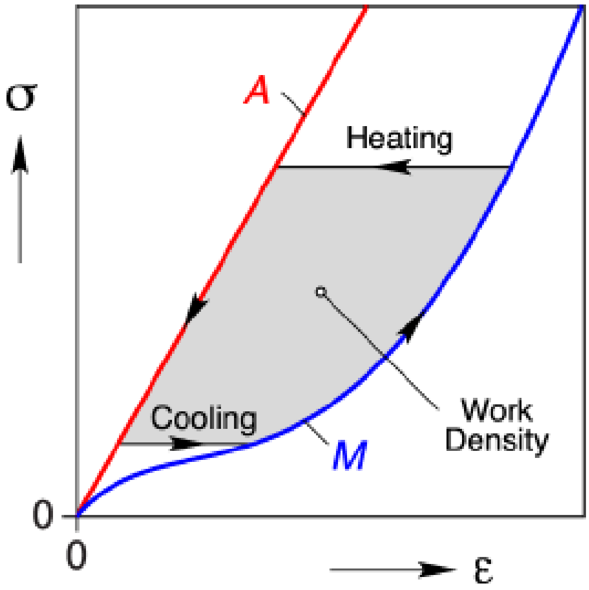

Figure 2.3.7: The estimation of the work output of shape memory alloys during thermal cycling [50].

Table 2-1: Work outputs and transformation temperatures with different alloying compositions in Ni-Ti-Pt and Ni-Ti-Pd alloys [16].

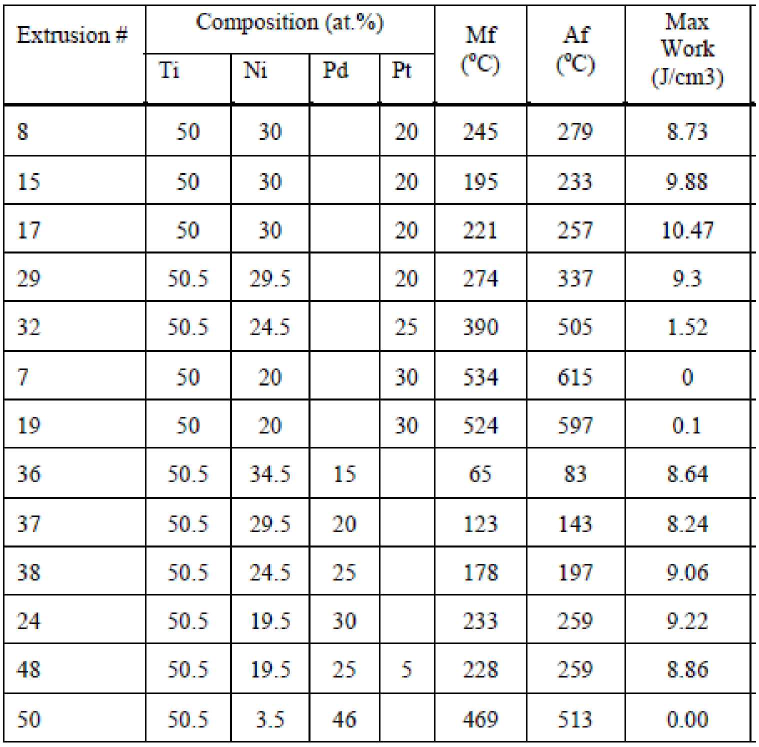

Extrusion #	Composition (at.%)				Mf (°C)	Af (°C)	Max Work (J/cm3)
	Ti	Ni	Pd	Pt			
8	50	30		20	245	279	8.73
15	50	30		20	195	233	9.88
17	50	30		20	221	257	10.47
29	50.5	29.5		20	274	337	9.3
32	50.5	24.5		25	390	505	1.52
7	50	20		30	534	615	0
19	50	20		30	524	597	0.1
36	50.5	34.5	15		65	83	8.64
37	50.5	29.5	20		123	143	8.24
38	50.5	24.5	25		178	197	9.06
24	50.5	19.5	30		233	259	9.22
48	50.5	19.5	25	5	228	259	8.86
50	50.5	3.5	46		469	513	0.00

2.4. Mechanical properties of shape memory alloys

Compression tests, tensile tests and hardness tests can be used to determine the mechanical properties of the SMAs. When a load or stress is applied to a SMA, the alloy undergoes several stages of deformation. Figure 2.4.1 depicts several stages of deformation that Ni-Ti SMAs undergo during compression or tensile testing using a stress-strain curve [20]. During the first stage of deformation, the alloy deforms elastically until point A, such that, it will recover its original shape/dimensions when the load or stress is removed. The associated deformation is due to the elastic accommodation of twin bands. At point A, the first yielding point occurs by the reorientation of martensite twin variants, known as detwinning stress or reorientation stress of martensite variants until the martensite is fully detwinned at point B. After the martensite is fully detwinned, the alloy displays secondary elastic deformation where the detwinned martensite deforms elastically at this stage. At point C, the second yielding point occurs where slip begins (plastic deformation), which indicates the critical stress for slip. During this stage, the deformation is no longer completely reversible upon unloading or when heated above the A_f temperature. If the critical stress for slip is lower than the detwinning stress, there will be no double yielding behaviour of the martensite phase and this will result in a reduction of the shape memory effect. The reorientation of martensite variants can occur under a small stress when the detwinning stress is small, while plastic deformation becomes harder when the yield stress is high [20].

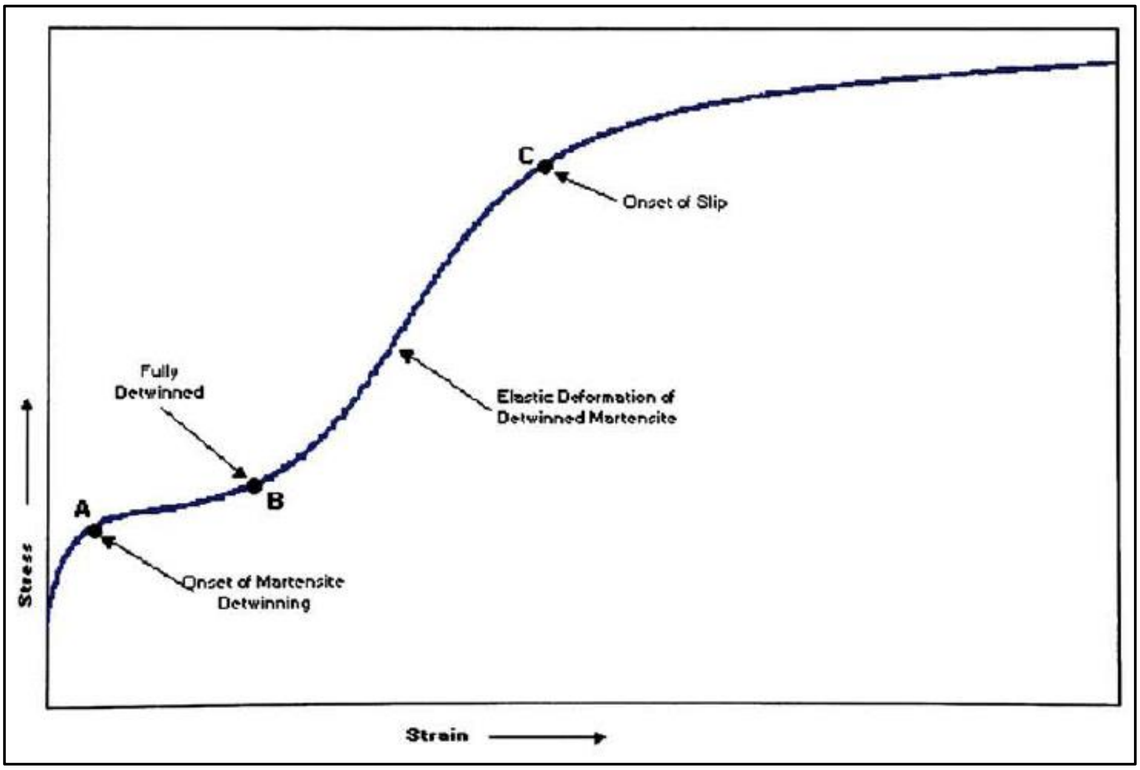

Figure 2.4.1: Schematic diagram of stress-strain curve of Ni-Ti alloys [51].

Biggs *et al*. [37] examined the mechanical properties of solution treated binary Ti-Pt using a Vickers hardness tester with a load of 10 kg. They reported that the lowest hardness was found in the TiPt martensite with around 50 at.%, Figure 2.4.2. However, the hardness increased rapidly as the stoichiometry deviated on either side of the 50 at.%. This indicated that 50 at.% TiPt martensite shows the lowest strength compared to the non-stoichiometric TiPt phase. They reported that the increase in hardness within the single phase region was attributed to the variation of point defects such as vacancies and antisites across the range of stoichiometry [37]. In addition, the increase in hardness when outside of the single-phase region could be due to the presence of other phases in the alloy.

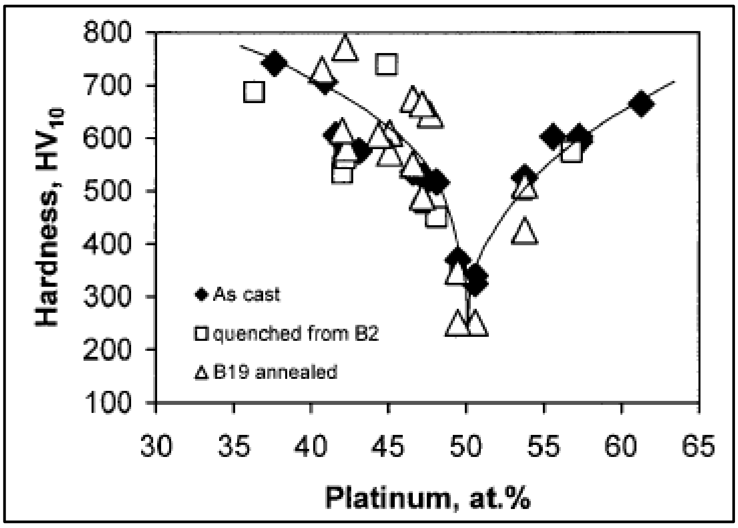

Figure 2.4.2: The variation in hardness of the Ti-Pt system between 36 and 60 at.% Pt [37].

2.5. Phase diagrams of Ti-Pt

The first comprehensive study on Ti-Pt alloys was done by Nishimura and Hiramitsu [52] in 1957 using metallographic examination, X-ray analysis, differential thermal analysis (DTA) and melting point measurements. This study led to the construction of the first equilibrium phase diagram of Ti-Pt, Figure 2.5.1. The authors reported three intermetallic phases: Ti_3Pt, TiPt and $TiPt_3$, which melt congruently at their respective temperatures of 1370, 1830 and 1950 °C. They also reported three eutectic reactions, one eutectoid reaction and one peritectoid reaction taking place, which are summarized as follows:

Eutectic reaction: (1) At 1310 °C: L → β + Ti_3Pt having approximately 15 at.% Pt.
(2) At 1320 °C: L → Ti_3Pt + TiPt having approximately 34 at.% Pt.
(3) At 1780 °C: L→ TiPt + $TiPt_3$ having approximately 58 at.% Pt.

Eutectoid reaction: At 840 °C: β-Ti → α-Ti + Ti_3Pt having approximately 3 at.% Pt.

Peritectic reaction: At 1800 °C: L + $TiPt_3$ → γ-Pt having approximately 81 at.% Pt.

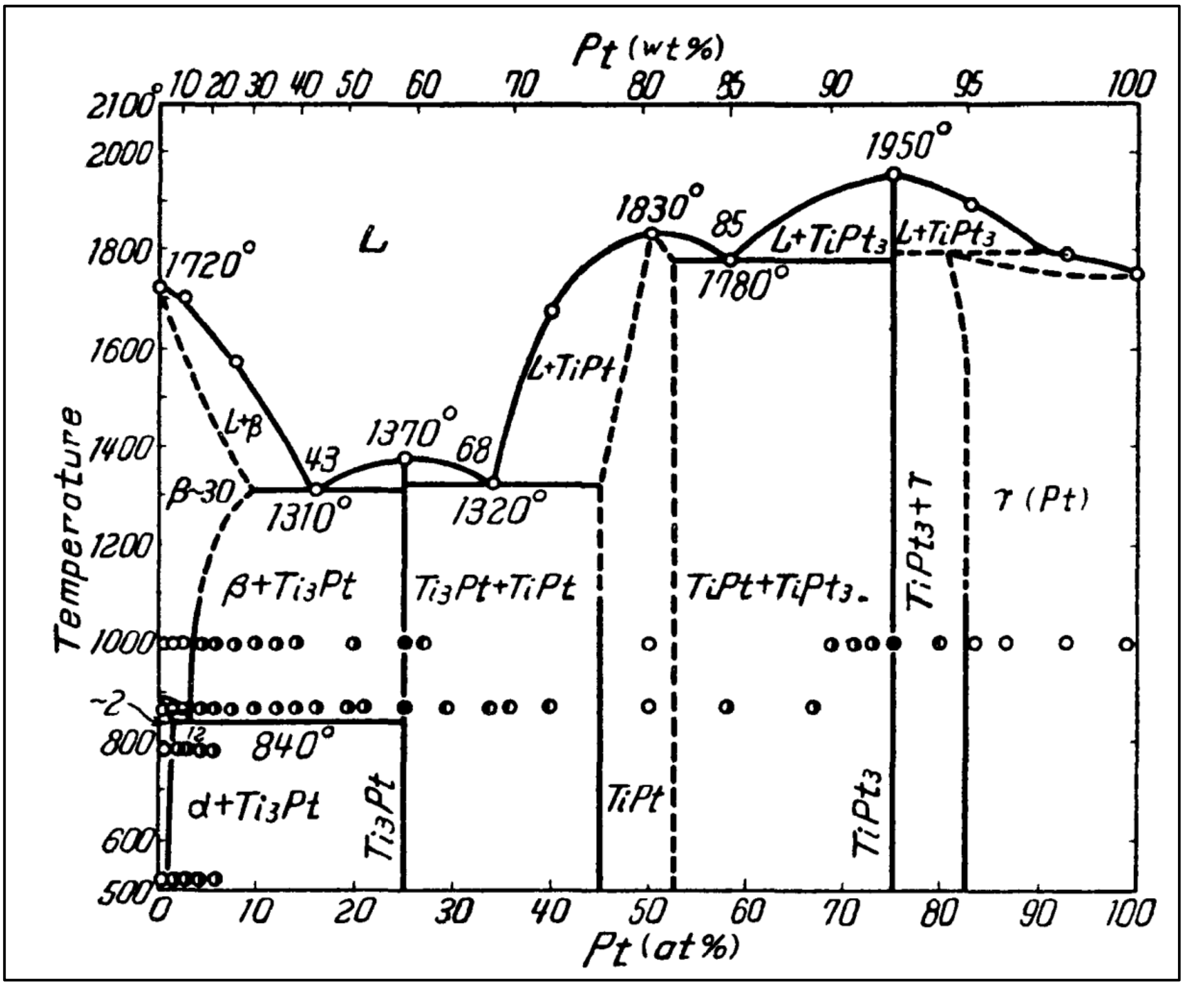

Figure 2.5.1: Ti-Pt equilibrium phase diagram proposed by Nishimura and Hiramitsu in 1957 [52].

Pietrowsky [53] discovered the $TiPt_8$ phase on the Pt-rich end of the phase diagram in 1965 by using XRD patterns. In 1976, Junod *et al.* [54] found that the Ti_3Pt phase was not stoichiometric as suggested by Nishimura and Hiramitsu [52]. They found that it had a composition range between 22 and 29 at.% Pt. Donkersloot and Van Vucht in 1970 [55] investigated the crystal structure of the TiPt phase reported by Nishimura and Hiramitsu [52]. They found that the TiPt phase existed in two crystal structures viz. a high temperature β-TiPt phase and a low temperature α-TiPt phase [55,56]. The α-TiPt phase is a stable phase at room temperature up to 1070 °C and β-TiPt is stable from 1070 °C up to the melting point of 1830 °C. These phases gave B2→B19 martensitic transformations based on the DTA results. This reversible transformation exhibits the SME.

Murray [57] later on in 1982 published a modified phase diagram using thermodynamic calculations, Figure 2.5.2. The phase diagram included the composition range of the Ti_3Pt phase and the Pt-rich $TiPt_8$ phase identified by Pietrowsky [53]. This phase diagram included the two crystal structures of the TiPt phase found by Donkersloot and Van Vucht [55].

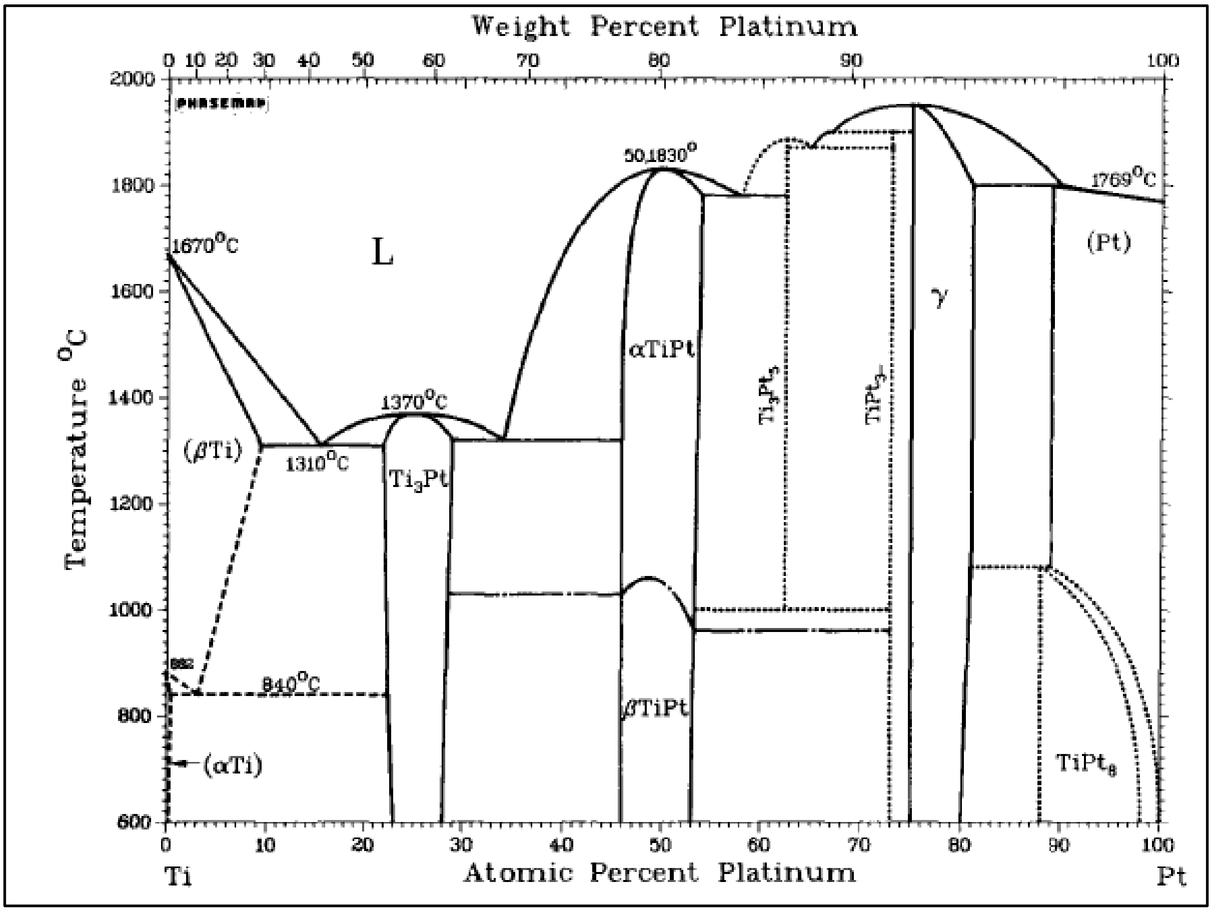

Figure 2.5.2: Ti-Pt equilibrium phase diagram found by Murray in 1982 [57].

In 2004, Biggs *et al.* [46] studied the Ti-Pt phase diagram at composition ranges between 30 and 60 at.% Pt using an optical microscopy (OM), scanning electron microscopy (SEM), X-ray diffraction (XRD) and a differential thermal analysis (DTA). They found that there was a new stable phase, Ti_4Pt_3 with compositions in the range of 41.7 and 43.4 at.% Pt existing between the Ti_3Pt and TiPt phases. They reported that the new phase was formed by a peritectoid reaction between β-TiPt and Ti_3Pt phase at approximately 1205 °C based on the DTA results, Figure 2.5.3.

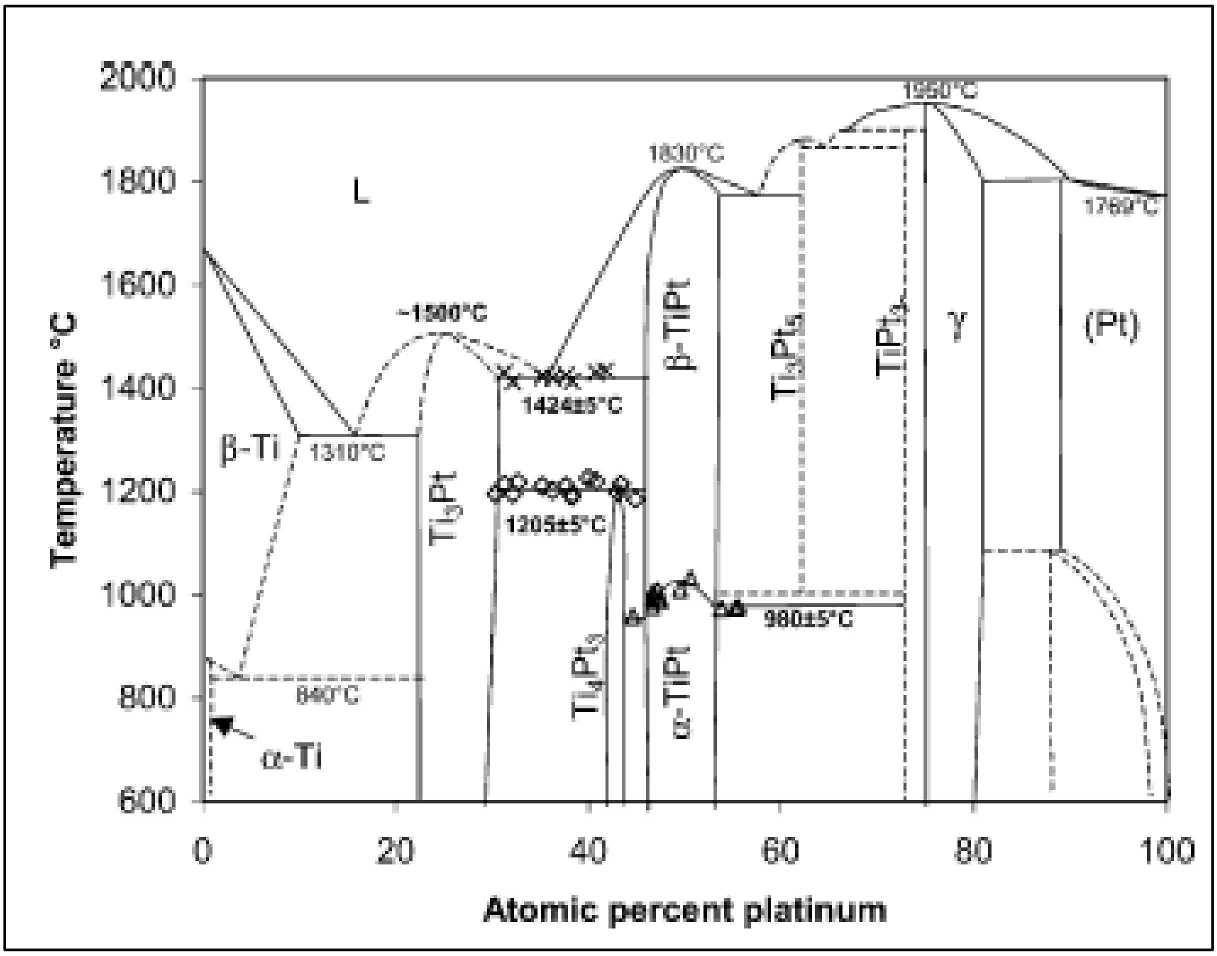

Figure 2.5.3: Ti-Pt equilibrium phase diagram modified by Biggs *et al.* in 2004 [46].

Li *et al.* [58] used the thermodynamic optimization to derive the phase diagram of Ti-Pt system using computational modelling by using a computer technique called CALPHAD. The thermodynamic optimization process was carried out by using the experimental data and thermodynamic data from Nishimura *et al.* [52] and Biggs *et al.* [46]. The compilation resulted in the construction of the phase diagram in Figure 2.5.4.

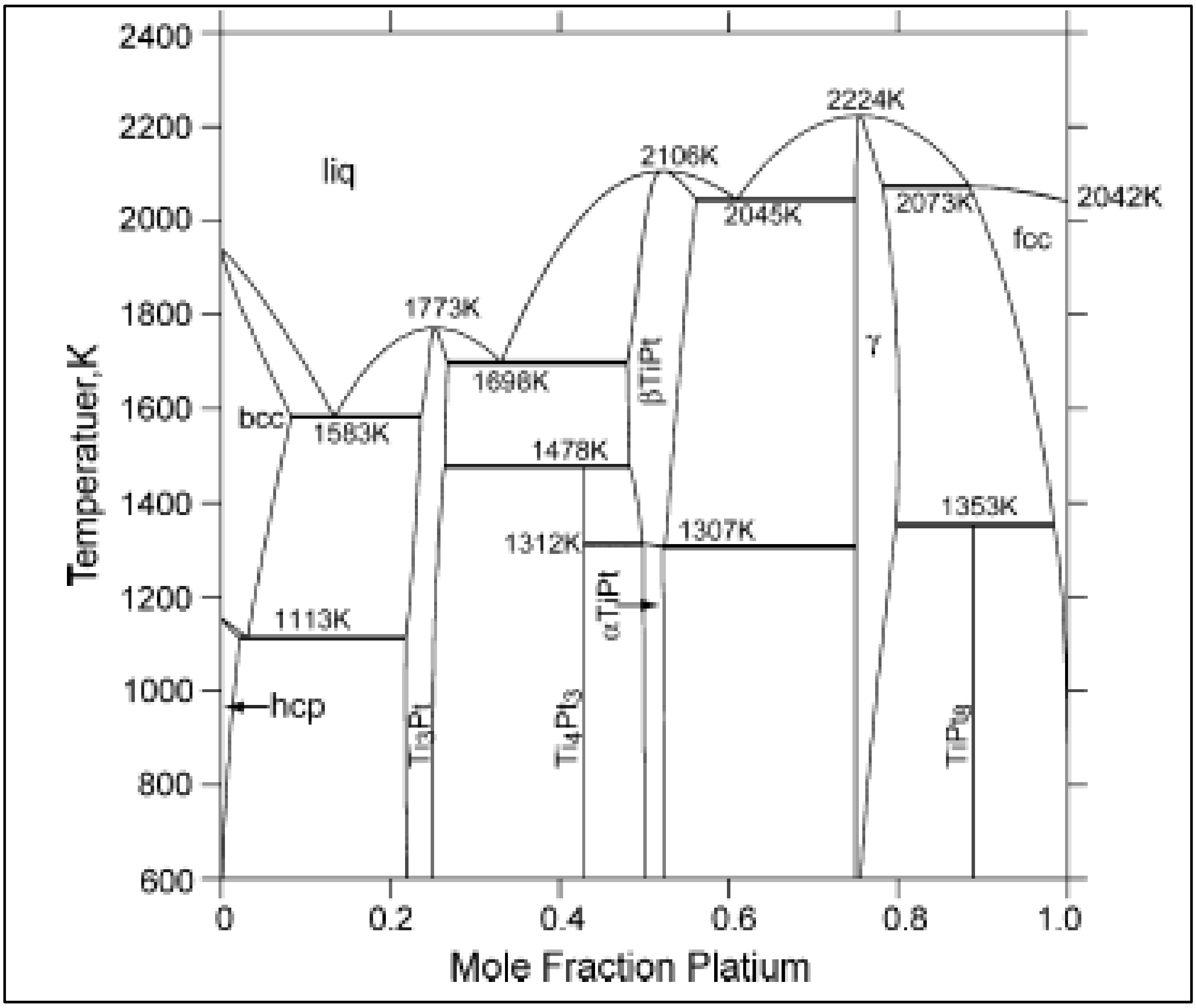

Figure 2.5.4: Ti-Pt equilibrium phase diagram after modification by Li *et al.* in 2008 [58].

Recently, Tello [25] also did an experimental study on the phase diagram proposed by Biggs *et al.* [46] in the composition range of 30 to 50 at.% Pt using SEM, TEM and DTA techniques. Tello [25] confirmed the occurrence of the peritectoid reaction at the Ti_3Pt and β-TiPt interfaces to form Ti_4Pt_3 and also proposed a modification of the phase diagram, as shown in Figure 2.5.5. According to the modifications, the β-TiPt solidus line should be displaced to lower Pt ranges and the β-TiPt solvus line must display increasing Pt solubility until the original solvus line is reached at 1100 °C. The resultant modifications on the phase diagram were based on differences in the volume fraction of dendrites observed experimentally. The presence of Ti_5Pt_3 phase in Ti-Pt alloys which contains a slightly lower Pt content than the Ti_4Pt_3 phase was also observed. The Ti_5Pt_3 phase is an oxygen stabilised phase, where oxygen could have been picked up in the starting powders, during processing or heat treatments [25].

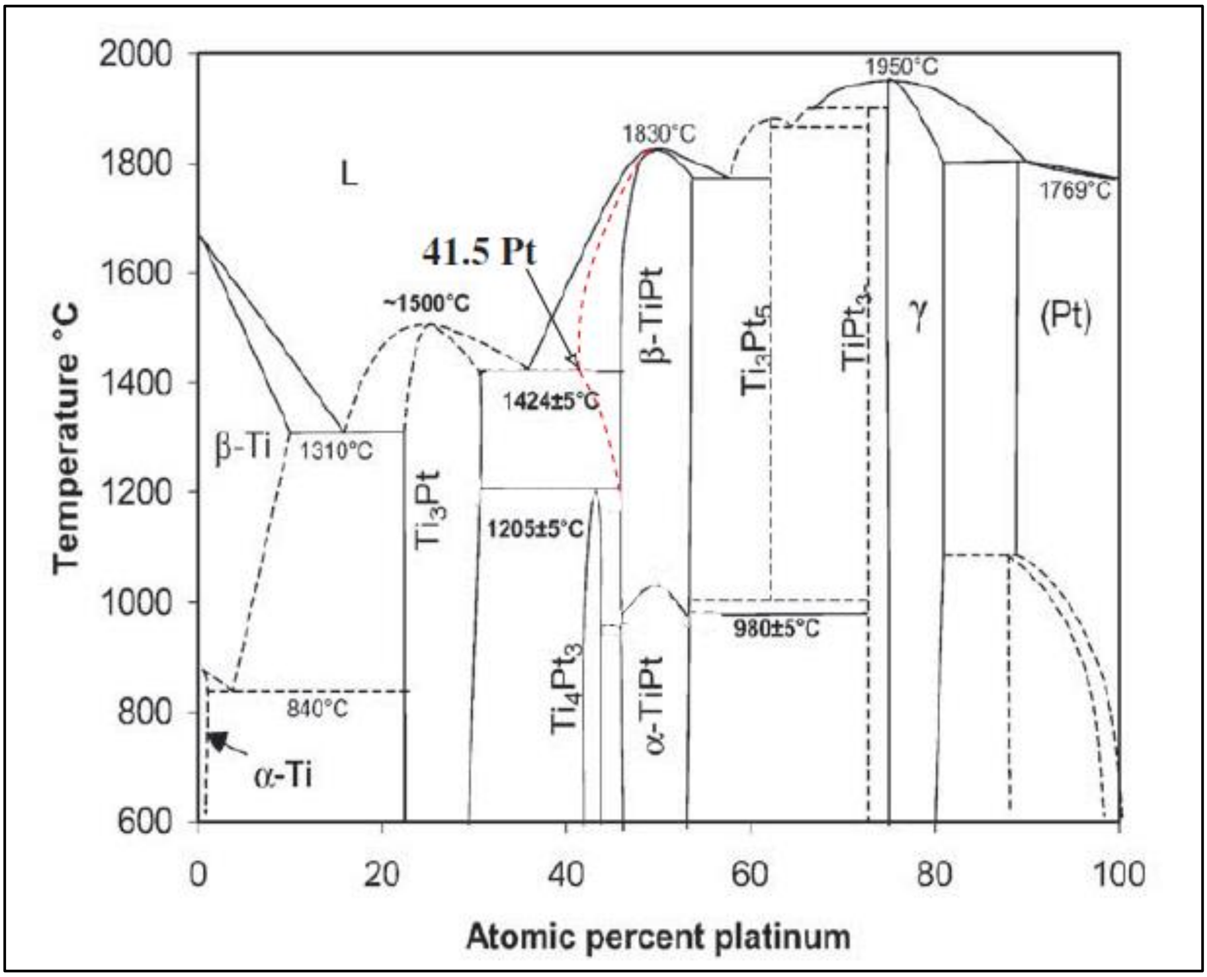

Figure 2.5.5: Modified equilibrium Ti-Pt phase diagram by Tello in 2017 [25].

In addition, Pt-V and Ti-V phase diagrams were also included in this study because the effect of ternary alloying Ti-Pt alloys was investigated using V as a ternary alloying element in the absence of an existing ternary Ti-Pt-V or Ti-V-Pt phase diagram, Figure 2.5.6. The Pt-V phase in Figure 2.5.6(a) was examined by Waterstrat [59] in 1973. The solubility of V in Pt is about 20.5 at.% V at 700 °C and it increases with increasing temperature, reaching approximately 57 at.% V at 1720 °C [60]. The solubility of Pt in V is up to 12 at.% Pt in BCC α-V at a temperature of about 1800 °C.

Figure 2.5.6(b) shows the binary Ti-V phase diagram which consists of only three phases, namely the liquid, the α and the β phases [61–63]. The solubility of V in α- and β- Ti was investigated by determining the α/α+β and β/α+β boundaries using microprobe and metallography techniques [63]. The maximum solubility of vanadium in α-Ti is approximately 3.7 at.% (0.037)V above temperatures of 773-873 K [63]. The β/α+β boundary decreases in temperature with increasing vanadium contents.

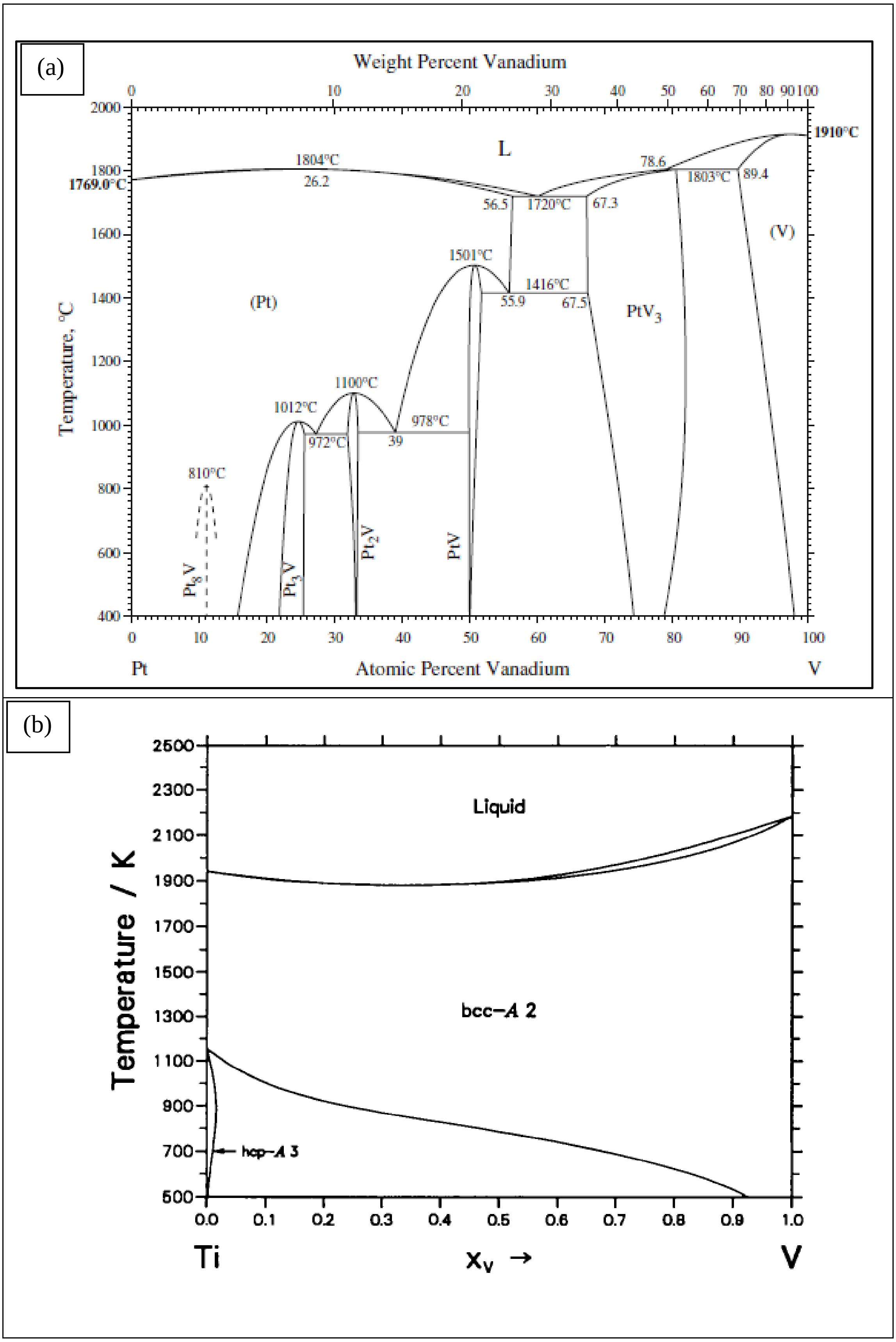

Figure 2.5.6: Phase diagrams of the Pt-V [59] and Ti-V systems [61]

2.5.1. Martensitic TiPt phase

The Ti-Pt system undergoes a martensitic transformation at composition ranges of between 46 and 54 at.% Pt which is a single TiPt phase region. Within this composition range, the alloy undergoes a displacive phase transformation from a cubic (B2) high temperature austenite phase (β-TiPt) having a BCC structure to a low temperature B19 martensitic structure, Figure 2.5.7 [41]. The Ti-Pt alloy has a martensite start temperature of just over 1000 ^{o}C in this region, [11,19-21]. The martensitic transformation takes place by shear distortion of the (110)$_{B2}$ basal plane along the [110]$_{B2}$ direction of the austenite phase which is achieved by the movement of the interface that separates the austenite phase from the martensite phase, thereby creating the B19 martensite structure [25,42].

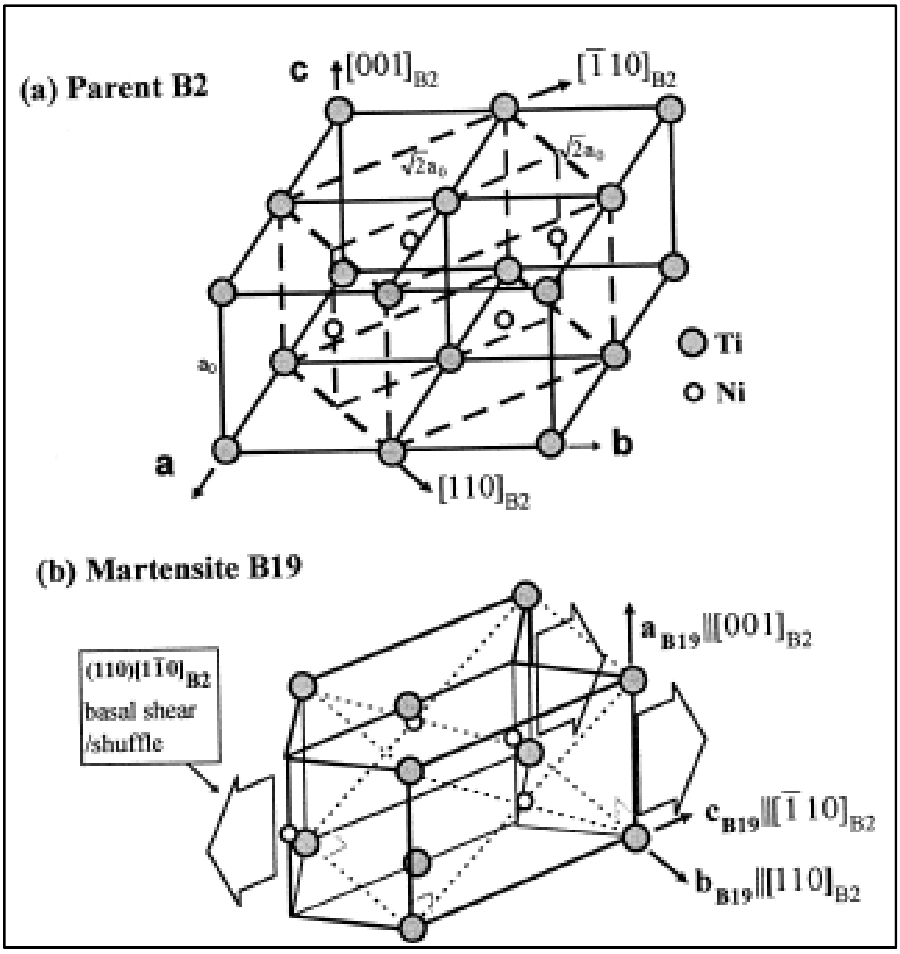

Figure 2.5.7: The crystal structures of TiPt parent austenite and martensite phase in the Ti-Pt system [25,42].

Table 2-2 shows the crystal structures known to be involved in the formation of the reversible martensitic transformations in Ti-Pt alloys. The martensitic phase has a crystal structure similar to that of gold-cadmium (AuCd) and the austenite phase to that of cesium-chloride (CsCl).

Table 2-2 : Summary of known crystal structure, space group and lattice parameters of the phases involved in the martensitic transformation [25,55,56].

Phase	Structure	Prototype	Space group	Cell parameters	
				Lattice parameter (nm)	Angle
α-TiPt	B19	AuCd	*Pmma*	a=0.455	α=90°
				b=0.273	β=90°
				c=0.479	γ=90°
β-TiPt	B2	CsCl	*Pm3m*	a=0.3192	α=90°
				b=0.3192	β=90°
				c=0.3192	γ=90°

2.5.1.1. Structural and phase identification of TiPt

Biggs *et al.* [64] did microstructural analysis of Ti-Pt with varying contents of Pt using SEM. All samples in the composition ranges of 46 to 54 at.% Pt contained laths and twins indicating that a displacive transformation took place at some higher temperatures, Figure 2.5.8. The morphology of the laths and twins was different with varying contents of Pt, where 49.5 at.% Pt had broad laths with a well-developed midrib (Figure 2.5.8(a)) and 53.8 at.% Pt had narrow laths which appeared like twins (Figure 2.5.8(b)). They also observed that materials with less than 50 at.% Pt contained grain boundary precipitates (black particles in Figure 2.5.8(c)) and these precipitates were suggested to form by internal oxidation forming a ternary $(Ti_2Pt)_xO_y$ oxide phase.

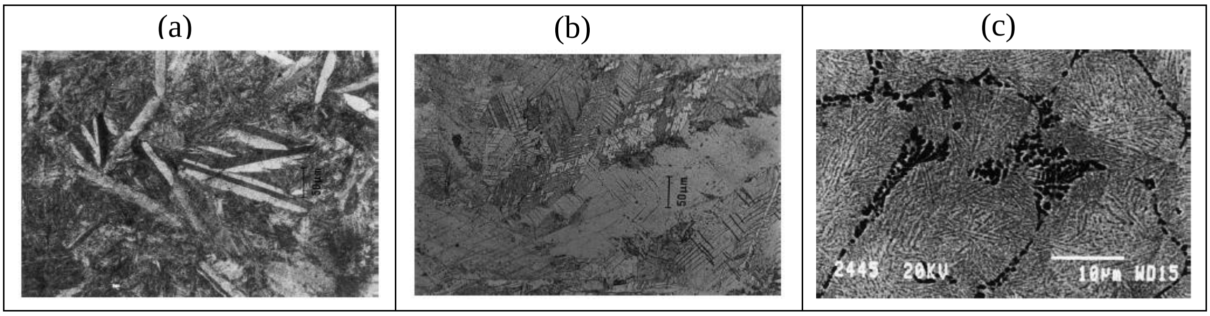
(a) (b) (c)

Figure 2.5.8: Microstructure of TiPt phase with (a) 49.5 at.% Pt, (b) 53.8 at.% Pt after annealing at 1200 °C for 72 hours and (c) backscattered electron image of a sample containing 47.7 at.% Pt after annealing at 800 °C for one hour, followed by furnace cooling [64].

Rotaru *et al.* [65] used X-ray and neutron diffraction studies to confirm the crystal structure of the as cast stoichiometric Ti-Pt alloy, Figure 2.5.9. Both results confirmed a TiPt phase with a B19 crystal structure at room temperature.

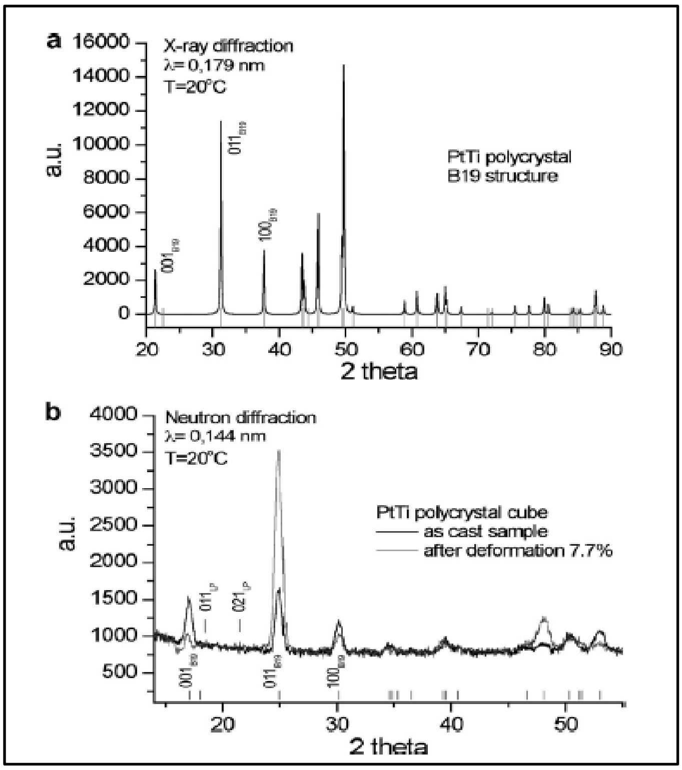

Figure 2.5.9: X-ray and neutron powder diffraction spectra of TiPt martensite taken at room temperature on the as-cast Ti-Pt alloys respectively [65].

Yamabe-Mitarai *et al.* [66] also investigated the martensitic transformation behaviour of Ti_{50}-Pt_{50} using a high temperature X-ray diffractometry. Ti_{50}-Pt_{50} was prepared by an arc-melting method and heat-treated for 3 hours at 1523 K (1250 ^{o}C) in a vacuum furnace, followed by ice water quenching. Figure 2.5.10 shows that the diffraction pattern of the B19 structure could be identified up to 1173 K and only a B2 structure at 1473 and 1573 K. They also found that the lattice parameters of the B19 phase increased with increasing test temperature, Table 2-3. The coefficient of thermal expansion was estimated from the lattice parameter change as [66]:

$$\Delta L = \propto \times L \ \times \Delta T \qquad (2.5.1)$$

where ΔL, L and ΔT are the thermal expansion, initial length and temperature difference.

The lattice parameters at each test temperature and coefficients of thermal expansions are summarized in Table 2-3. The largest coefficient of thermal expansion was in the lattice parameter b, the smallest parameter of the B19 phase. However, the smallest coefficient of thermal expansion was in the lattice parameter c, the largest parameter of the B19 phase. This showed that the lattice parameter b expanded the most with increasing test temperature. Figure 2.5.11 shows that the lattice parameter ratios a/b and c/b decrease with increasing temperature.

This indicated a reasonable change of an orthorhombic B19 structure to cubic B2 above 1273 K [66].

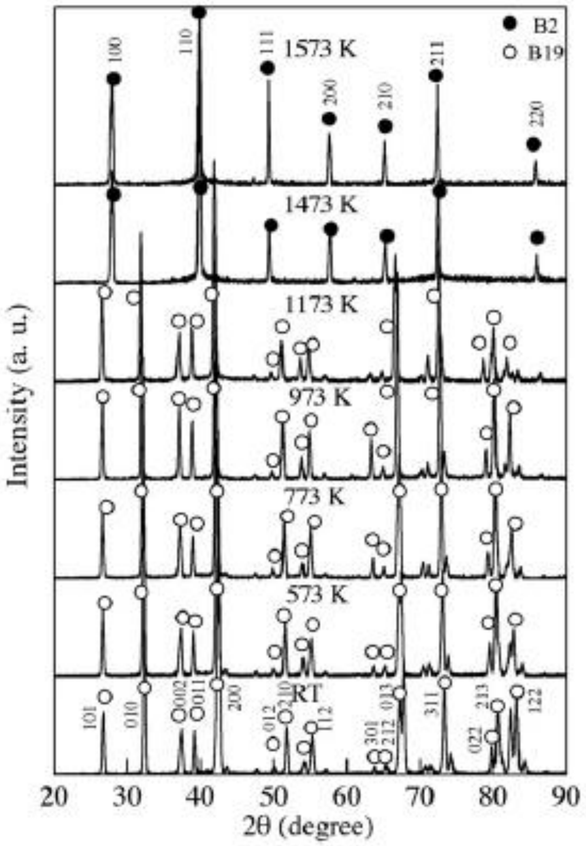

Figure 2.5.10: XRD patterns of TiPt from room temperature to 1573 K. Solid and open symbols represent peaks from the B2 and B19 structure respectively [66].

Table 2-3: Lattice parameters of the cubic B2 and orthorhombic B19 phases at different test temperatures with coefficients of thermal expansion of the B19 phase [66].

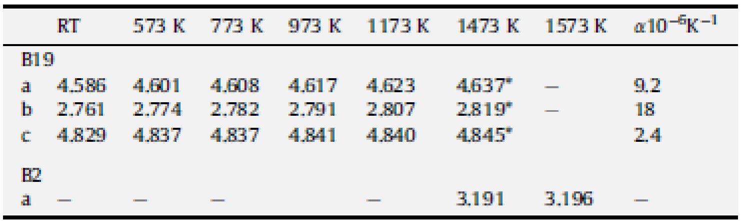

	RT	573 K	773 K	973 K	1173 K	1473 K	1573 K	$\alpha 10^{-6} K^{-1}$
B19								
a	4.586	4.601	4.608	4.617	4.623	4.637*	–	9.2
b	2.761	2.774	2.782	2.791	2.807	2.819*	–	18
c	4.829	4.837	4.837	4.841	4.840	4.845*		2.4
B2								
a	–	–	–		–	3.191	3.196	–

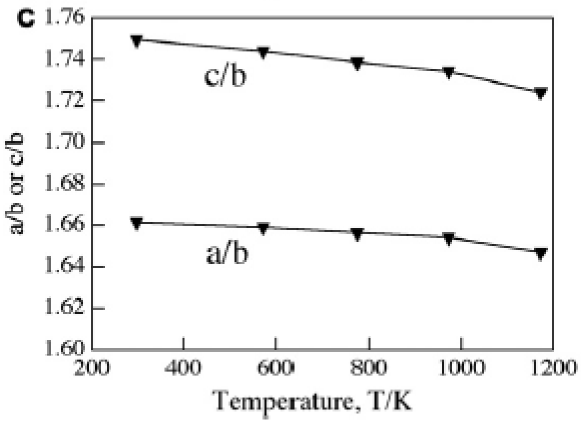

Figure 2.5.11: Change in lattice parameters *a* and *c* for lattice parameter *b* [66].

2.5.1.2. Martensite transformation behaviour of TiPt

Donkersloot and Van Vucht [55] investigated the effect of varying platinum contents on the M_s temperature of Ti-Pt alloys using DTA. They found that the M_s temperature was maximum at a composition of about 50 at.% Pt. Above 50 at.%, the transformation temperatures decreased significantly but they were still above 900 °C, Figure 2.5.12. A similar behaviour was also observed by Biggs *et al.* [37] where they confirmed that the highest transformation temperatures occur at about 50 at.% Pt. However, the A_s temperatures reported by Biggs *et al.* [37] were above the M_s temperatures and the opposite was observed by Donkersloot and Van Vucht [55]. Donkersloot and Van Vucht [55] speculated that the difference in temperatures may have been caused by the formation of intermediate phases between B2 and B19 in the phase formation.

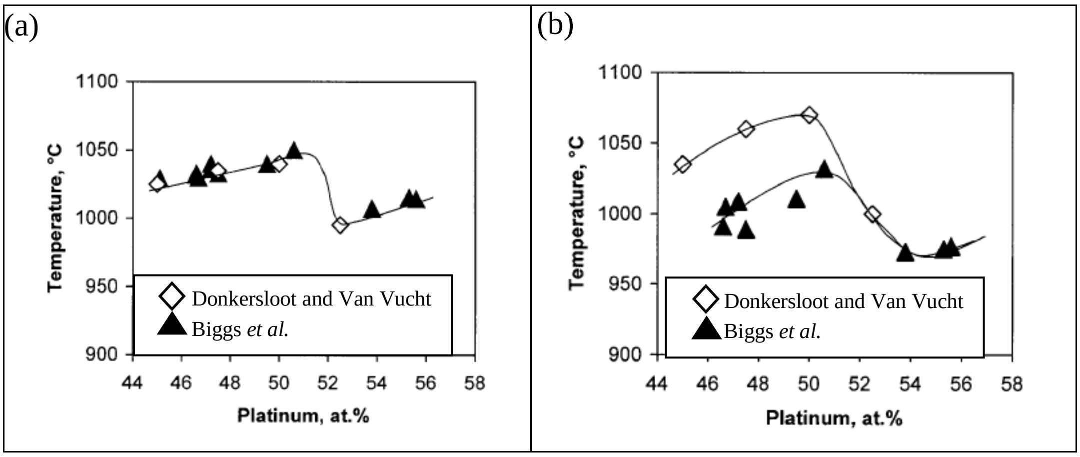

Figure 2.5.12: The effect of composition on (a) austenite start temperature, A_s, and (b) martensite start temperature, M_s of Ti-Pt alloys [37,55].

The presence of intermediate phases was further confirmed using DTA results from Biggs *et al.* [37] where they reported the presence of multiple peaks in samples with compositions between 43 and 50 at.% Pt. These samples showed two peaks during cooling and an additional small intermediate peak during heating; whereas the TiPt phase with Pt compositions greater than 50 at.% displayed only a single peak, Figure 2.5.13.

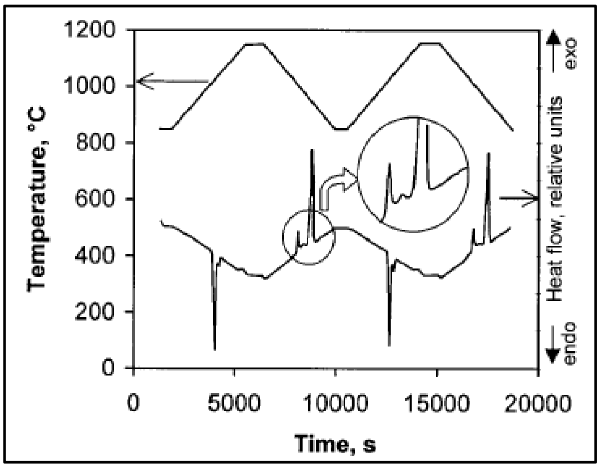

Figure 2.5.13: Differential thermal analysis done on the B2-B19 transformation in a sample with 47 at.% Pt of Ti-Pt alloys [64].

Rotaru *et al.* [65] did some experimental work on equiatomic Ti-Pt alloys with an average Ti content of between 49.55 and 50.11 at.%. The DSC revealed two endothermic peaks upon heating (1016 ^{o}C) with a latent heat of 2.7 J/g and one larger peak (1035 ^{o}C) with a latent heat of 23.4 J/g, Figure 2.5.14. The cooling curve displayed a single large exothermic peak, with an onset at 1015 ^{o}C and an area of 28.7 J/g, and a very shallow exothermic bump around 987 ^{o}C. They reported that the large peaks upon cooling and heating on the DSC corresponded to B2 to B19 martensitic transformation with a hysteresis of 20 ^{o}C, Figure 2.5.14. The small endothermic peak was associated with the shallow exothermic bump during cooling and belonged to the same reversible transformation. The presence of the latter small peaks in DSC runs was related to the formation of the new long period microtwin (LP) confirmed using high-resolution transmission electron microscopy (HRTEM). The formation of LP structure was due to small and local inhomogeneities in the composition and stress leading to the formation of mixed B19 and LP regions where no difference in composition between the LP and B19 martensitic structures could be measured.

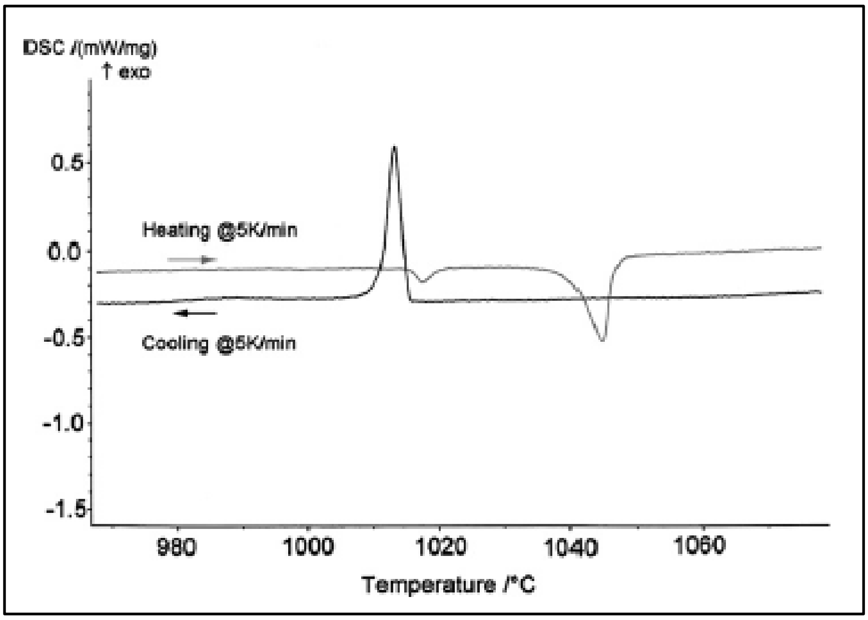

Figure 2.5.14 : Heating and cooling DSC cycles of the as-cast Ti-Pt alloy [65].

2.5.1.3. Shape memory properties of TiPt

Yamabe-Mitarai *et al.* [66] investigated the shape memory properties of TiPt using loading-unloading compression tests at room temperature and 1123 K (850 °C), both temperatures were below the martensitic transformation temperature, Figure 2.5.15. At room temperature (Figure 2.5.15(a)), the stress was applied until the strain reached about 0.9%, and then the stress was removed. The detwinning stress was about 200 MPa during loading. A recovery strain of about 0.55% for a plastic deformation strain of 0.65% was observed during unloading [66]. The test at 1123 K (850 °C) showed that the detwinning stress for the martensite phase was about 50 MPa and the applied stress was removed after a deformation strain of about 5%, Figure 2.5.15b. A strain recovery of 1.9% for a plastic deformation strain of 2.6% was observed during unloading.

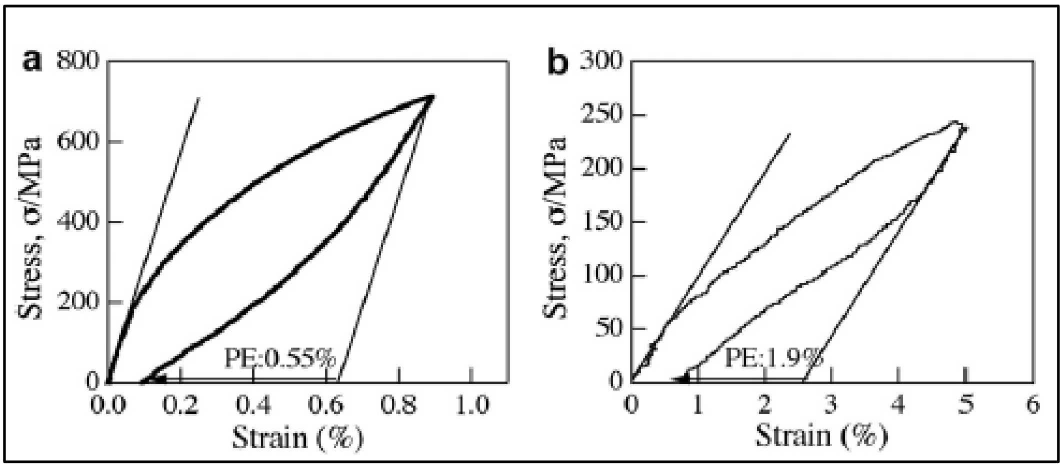

Figure 2.5.15: Loading-unloading compression tests at (a) room temperature and (b) 1123 K [66].

Yamabe-Mitarai *et al.* [66] investigated the strain recovery / SME of Ti-Pt by applying strains of 6% and 5% at room temperature and 1123 K (850 °C), Figure 2.5.16. Shape recovery was observed in the TiPt sample deformed at room temperature and at 1123 K after heating to above the martensitic transformation temperature (1523 K) for 1 hour [66]. In Figure 2.5.16, the asterisk indicates that cyclic tests were carried out for the sample and symbols without an asterisk indicate that a single compression test was carried out. The maximum recovery strain of TiPt was about 1% and decreased beyond 2% of residual strain. The maximum strain recovery ratio was about 60% after deformation at room temperature. After deformation at 1123 K, the strain recovery of the TiPt phase was about 0.2% for a residual strain of 1.7%. The strain recovery ratio was 11% and it was lower than that at room temperature due to a decrease in the yield strength at 1123 K (50 MPa). They mentioned that shape recovery of a SMA could be improved by training treatment such as work hardening, precipitation hardening and microstructure control by heat treatment [66].

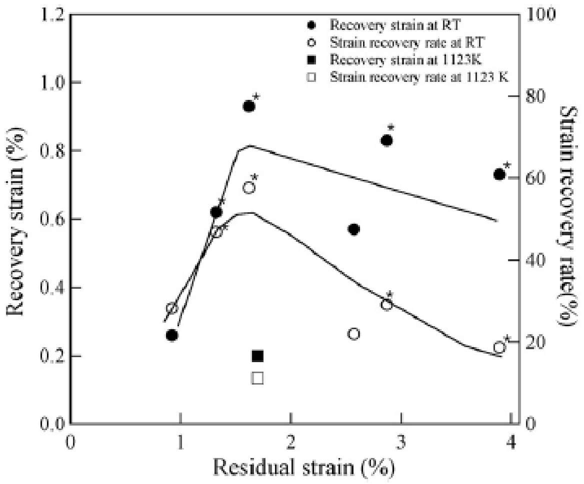

Figure 2.5.16: Strain recovery ratio and recovery strain of TiPt sample by heating in the austenite phase after deformation in the martensitic state related to residual stress [66].

2.5.2. The effect of adding alloying elements on the shape memory properties of Ti-Pt alloy

Although Ti-Pt alloys have the potential for use in high temperature shape memory applications, the high cost of Pt and its negligible shape memory effect could limit their practical application. The high cost of Pt could be addressed by the addition of cheaper alloying elements that do not alter the transformation temperature significantly such that the resulting alloy can still find applications at high operating temperatures. The negligible shape memory effect was attributed to the low critical stress for slip deformation compared to the stress required for martensitic transformation. The addition of alloying elements has been suggested as one of the several alternative ways of improving transformation temperatures and mechanical properties of shape memory alloys [10,13,18,19,31,67,68].

Prior to the addition of an alloying element by substitutional solid solution, the alloying element needs to give maximum solubility when replacing either Ti or Pt so that there is no formation of intermetallic compounds that could affect the shape memory properties of the Ti-Pt alloy. Hume-Rothery alloying rules can be partially used to determine several factors of solubility limit in alloys[69]. The Hume-Rothery rules state what an alloying element should satisfy to achieve maximum solubility as follows [69]:

- Atomic size factor rule: Extensive substitutional solid solution occurs only if the relative difference between the atomic radii of the solute and solvent atoms is less than 15 %. The mismatch between the solute and solvent atoms is calculated using the equation:

$$\frac{r_{solute} - r_{solvent}}{r_{solvent}} \times 100 \qquad (2.5.2)$$

- Crystal structure rule: The crystal structure of the two elements should be the same for appreciable solid solubility.
- Valency rule: The solute and solvent atoms should have the same valency in order to achieve maximum solubility.
- The electronegativity rule: The two elements should have a similar electronegativity so that intermetallic compounds do not form. Electronegativity differences close to zero gives maximum solubility.

The effect of adding alloying elements on the martensitic transformation temperatures of shape memory alloys can be explained using the dependence of transformation temperature on the number (e_v/a) and concentration (C_v) of valence electrons with respect to the change in composition [70]. For example, in the Ni-Ti alloy, it was shown that the transformation temperature was related to whether the number of valence electrons per atom of the alloy is (e_v/a) = 7 or (e_v/a) ≠ 7 [70]. It was found that by increasing the valence electron concentration of Ni-Ti based alloys, the transformation temperatures decrease because of a higher bulk modulus and therefore higher shear and elastic moduli. The bulk modulus is a measure of resistance of a solid to volume change and the shear modulus is a measure of resistance to shape change [70]. The higher elastic modulus of the B2 phase crystal due to its strong bonds increase the resistance to shear and shape change, which is responsible for the martensite transformation.

The valence electron per atom and concentration of valence electrons can be calculated using the formulae [70]:

$$\frac{e_v}{a} = f_A e_v^A + f_B e_v^B + f_C e_v^C + \cdots \qquad (2.5.3)$$

$$C_v = \frac{e_v}{e_t} = \frac{f_A e_v^A + f_B e_v^B + f_C e_v^C}{f_A Z_A + f_B Z_B + f_C Z_C} \qquad (2.5.4)$$

where f_A, f_B and f_C represent the atomic fractions of A, B and C elements in the alloy, e_v^A, e_v^B and e_v^C are the corresponding number of valence electrons of elements A, B and C. The Z_A, Z_B and Z_C represent the atomic numbers of elements A, B and C respectively.

The effect of a ternary alloying element on the microstructure of Ti-30Ni-20Pt alloy was investigated by Ramaiah *et al.* [15] using an optical microscope. The resultant microstructure in the as-cast condition was inhomogeneous, consisting of a dendritic structure with interdendritic regions, Figure 2.5.17. They reported that partitioning of alloying elements during solidification occurred and interdendritic regions were rich in Ti and depleted in Pt resulting in more phases in the interdendritic regions. The homogenisation treatment of the cast sample at 1050 °C for times of above 48 hours resulted in the dissolution of the dendritic structure and the matrix was homogeneous and consistent in composition, shown in Figure 2.5.18. There was precipitation of $Ti_2(Ni,Pt)$ intermetallic phase at the grain boundaries on the homogenized sample. The presence of a similar phase was reported by Padulla ll *et al.* [16], where it was attributed to internal oxidation of the system.

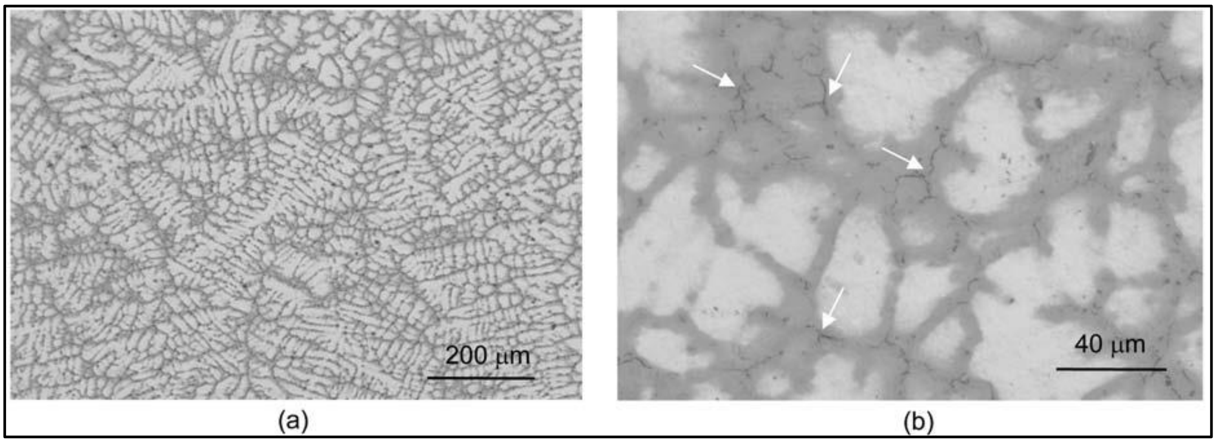

Figure 2.5.17: Optical micrographs showing (a) as-cast structure and (b) partitioning of alloying elements at the interdendritic regions of Ti-30Ni-20Pt alloy [15].

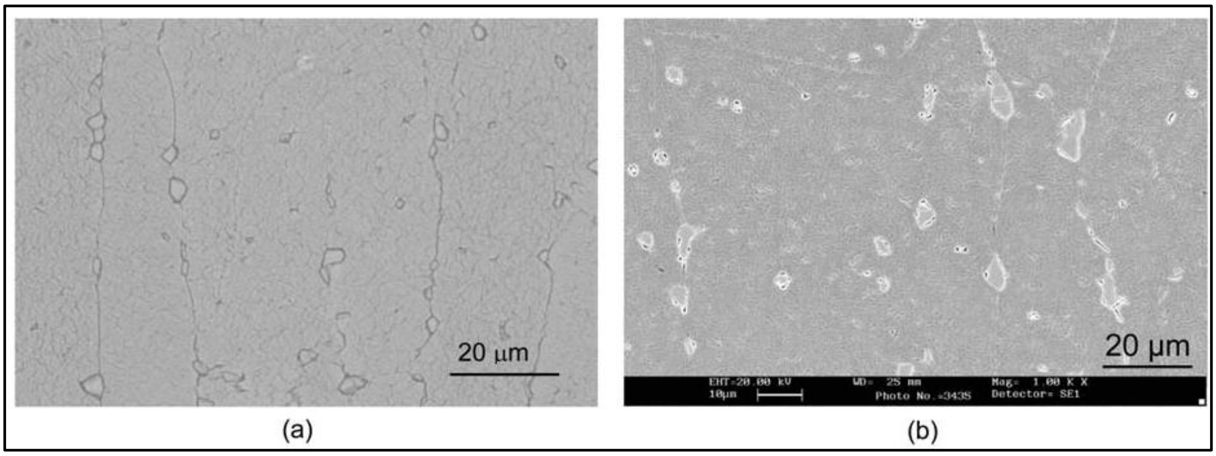

Figure 2.5.18: Homogenized microstructure of Ti-30Ni-20Pt, (a) optical microscope image and (b) scanning electron microscope image [15].

Yamabe-Mitarai *et al.* [20] reported that ternary alloying of Ti-Pt alloys with 5 at.% of Zr, Hf, Ru, and Co decreased the M_s temperature, but it increased with the addition of Ir, Figure 2.5.19(a) [20]. Zirconium and Hf belong to the same group as Ti on the periodic table (group IV) having four valence electrons, so they replace Ti, whereas Ru, Ir and Co are in the 8th and 9th group, close to Pt, meaning they replace Pt [71]. The decrease in transformation temperatures was also observed in Ti-Pd alloys after replacing Ti with 5 and 10 at.% Zr and was. The larger atomic radius of Zr (0.160 nm) than those of Ti (0.147 nm) and Pd (0.137 nm) causes large distortions of the lattice and result in the effective solid solution strengthening of both the martensite and parent phases [67]. The decrease in transformation temperature when Ru and Co were replacing Pt was attributed to the high stability of the B2 high temperature phase [20].

The actual shape recovery strain and ratio of equiatomic Ti-Pt alloy was close to 0% and it was not improved by the addition of 5 at.% Ir, Figure 2.5.19(b) and (d). However, the addition of 5 at% Zr, Hf, Ru and Co led to small improvements in the shape recovery strain and ratio, which also improved the shape memory effect of the alloy. The addition of Zr, Ru, Co and Hf to Ti-Pt alloys resulted in a decrease in the martensitic transformation temperatures ranging between 900 and 950 ^{o}C. The addition of Zr, Ru, Co and Hf resulted in the improvement of shape recovery strain and shape recovery ratio from almost 0% and 10% in Ti-Pt to between 1-2% recovery strain and 40-60% shape recovery ratio when compression tests were performed below M_{f-50} temperatures of the ternary alloys. However, the shape recovery strain and shape recovery ratio of Ti-Pt-Ir remained unchanged at about 10%. Therefore, Zr and Hf were the most effective in improving the shape memory behaviour of Ti-Pt alloys, Figure 2.5.19(b).

The transformation hysteresis of the Ti-Pt alloy was increased with the addition of Zr, Hf, Co, Ru, and Ir alloying elements, which could lead to a higher driving force for the martensitic transformation, Figure 2.5.19(c). A wider hysteresis could be a problem in actuation applications where a narrow hysteresis is needed for faster response during actuation [21].

On the mechanical properties, Yamabe-Mitarai [20] did not observe the double yield behaviour in the stress-strain curve of the martensite phase with Ti-Pt and Ti-Pt-Ir alloys. However, the addition of Zr, Hf, Ru and Co did result in a double yielding behavior and an increase in yield strength as compared to binary Ti-Pt alloy, Figure 2.5.19(e). The addition of Zr to Ti-Pt alloys led to the highest increase in the yield strength of the martensite phase. The addition of Co did not change the yield strength of the Ti-Pt martensite phase. The increase in the yield strength and detwinning stress with the addition of Hf and Zr was attributed to the atomic sizes in comparison with that of Ti and Pt. The atomic sizes of Zr (0.160 nm) and Hf (0.159 nm) are larger than that of Ti (0.147 nm) and Pt (0.139 nm), meaning that Zr and Hf will cause larger lattice distortions while substituted for Ti. Ruthenium (0.134 nm) and Ir (0.136 nm) will have a smaller effect in the yield strength when substituted for Pt since its atomic sizes is smaller. The difference in atomic size was proposed as a strengthening effect of the martensite and austenite phases through solid solution strengthening.

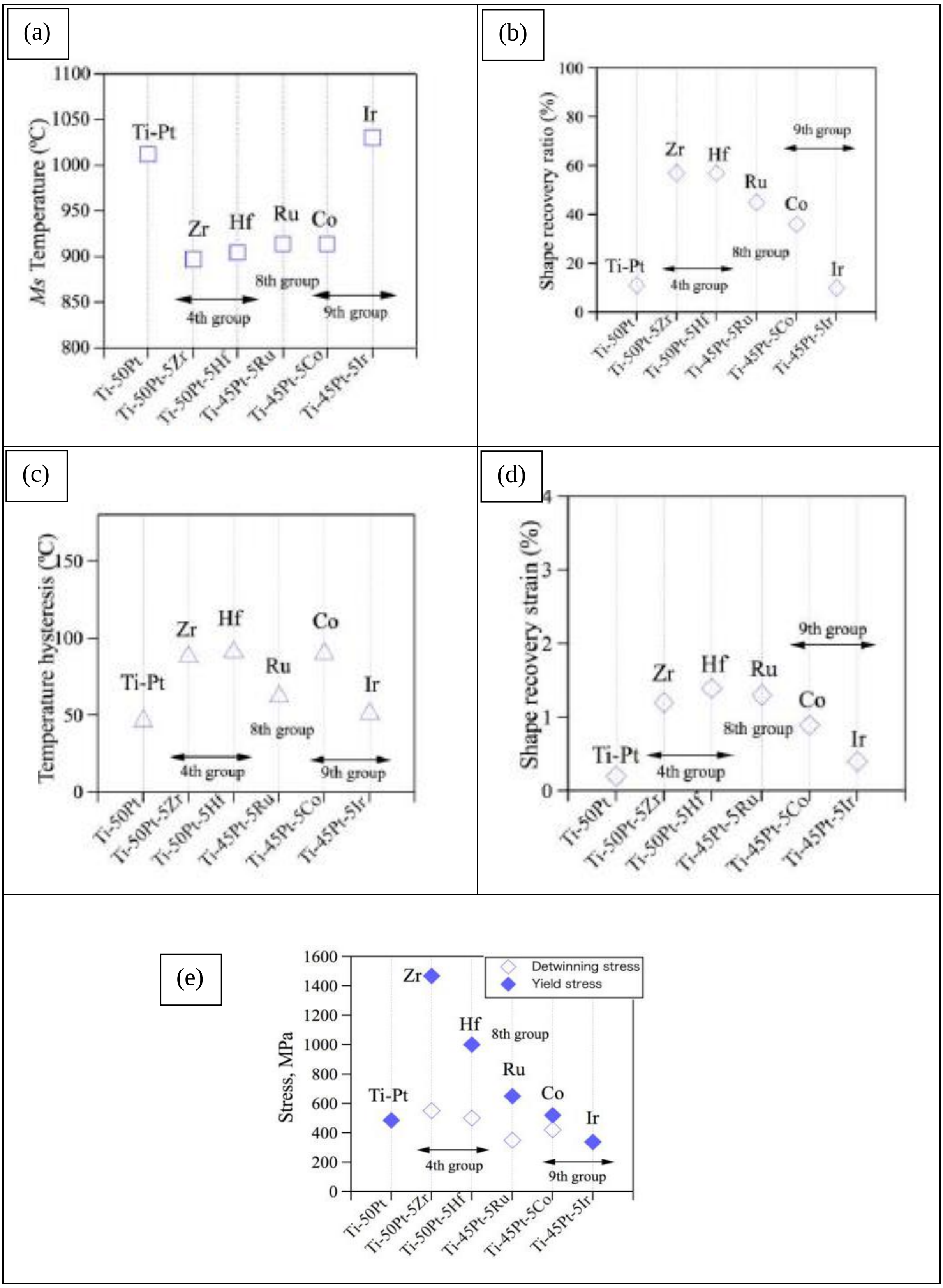

Figure 2.5.19 : The effect of ternary alloying on the a) M_s temperatures, b) shape recovery ratio (shape memory effect), c) temperature hysteresis, d) detwinning stress and yield stress and e) shape recovery strain of Ti-Pt alloys [20].

Mashamaite *et al.* [72] used the first principles approach to investigate the effect of ternary alloying with Zr, Hf, Co, Ru Cu on the equiatomic B19 Ti-Pt alloy while substituting for Pt. They confirmed that partial substitution of Pt with 5 at.% Ru resulted in higher transformation temperatures. However, all the other alloying elements (Co, Cu, Zr, Hf) resulted in lower transformation temperatures than binary TiPt, which was in agreement with what Yamabe-Mitarai *et al.* [20] observed experimentally. They attributed this behavior to the highest shear modulus (C') that Ru (92) exhibits compared to Cu (89), Hf (80), Zr (78) and Co (85). In addition, Ru had the most stable structure and displayed the lowest heats of formation (0.8640 ev/atom), Figure 2.5.20. The partial substitution of Pt with Cu and Co was more stable than Zr and Hf, meaning that the transformation temperatures of substituting Pt with Cu and Co are lower than that for Zr and Hf.

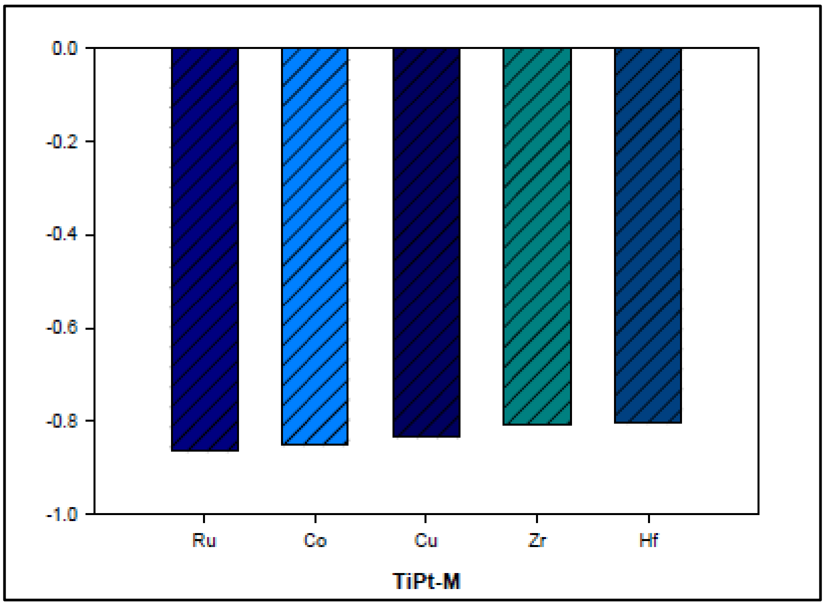

Figure 2.5.20: The predicted heats of formation of Ti-Pt alloys when ternary alloyed with 5 at.% of Ru, Co, Cu, Zr and Hf while partially substituting Pt [72].

Yamabe-Mitarai *et al.* [23] investigated the effect of adding varying contents of Ir (12.5, 25 and 37.5 at.%) on the mechanical properties of Ti-Pt shape memory alloys by using a DTA, dilatometer and TEM when Ir was replacing Pt. They reported that all alloys had a twinned microstructure consisting of coarse twins with various widths depending on the composition of the alloy, Figure 2.5.21. Each coarse twin had a finely twinned internal structure. The twinning morphology in the alloys is a typical requisite for thermoelastic-transformed martensite [23,34]. This similar martensitic transformation was also observed in the Ti-rich Ti-Pt-Ir ternary alloy [34], where several straight lines similar to twin structures were observed in the bright phase regions of Ti-27Pt-13Ir, Ti-22Pt-22Ir and Ti-13Pt-27Ir alloys heat treated at 1250 °C for 100 hours followed by ice-water quenching, Figure 2.5.22. Figure 2.5.22 also reveals that the resultant microstructure consisted of light Ti(Pt,Ir) and dark Ti_3(Pt,Ir) phases.

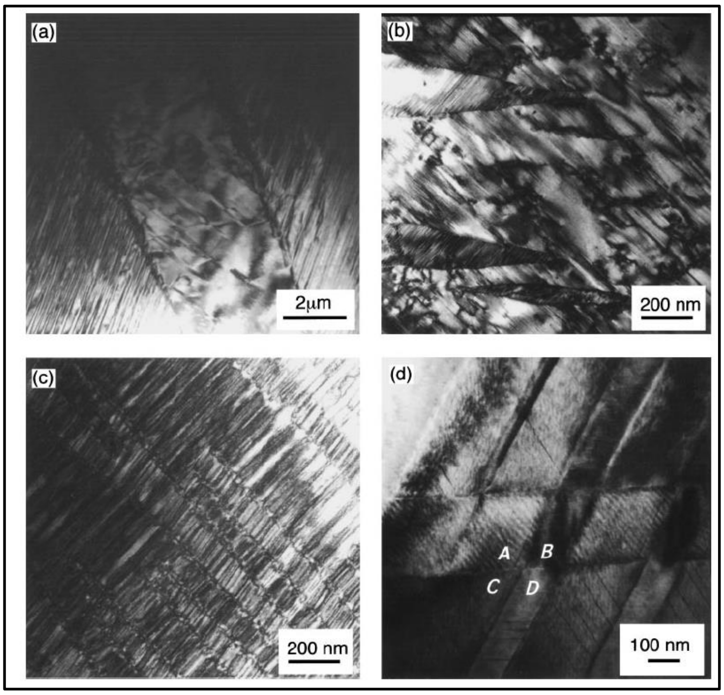

Figure 2.5.21: TEM images of (a) Ti-50Pt, (b)Ti-37.5Pt-12.5Ir, (c) Ti-25Pt-25Ir and (d) Ti-12.5Pt-37.5Ir heat treated at 1250 °C for 24 hours followed by ice water quenching, note that the magnification is not the same [23].

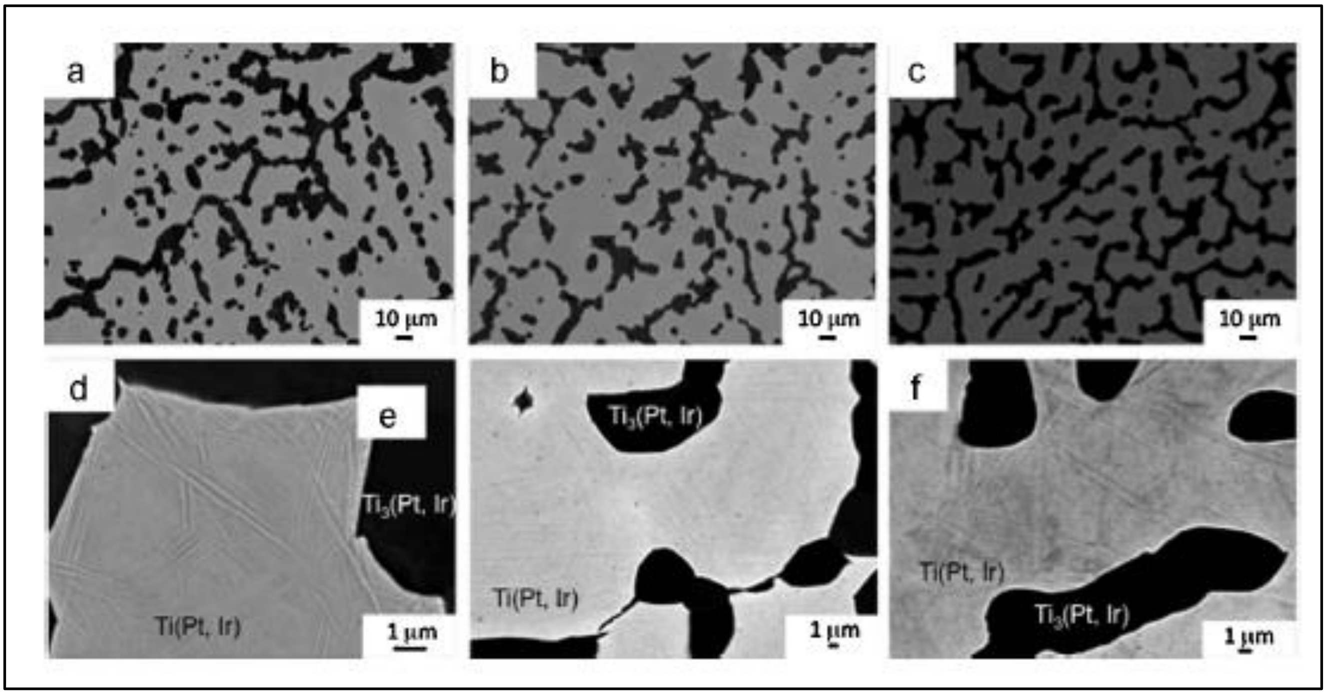

Figure 2.5.22: Backscattered electron images at low and high magnification of (a) & (d) Ti-27Pt-13Ir, (b) & (e) Ti-22Pt-22Ir, and (c) and (f) Ti-13Pt-27Ir alloys heat treated at 1250 °C for 100 hours followed by ice-water quenching [34].

Yamabe-Mitarai *et al.* [23] found that transformation temperatures were increasing with increasing Ir content, giving the alloys a higher possibility for use in high temperature applications, Figure 2.5.23. The thermal hysteresis calculated using the equation A_f - M_s [47] was 68 ^{o}C for binary Ti-Pt alloys,103 ^{o}C for Ti-37.5Pt-12.5Ir, 80 ^{o}C for Ti-25Pt-25Ir and 34 ^{o}C for Ti-12.5Pt-37.2Ir. This means that with Ir concentrations of above 12.5 at.%, the thermal hysteresis was narrow.

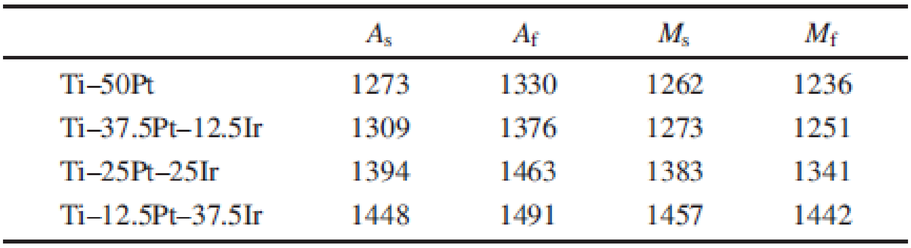

	A_s	A_f	M_s	M_f
Ti–50Pt	1273	1330	1262	1236
Ti–37.5Pt–12.5Ir	1309	1376	1273	1251
Ti–25Pt–25Ir	1394	1463	1383	1341
Ti–12.5Pt–37.5Ir	1448	1491	1457	1442

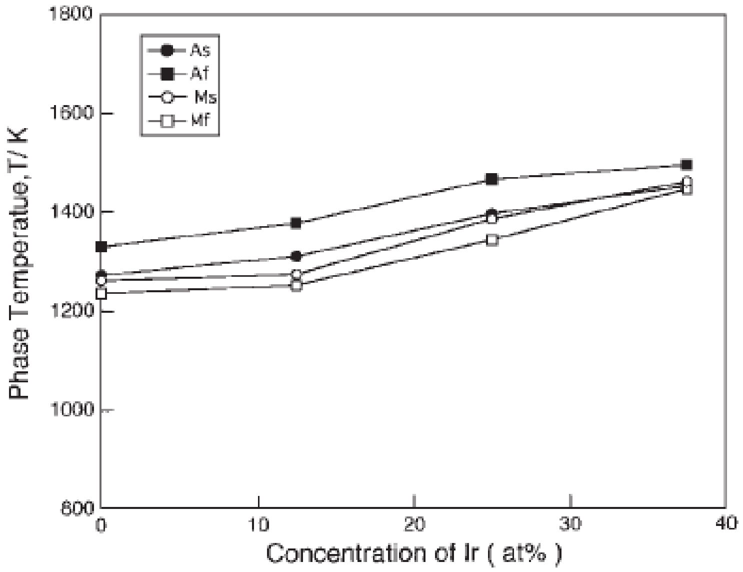

Figure 2.5.23: Phase transformation temperatures in (K) as a function of Ir concentrations on Ti-Pt alloy [23].

In the same study, Yamabe-Mitarai *et al.* [23] also investigated the mechanical properties using thermal expansion tests (at temperatures from 27 to 1327 ^{o}C) and they found that Ti-37.5-12.5Ir and Ti-25Pt-25Ir exhibited the highest shape recovery strain of 0.9%, Figure 2.5.24. Binary Ti-Pt alloy exhibited a shape recovery strain of 0.6% and concentrations of Ir above 25 at.% showed a decrease in the shape recovery strain of the material.

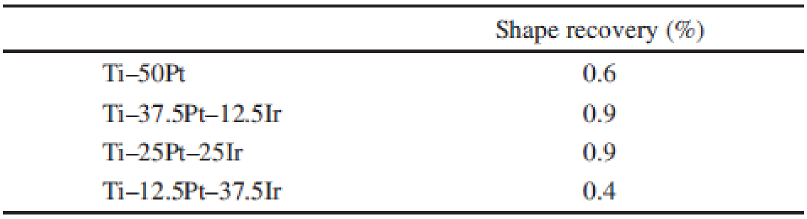

	Shape recovery (%)
Ti–50Pt	0.6
Ti–37.5Pt–12.5Ir	0.9
Ti–25Pt–25Ir	0.9
Ti–12.5Pt–37.5Ir	0.4

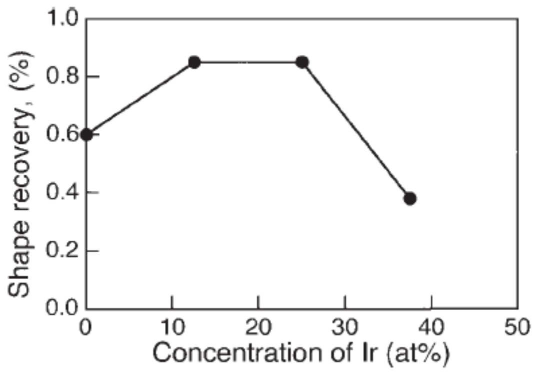

Figure 2.5.24: The shape recovery of Ti-50Pt and Ti-50(Pt, Ir) measured by the thermal expansion test [23].

The loading and unloading compression tests were also carried out at temperatures below the M_s, between A_s and A_f transformation temperatures and above A_f with a strain rate of 3 x 10^{-4}/s in Ti-50Pt and Ti-50(Pt, Ir) alloys. In the binary Ti-50Pt alloy, there was no double yield behaviour of the martensite phase during elastic deformation. The shape recovery and superelasticity was 0% under all heat treatment conditions, Figure 2.5.25(1) and Table 2-4. Iridium concentrations of above 12.5 at.% resulted in the reorientation of the martensite variants, signifying the double yielding behaviour below the (M_f) temperature which is a prerequisite for the shape memory effect. The resultant detwinning strength of the martensite phase led to shape recovery, which was reported to increase with higher additions of Ir in the alloy. The addition of Ir increased both the detwinning stress for reorientation of martensite variants and yield strength at higher temperatures, meaning that the critical stress due to slip of dislocations increased by the addition of Ir at higher temperatures. The highest shape recovery was in Ti-25Pt-25Ir which was 4% under the M_f and showed 1.8% shape recovery by reheating to A_f after a loading-unloading test at a temperature between the A_s and A_f, Figure 2.5.25(3) and Table 2-4. Also, when heating above the A_s temperature, Ti-Pt alloys with Ir additions over 25 at.% had a high shape recovery, Table 2-4. Overall, these results suggested that ternary alloying of Ti-Pt alloys with Ir has high potential to be used as high-temperature shape memory alloys.

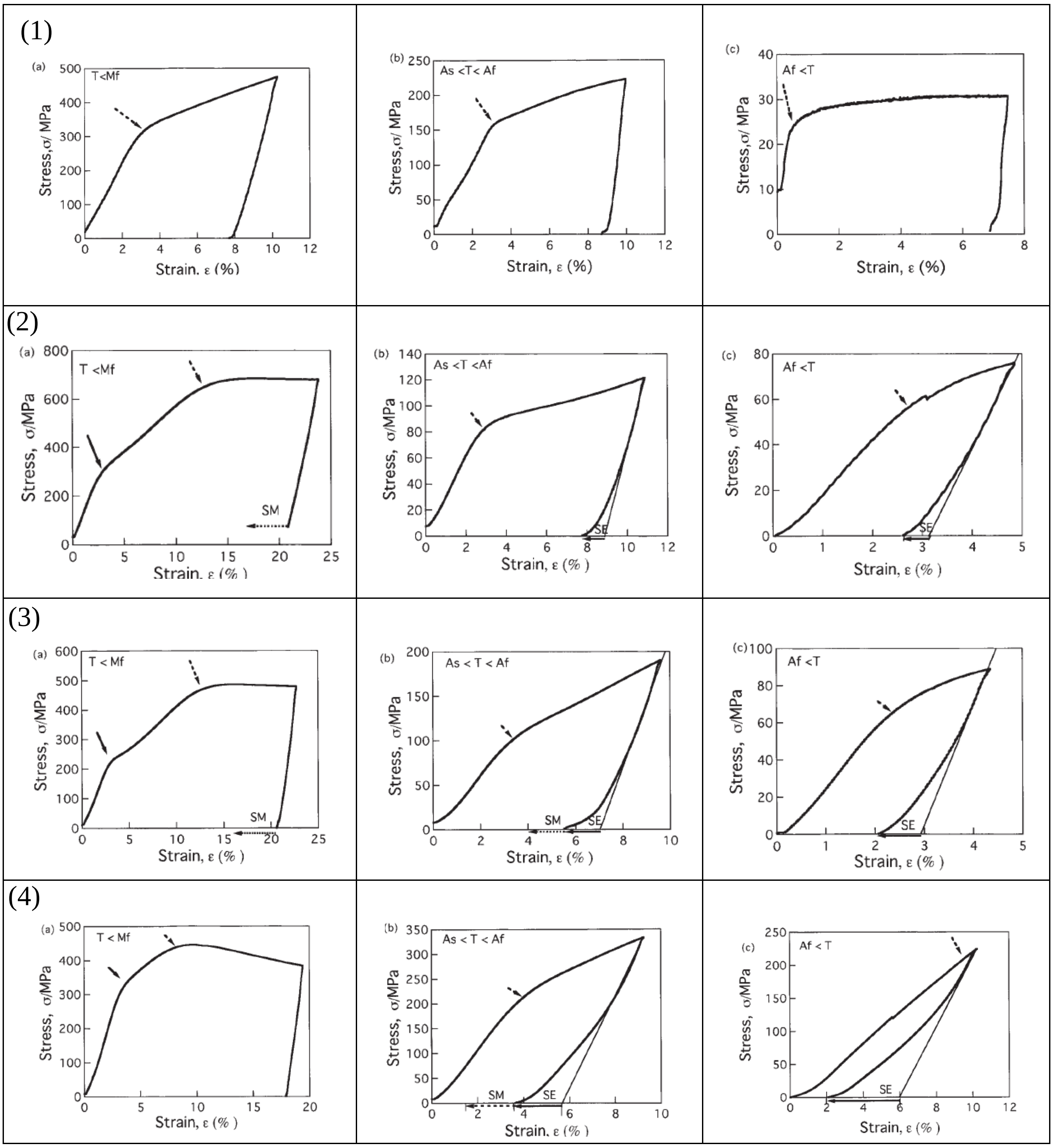

Figure 2.5.25: Stress-strain curves of (1) Ti-50Pt, (2) Ti-37.5Pt-12.5Ir, (3) Ti-25Pt-25Ir and (4) Ti-12.5Pt-37.5Ir carried out at temperatures (a) under M_f, (b)between A_s and A_f and (c) above A_f temperatures [23].

Table 2-4: A summary of shape recovery by reheating after the loading-unloading compression tests in Ti-50(Pt, Ir) alloys [23].

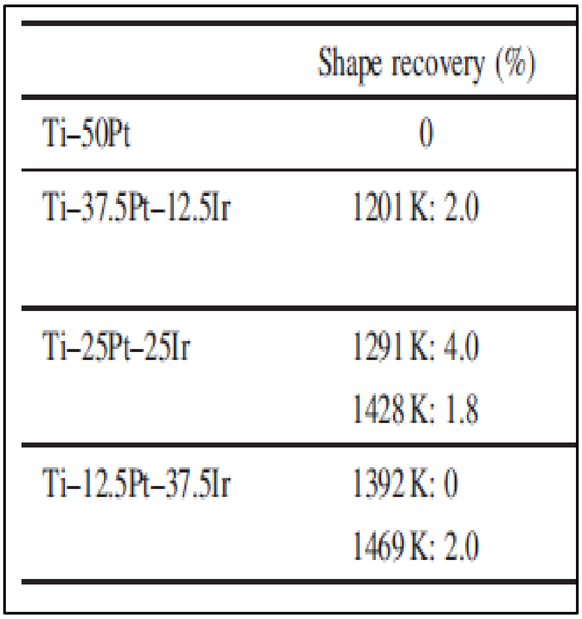

	Shape recovery (%)
Ti–50Pt	0
Ti–37.5Pt–12.5Ir	1201 K: 2.0
Ti–25Pt–25Ir	1291 K: 4.0 1428 K: 1.8
Ti–12.5Pt–37.5Ir	1392 K: 0 1469 K: 2.0

2.5.3. Ternary alloying of shape memory alloys with vanadium (V)

2.5.3.1. Vanadium in Ti-Ni alloys

Besides the low cost of V, Quin Mary [73] and Yamauchi *et al.* [74] patented that the addition of V to Ti-Ni shape memory alloys improved the workability of the alloys. Quin Mary [73] studied the effect of V additions up to 30 at.% on the shape memory behaviour by melting pure Ti, Ni and V in desired proportions to produce Ti-Ni-V alloy ingots shown in Table 2-5. Figures 2.5.26(a) through 2.5.26(e) depict typical stress-strain curves of shape memory alloys at various testing temperatures, which were used to describe the stress-strain behaviour of the Ti-Ni-V alloys. In Figure 2.5.26(a), the temperature is below M_s and the alloy was fully martensitic where it deformed by detwinning below the elastic limit. The deformation at this temperature was recovered when the alloy is heated above A_s temperature and gives rise to the shape memory behaviour.

In Figure 2.5.26(b), the temperature is between M_s and M_d (maximum temperature where martensite may be stress induced). In this state, the alloy is initially austenitic and the application of stress results in the formation of martensite with some deformation taking place. Because the alloy is below As temperature, the deformation is not recoverable and heating the alloy above the As temperature will result in the transformation back to austenite. If the sample is not restricted, the original shape will be fully recovered, and if it is restrained, it will recover to the extent permitted by the restraint. However, if the alloy is cooled down to the deformation temperature, the stress produced will be constant regardless of the strain, provided that the strain lies within the plateau region of the stress-strain curve. In Figure 2.5.26(c), the test temperature is as in 2.5.26(b) but above the A_s temperature. In this condition, the SIM is thermally unstable and reverts to the austenite when the stress is removed. This behavior is called the stress induced martensite pseudoelasticity. Figure 2.5.26(d) shows a test temperature M_d where some stress induced martensite can be formed but the stress level for martensite formation is close to the austenite yield strength of the alloy, resulting in the formation of both the plastic and stress induced martensite (SIM) deformation. SIM deformation can be recovered. Figure 2.5.26(e) shows a situation where the test temperature was above the M_d where the alloy in the austenite phase yields plastically when stressed beyond its elastic yield point and the deformation is not recoverable.

From Table 2-5, Quin Mary [73] showed that alloys with an M_s temperature higher than -40 ^oC but lower than 20 ^oC showed the B- and C-type (pseudoelasticity) behavior at test temperatures of 20 and 40 ^oC. Alloys with an M_s temperature of -42 ^oC showed a D-type behavior at 0 and 20 ^oC. Therefore, alloys with an M_s temperature below -40 ^oC would exhibit a D- or E-type behaviour in the temperature range of interest. It was worth noting that alloys with an M_s temperature above 20 ^oC exhibits the shape memory behavior A-type at testing temperatures of about 0 and 20 ^oC. The substitution of 4 to 5 at.% V replacing Ti showed predominantly a D-type stress-strain behavior where both recoverable and plastic deformation occur. Quin Mary [73] also reported that addition of more V led to undesirable mechanical properties such that an alloy with 30 at.% V showed a lesser degree of SIM elongation and a higher yield strength for the SIM transformation than alloys of lower V contents.

Table 2-5: Martensite start temperature and mechanical behaviour of Ti-Ni alloys with varying content of V [73].

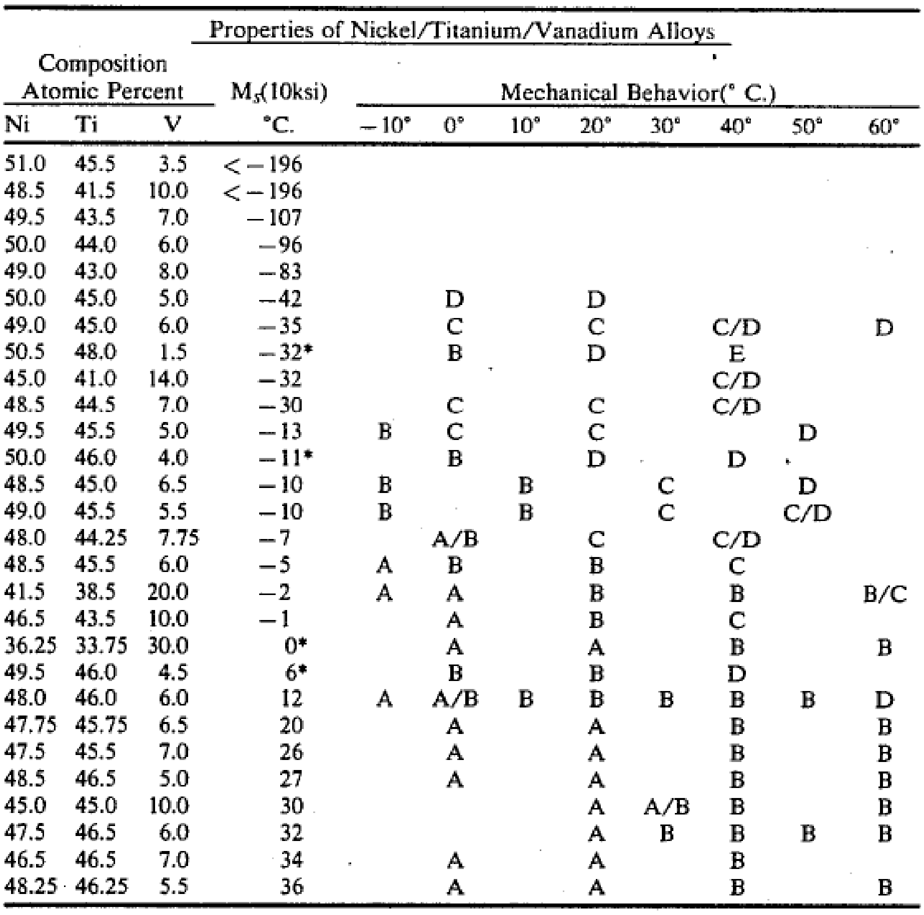

Properties of Nickel/Titanium/Vanadium Alloys

Composition Atomic Percent			M_s(10ksi)	Mechanical Behavior(° C.)							
Ni	Ti	V	°C.	−10°	0°	10°	20°	30°	40°	50°	60°
51.0	45.5	3.5	< −196								
48.5	41.5	10.0	< −196								
49.5	43.5	7.0	−107								
50.0	44.0	6.0	−96								
49.0	43.0	8.0	−83								
50.0	45.0	5.0	−42		D		D				
49.0	45.0	6.0	−35		C		C		C/D		D
50.5	48.0	1.5	−32*		B		D		E		
45.0	41.0	14.0	−32						C/D		
48.5	44.5	7.0	−30		C		C		C/D		
49.5	45.5	5.0	−13	B	C		C			D	
50.0	46.0	4.0	−11*		B		D		D		
48.5	45.0	6.5	−10	B		B		C		D	
49.0	45.5	5.5	−10	B		B		C		C/D	
48.0	44.25	7.75	−7		A/B		C		C/D		
48.5	45.5	6.0	−5	A	B		B		C		
41.5	38.5	20.0	−2	A	A		B		B		B/C
46.5	43.5	10.0	−1		A		B		C		
36.25	33.75	30.0	0*		A		A		B		B
49.5	46.0	4.5	6*		B		B		D		
48.0	46.0	6.0	12	A	A/B	B	B	B	B	B	D
47.75	45.75	6.5	20		A		A		B		B
47.5	45.5	7.0	26		A		A		B		B
48.5	46.5	5.0	27		A		A		B		B
45.0	45.0	10.0	30				A	A/B	B		B
47.5	46.5	6.0	32				A	B	B	B	B
46.5	46.5	7.0	34		A		A		B		
48.25	46.25	5.5	36		A		A		B		B

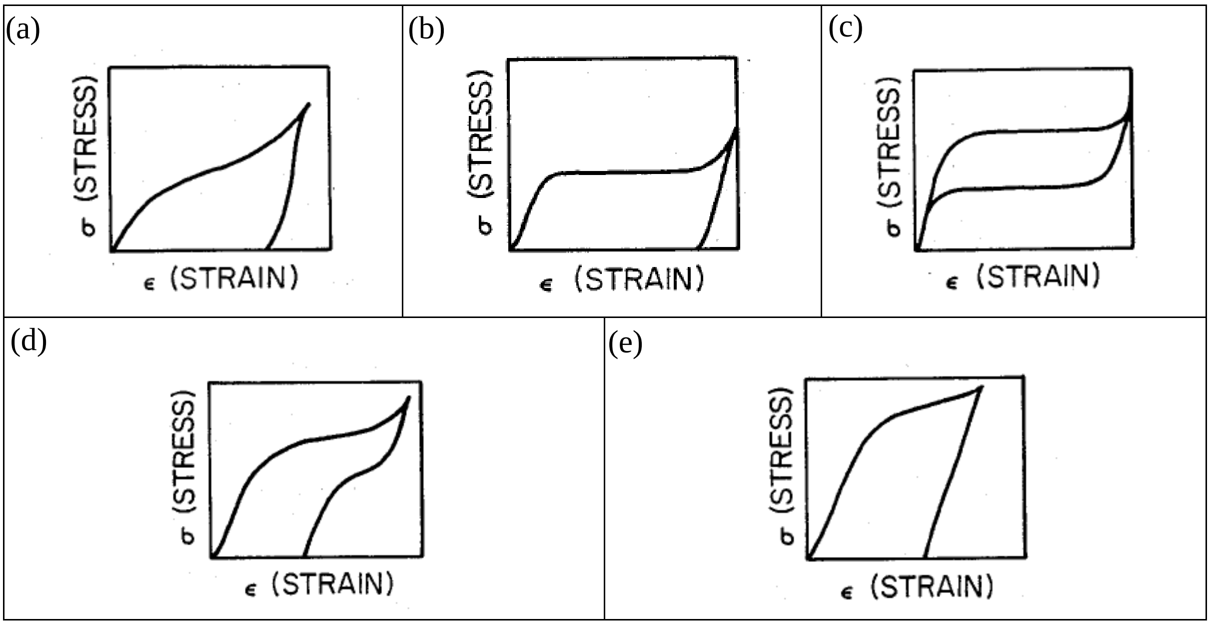

Figure 2.5.26: Typical stress-strain curves for shape memory alloys at various temperatures (a-e) [73].

Yamauchi *et al.* [74] confirmed that the addition of vanadium to Ti-Ni improved its workability and shape memory properties. Figure 2.5.27 shows alloy ingots with related transformation temperatures that were prepared using an induction vacuum furnace, followed by heat treating at 750 °C for one hour by Yamauchi *et al.* [74]. The binary Ni_{50}-Ti_{50} alloy had an A_f and M_s temperature of 65 and 5 °C respectively, which resulted in a transformation thermal hysteresis of 15 °C. Overall, the transformation thermal hysteresis decreased with the addition of V in these Ti-Ni alloys. Good workability and decreased transformation thermal hysteresis were attained for Ti-Ni alloys containing 0.25-2.0 at.% V, with 48.5 at% or more of Ti (balance Ni) and an atomic ratio of Ni/Ti being 0.96-1.02. The addition of V to alloys with a Ni/Ti ratio of 0.96-1.02 increased the M_s temperature, workability and thermal hysteresis of Ti-Ni-V alloys. Ti-Ni-V alloys having a Ni/Ti ratio of 1.02-1.06 were associated with M_s temperatures of room temperature or lower and also exhibited pseudoelasticity at room temperature or lower (Alloy No. 1, 2, 3, 5, 6, 7, 8, 9, 10, 11, 12, 13, 15, 25).

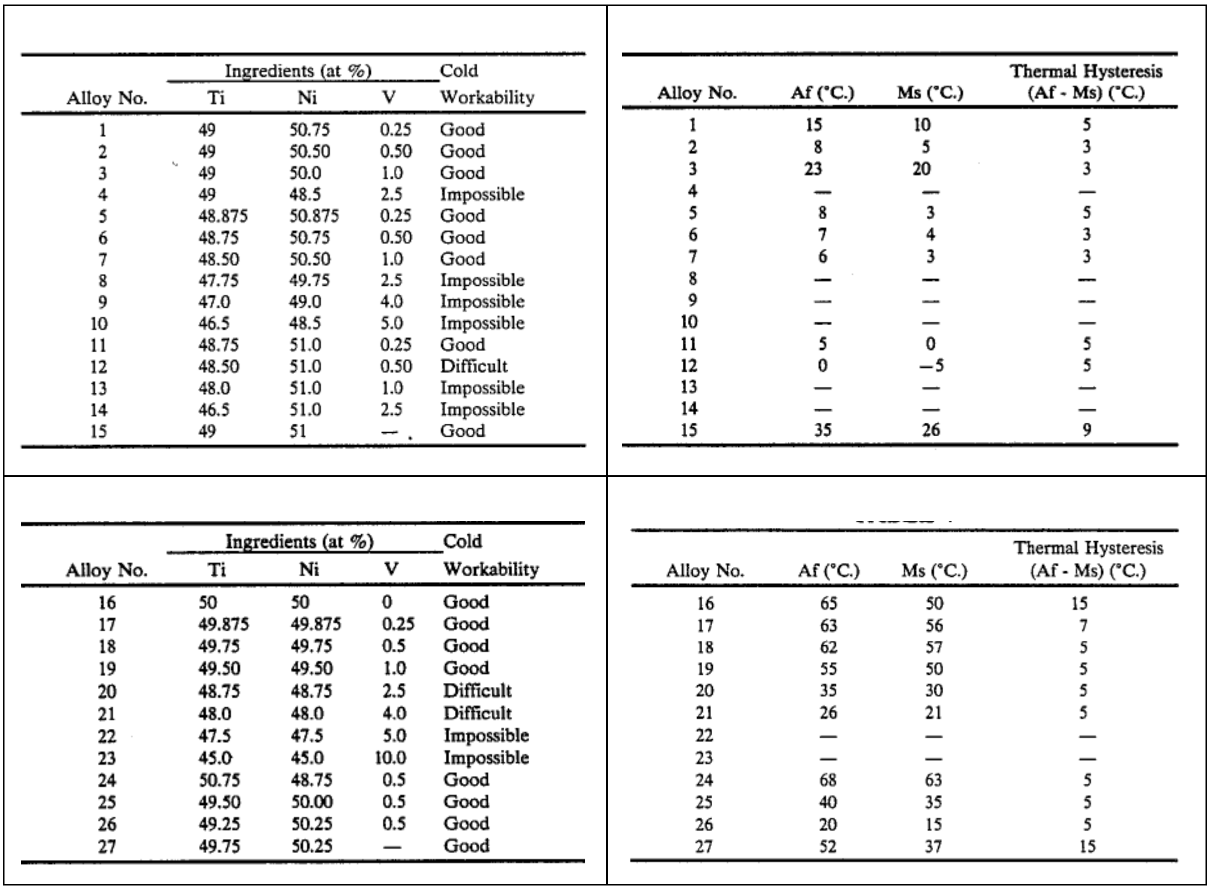

	Ingredients (at %)			Cold
Alloy No.	Ti	Ni	V	Workability
1	49	50.75	0.25	Good
2	49	50.50	0.50	Good
3	49	50.0	1.0	Good
4	49	48.5	2.5	Impossible
5	48.875	50.875	0.25	Good
6	48.75	50.75	0.50	Good
7	48.50	50.50	1.0	Good
8	47.75	49.75	2.5	Impossible
9	47.0	49.0	4.0	Impossible
10	46.5	48.5	5.0	Impossible
11	48.75	51.0	0.25	Good
12	48.50	51.0	0.50	Difficult
13	48.0	51.0	1.0	Impossible
14	46.5	51.0	2.5	Impossible
15	49	51	—	Good

Alloy No.	Af (°C.)	Ms (°C.)	Thermal Hysteresis (Af - Ms) (°C.)
1	15	10	5
2	8	5	3
3	23	20	3
4	—	—	—
5	8	3	5
6	7	4	3
7	6	3	3
8	—	—	—
9	—	—	—
10	—	—	—
11	5	0	5
12	0	−5	5
13	—	—	—
14	—	—	—
15	35	26	9

	Ingredients (at %)			Cold
Alloy No.	Ti	Ni	V	Workability
16	50	50	0	Good
17	49.875	49.875	0.25	Good
18	49.75	49.75	0.5	Good
19	49.50	49.50	1.0	Good
20	48.75	48.75	2.5	Difficult
21	48.0	48.0	4.0	Difficult
22	47.5	47.5	5.0	Impossible
23	45.0	45.0	10.0	Impossible
24	50.75	48.75	0.5	Good
25	49.50	50.00	0.5	Good
26	49.25	50.25	0.5	Good
27	49.75	50.25	—	Good

Alloy No.	Af (°C.)	Ms (°C.)	Thermal Hysteresis (Af - Ms) (°C.)
16	65	50	15
17	63	56	7
18	62	57	5
19	55	50	5
20	35	30	5
21	26	21	5
22	—	—	—
23	—	—	—
24	68	63	5
25	40	35	5
26	20	15	5
27	52	37	15

Figure 2.5.27: Transformation temperatures of Ti-Ni alloys with varying V contents up to 10 at.% [74].

2.5.3.2. Vanadium in Ti-Pd alloys

The addition of V to other high temperature shape memory alloys attracted much research interest [12,21,75–77]. Yamabe-Mitarai [75] investigated the effect of ternary alloying with 5 at.% V, Cr ,Hf, Zr, Nb, Ta, W, Ru, Co and Ir on Ti-Pd. The transformation temperatures of TiPd decreased with the addition of all alloying elements, Figure 2.5.28. Alloying elements such as V, Zr, Hf and Nb are bcc stabilizers in Ti alloys, thus the B2 structure (ordered BCC) was stabilized by the addition of these alloying elements and transformation temperatures decreased [73]. The addition of 5 at.% V widened the thermal transformation hysteresis from 56 to 61 °C, which can limit its application as an actuator at higher temperatures.

Alloy	A_s	A_f	M_s	M_f	A_f - Ms	$\Delta M_s/at\%$
Ti-50Pd	574	590	534	527	56	-
Ti-50Pd-5Zr	484	503	457	439	49	-15
Ti-50Pd-5Hf	481	505	460	429	45	-15
Ti-50Pd-5V	508	523	462	440	61	-15
Ti-50Pd-5Nb	486	508	431	408	77	-20
Ti-50Pd-5Ta	561	579	512	489	67	-4
Ti-50Pd-5Cr	268	356	347	293	9	-37
Ti-50Pd-5Mo	267	383	401	268	-18	-27
Ti-50Pd-5W	558	576	513	492	63	-4
Ti-46Pd-4Ru	440	481	435	392	46	-23
Ti-46Pd-4Co	472	492	454	427	38	-18
Ti-46Pd-4Ir	535	552	510	484	42	-4

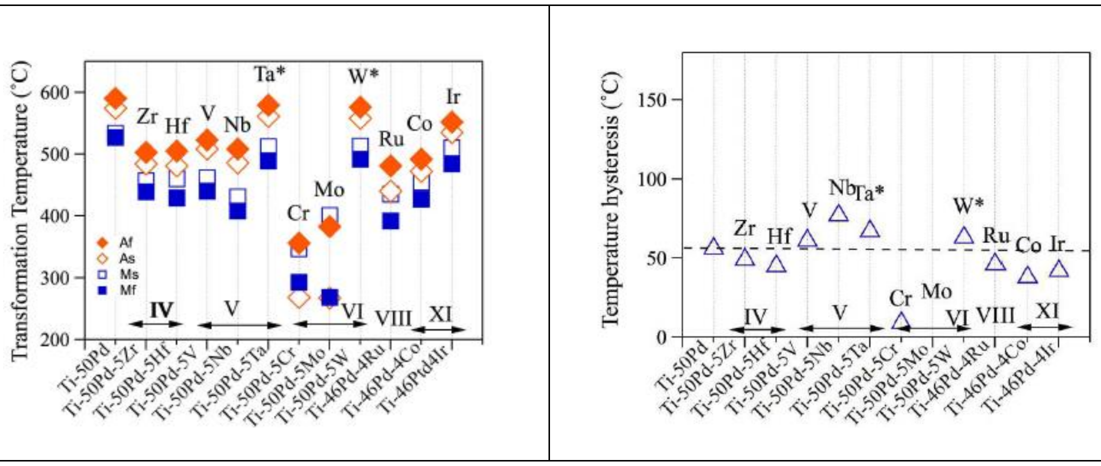

Figure 2.5.28: Martensite transformation temperatures of binary Ti-Pd and Ti-Pd-X alloy samples [75].

However, the yield strength of TiPd martensite was improved by the addition of most alloying elements including V, Figure 2.5.29. It indicated that the addition of alloying elements was effective in suppressing the introduction of plastic deformation, but the detwinning stress was also increased, meaning it would not be easy to change martensite variants. The yield strength of the austenite phase was significantly improved by alloying elements such as V, Cr and Mo. Yamabe-Mitarai *et al.* [20] reported that shape recovery for Ti-Pt alloys is improved when the yield strength of the martensite (M_dy) becomes high, in order to supress plastic deformation. The detwinning stress (M_dT) should be decreasing in order to move martensite variant easily. It means that if M_dT/ M_dy becomes small, shape recovery is expected to be high [20]. In the Ti-Pd system, there was no clear correlation between shape recovery ratio and M_dT/ M_dy. Therefore, they suggested that the presence of precipitates could also contribute to low shape recovery by preventing the reverse martensitic transformation, causing low shape recovery [75].

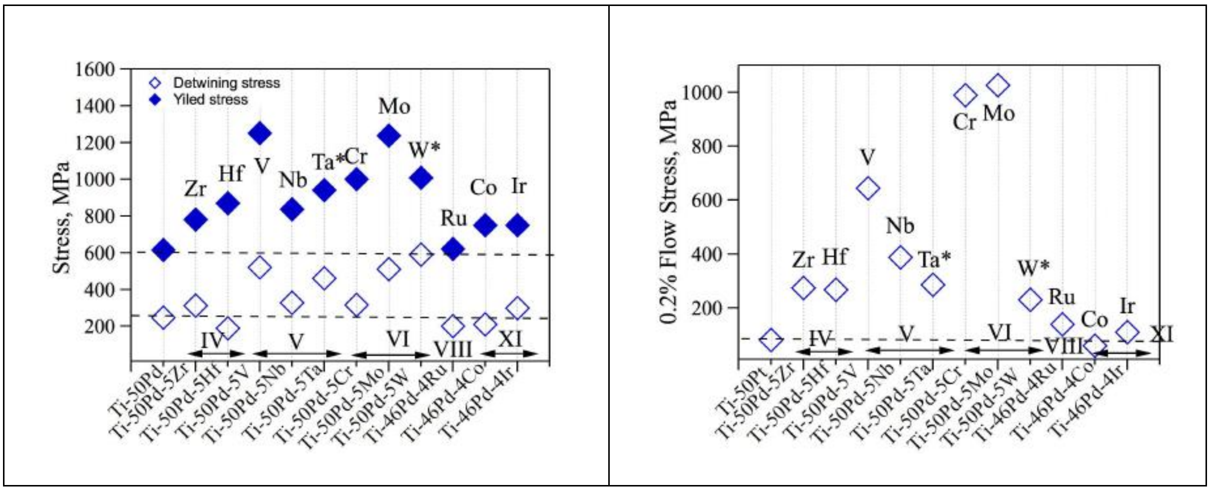

Figure 2.5.29: Yield and detwinning strength of the martensitic TiPd (a) and the austenite phase (b) in Ti-Pd alloys [75].

2.5.3.3. Vanadium in Ti-Pt alloys

Modiba *et al.* [77] investigated the effect of partial substituting Pt with V additions on the elastic constants and electronic structure of the B2 phase in relation to the martensitic transformation temperature and phase stability in Ti-Pt-based alloys using first principles calculations, Table 2-6. The stability of the B2 structure was determined with respect to its equilibrium lattice parameters and elastic constants using the *ab* initio density functional theory (DFT) approach [77]. They reported that the lattice parameter *a* decreased with increasing V content due to the smaller atomic radius of V than Pt. Table 2-6 shows that with increasing V content C_{11} was greater that C_{12}, this suggested that the B2 Ti(Pt,V) phase was mechanically stable, thereby restricting the formation of the martensite phase. The C_{44} elastic constant increased with increasing V concentration, indicating a reduction in the transformation temperature. Therefore, the transformation temperatures of Ti-Pt alloy decreased with increasing V content (6.25, 18.75 and 25 at.% V). The anisotropy ($A = C_{44}/C'$) of the supercell indicates if the martensite formed would be B19 (>3) or B19' (<3). From Table 2-6, the anisotropy of the Ti-Pt-V was less than 3, which suggested a transformation of B2 to B19' structure. Phonon dispersions determined using the DFT approach, in Figure 2.5.30, further confirmed that the reduction of martensitic transformation temperature with increasing vanadium contents was due to the stabilization of the B2 phase. According to Figure 2.5.30, the phonon frequency of Ti-Pt-V with more V (18.25 and 25 at.% V) was positive, showing that the structure was more vibrationally stable with no negative frequency, meaning that higher contents of V when substituting Pt vibrationally stabilises the B2 Ti(Pt,V) phase and lower the transformation temperature of the transforming B19’ martensite structure.

Table 2-6: Lattice parameters (a) in Å, elastic properties Cij in GPa and anisotropy A of Ti_{50}-Pt_{50} with varying additions of V when substituting for Pt [77].

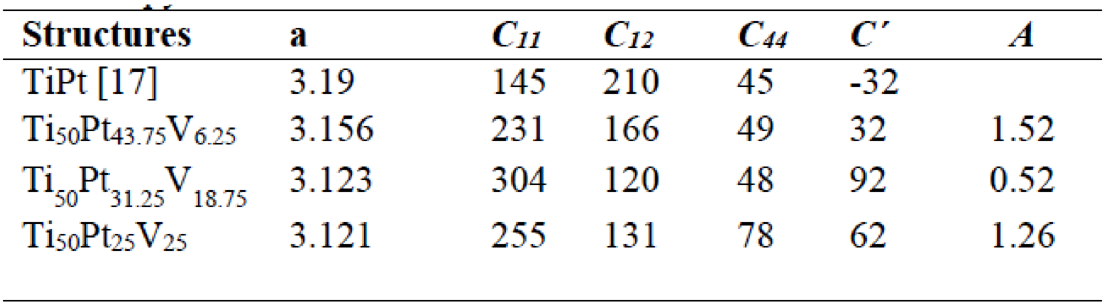

Structures	**a**	C_{11}	C_{12}	C_{44}	C'	A
TiPt [17]	3.19	145	210	45	-32	
$Ti_{50}Pt_{43.75}V_{6.25}$	3.156	231	166	49	32	1.52
$Ti_{50}Pt_{31.25}V_{18.75}$	3.123	304	120	48	92	0.52
$Ti_{50}Pt_{25}V_{25}$	3.121	255	131	78	62	1.26

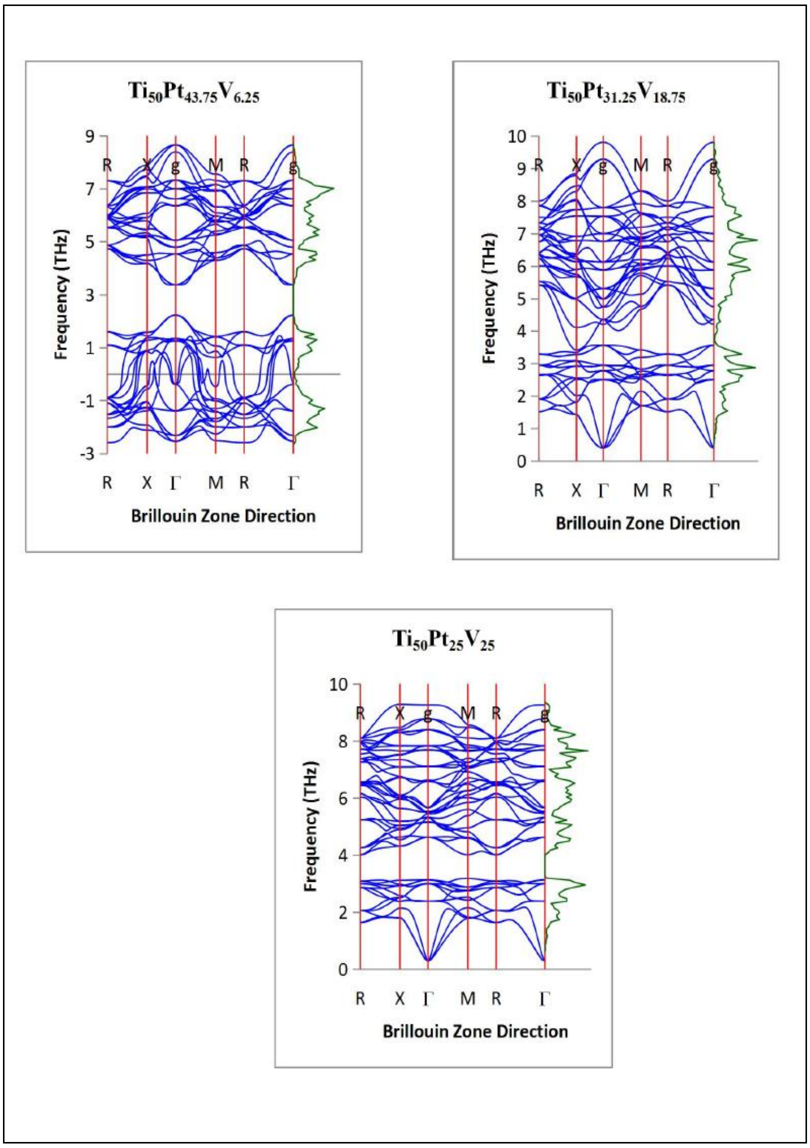

$Ti_{50}Pt_{43.75}V_{6.25}$

$Ti_{50}Pt_{31.25}V_{18.75}$

$Ti_{50}Pt_{25}V_{25}$

Figure 2.5.30: $Ti_{50}Pt_{43.75}V_{6.25}$, $Ti_{50}Pt_{31.75}V_{18.25}$ and $Ti_{50}Pt_{25}V_{25}$'s phonon dispersion curves [77].

Chikosha *et al.* [21] did an experimental study on the effect of 6.25 at.% V on the structure and martensitic transformation temperature of Ti-Pt alloys using X-ray diffraction (XRD), differential scanning calorimetry (DSC) and scanning electron microscopy (SEM) in backscattered mode with an energy dispersive spectrometer (EDS) in the as-cast condition. They reported that B2 TiPt had transformed to a low temperature B19 TiPt structure, which was contradictory to first principles calculations, Figure 2.5.31(a) where Modiba *et al.* [77] reported that an addition of V resulted in the transformation of B2 to B19' TiPt structure. However, the martensitic transformation temperature of TiPt had decreased with the addition of V and this was in agreement with first principles calculations, Figure 2.5.31(b). The thermal hysteresis was widened with the addition of V, which could limit actuation applications. SEM results revealed that the binary Ti-Pt and Ti-Pt-V alloys had multiple phases in the as-cast condition, Figure 2.5.31(c). Chikosha *et al.* [21] reported that the as-cast structure consisted of Ti(Pt,V) dendrites with eutectic regions consisting of Ti(Pt,V), $(Ti,V)_3Pt$ and $(Ti,V)_4Pt_3$ phases.

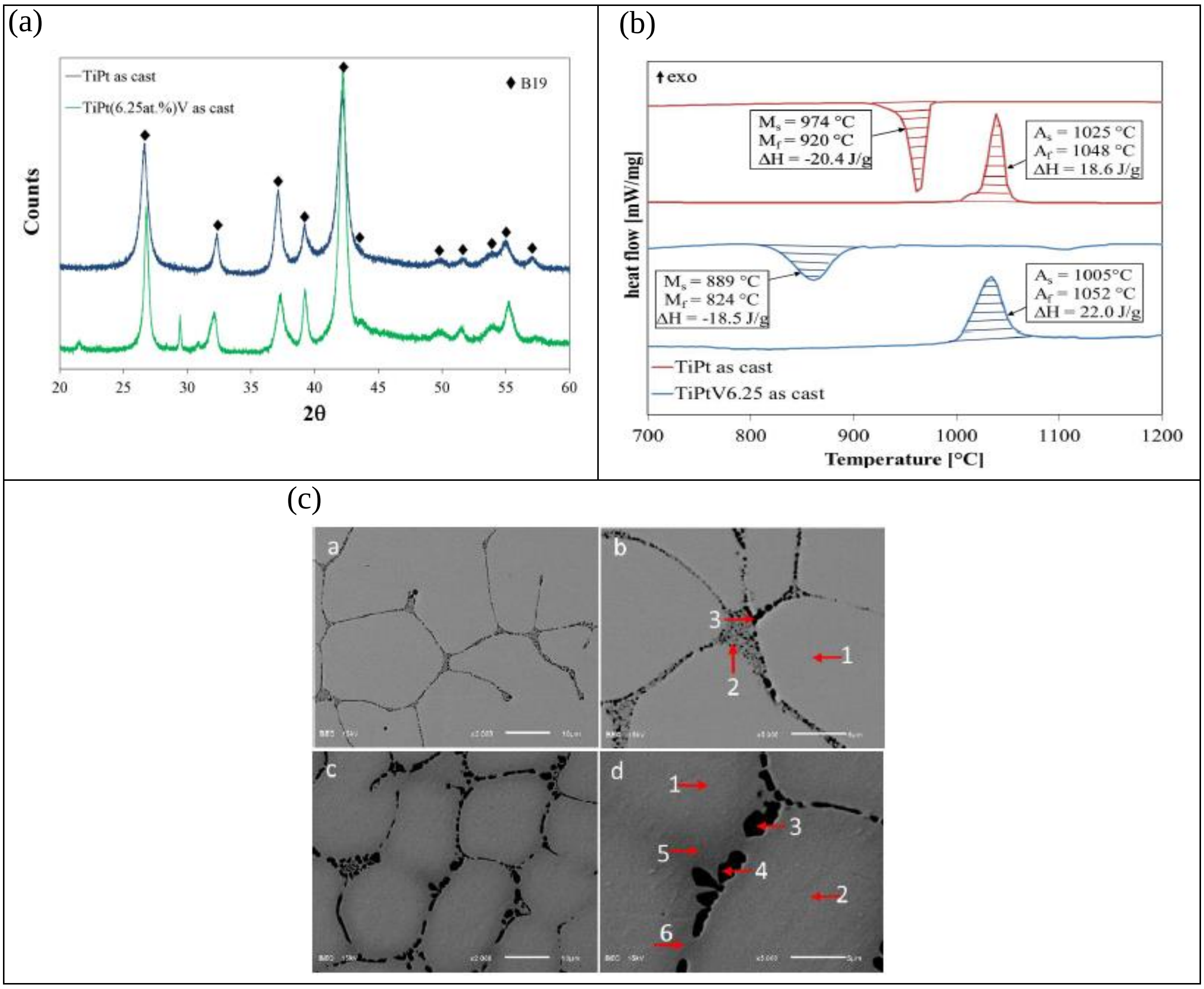

Figure 2.5.31: (i) X-ray diffraction analysis, (ii) DSC analysis and (iii) SEM micrographs of as-cast Ti-Pt-V alloy [21].

2.6. Production of Ti-Pt shape memory alloys

The Ti-Pt alloy is an equiatomic intermetallic compound comprised of high melting point components, where Ti has a melting point of 1668°C and Pt is 1768°C. Molten Ti is a universal solvent that dissolves atmospheric gases and reacts aggressively with other various materials [78]. The high reactivity of Ti could result in the shifting of compositions. Ideally, the initial composition should be kept constant throughout the whole experiment to avoid inhomogeneity on the samples. However, oxidation or melting loss of the prepared specimens could result in deviations from the nominal compositions which could affect the characteristics of the alloys [79]. In particular, the transformation temperatures are sensitive to composition.

Ti-Pt alloys can be synthesised using an arc melting, induction melting and a powder metallurgy routes. Powder metallurgy routes lead to the formation of metastable phases that transform to other phases at higher temperatures due to the non-equilibrium nature of the alloy. On the contrary, alloys produced by melting routes exhibit equilibrium phases and are less likely to transform to new ones when subjected to higher temperatures. However, the presence of alloying elements can lead to precipitation and evolution of phases at elevated temperatures. In this regard, research work on SMAs alloys synthesized by melting routes has been done [3–7].

Melting processes are associated with high rates of chemical segregation. However, studies have suggested that in order to reduce segregation, alloys could be quenched below their solidus temperatures [79]. Melting of elemental materials is usually carried out in a protective atmosphere of either Ar or He or vacuum to avoid contamination [79].

During arc melting, the upper electrode is a water cooled copper pole inlaid with tungsten head, which acts as a cathode [79]. The lower electrode, which is the anode, is the metal to be melted. An electric arc forms ion plasma under an inert gas shield or vacuum. The electric current passes through the electrode, thereby melting the anode metals while reaching several hundred amperes of current. The power supplied to the metal bath can be adjusted by monitoring the current intensity and the alloy is usually melted and remelted at least twice to ensure compositional homogeneity [79].

Non-equilibrium structures could be generated from solidification segregation as the melted alloy cools down through the liquidus, solidus and gradually solidifying. Solution heat treatment (SHT) could be a solution to the abovementioned problem, although some segregation (elemental) may be difficult to remove completely by this treatment. The SHT is usually carried out by putting samples into a furnace at a higher temperature below the solidus temperature of the alloy for an extended period, followed by quenching to room temperature. Quenching of samples is done to retain the phases at the SHT temperature to room temperature. Samples may also be slowly cooled to room temperature as this generates less thermal stress in the samples, thus making the lattice parameters measurements more accurate [79]. In this study, ternary SMAs were processed using arc melting routes, and SHTs were then carried out, followed by ice quenching.

2.7. Rationale of the current Project

Although the partial substitution of Pt with V decreased the martensitic transformation temperature of Ti-Pt, it was still above 750 ^{o}C. Therefore, Ti-Pt-V shape memory alloys can be used as candidates for potential high temperature applications. Therefore, the aim of the current study was to investigate the effect of partial substitution of either Pt or Ti with varying contents of V (6.25 and 12.5 at.%) on the shape memory properties in order to optimize the SME of these Ti-Pt alloys. Chapter 3 will describe the experimental procedure that was followed in the study. Chapters 4 and 5 will describe the effect of ternary alloying with V on the microstructure, crystal structure, transformation temperatures, mechanical properties and shape memory properties of Ti-Pt-V and Ti-V-Pt alloys in the as-cast and solution heat treated condition. Finally, an overall conclusion will be provided in Chapter 6.

CHAPTER 3: EXPERIMENTAL PROCEDURE

3. Experimental Procedure

Six alloys, namely Ti_{50}-Pt_{50}, Ti_{50}-$Pt_{43.75}$-$V_{6.25}$, Ti_{50}-$Pt_{37.5}$-$V_{12.5}$, Ti_{50}-$Pt_{31.75}$-$V_{18.25}$, $Ti_{43.75}$-$V_{6.25}$-Pt_{50} and $Ti_{37.5}$-$V_{12.5}$-Pt_{50} were produced using a button arc-melting furnace. Microstructure, chemical composition and crystal structure analysis of the alloys at various stages of processing were conducted using scanning electron microscopy (SEM) with an energy dispersive X-ray spectrometer (EDS) and X-ray diffraction (XRD). The thermal behaviour of the alloys was investigated using a differential scanning calorimetry (DSC). The compression and macro-Vickers hardness tests were used to study the mechanical properties and shape memory effect of the alloys. The preparation of the alloys and analytical techniques are further discussed below.

3.1. Powder preparation

Elemental powders of high purity Ti (99.9%), Pt (99.9%) and V (99.5%) were prepared in desired quantities to achieve homogeneous blends with compositions: Ti_{50}-Pt_{50}, Ti_{50}-$Pt_{43.75}$-$V_{6.25}$, Ti_{50}-$Pt_{37.5}$-$V_{12.5}$, Ti_{50}-$Pt_{31.75}$-$V_{18.25}$, $Ti_{43.75}$-$V_{6.25}$-Pt_{50} and $Ti_{37.50}$-$V_{12.5}$-Pt_{50}. Ti elemental powder was sourced from TLS, Technik, GmbH & Co, Germany. LGC Industrial Analytical (Pty) Ltd, South Africa, supplied the Pt and V elemental powders. The size of each prepared alloy blend was 28 g.

3.2. Compaction of powder blends

The powder blends were cold compacted at room temperature using an ENERPAC VLP 100 tonne press at 2842 MPa (100 bars) with a die size of 25 mm diameter to produce green compacts.

3.3. Melting of the alloys

The green compacts were arc melted using a button arc-melting furnace with a tungsten electrode in an argon atmosphere to produce button samples of Ti-Pt-V and Ti-V-Pt alloys, Figure 3.3.1(a). The buttons were remelted six times for all alloys in order to improve homogeneity. Prior to melting, green compacts placed in the Cu crucible were purged using argon gas in order to eliminate any contamination. A pure titanium (Ti) button located at the centre of the crucible was used as an oxygen getter in order to absorb all the oxygen/contaminants in the atmosphere, Figure 3.3.1(b). Melting was carried out using a transformer of 240 volts and the melting was controlled by supplying current to the electrode,

Figure 3.3.1(d). However, there was no temperature reading to note the temperature of the sample during melting. The mass of the green compacts before melting was approximately 27.8 g, and after melting, the alloy buttons weighed 26.9 g, giving a material loss of 3.2%.

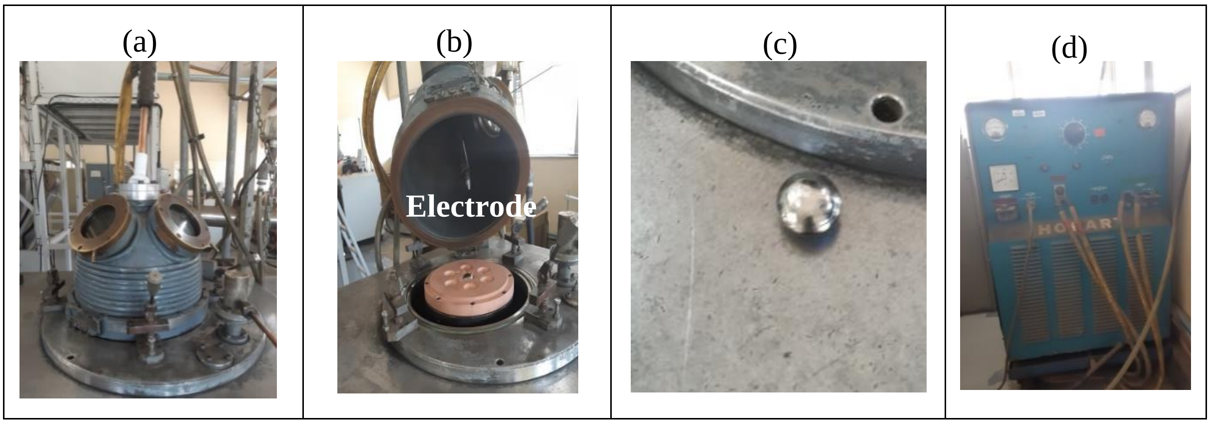

Figure 3.3.1: Photographs of the button arc-melting furnace showing (a) melting furnace, (b) electrode copper (Cu) crucible, oxygen getter, (c) example of the produced alloy button and (d) 240 volts Transformer.

After melting, alloy buttons were sectioned using a wire cutter for characterisation in the as-cast and solution heat treated condition. Solution heat treatments (SHTs) were carried out to improve homogeneity of the alloys. These heat treatments involved putting samples into a carbolite tube furnace under an argon inert gas environment. The samples were solution heat treated at a temperature of 1250 °C and holding for 72 hours, followed by ice water quenching.

The following sample preparation procedure was done on the as-cast and solution heat treated samples:

- Mounting of the samples was carried out on an Opal 440 mounting press machine using black bakelite.
- Grinding and polishing was done on a Saphir 550 automatic polishing machine using 1000, 2000 and 4000 grit paper, followed by colloidal silica as a final polishing paste and water in order to achieve a mirror surface.

3.3.1. X-ray diffraction analysis (XRD)

The XRD was used to determine the crystal structure of phases in the alloys. X-ray diffraction analysis was carried out in a PANanalytical X'Pert PRO operated at a voltage and current of 45 kV and 40 mA equipped with a PIXcel detector and a fixed divergence slit. The incident beam was produced from Cu K_α anode material (λ = 1.45 Å). Several alloy samples were analysed over the 2θ range of 5 to 90°, with a continuous scanning step size of 2θ = 0.026°, and a scan rate of 10 seconds/step. The resultant diffraction patterns were analysed for phase identification using the reference databases on X'Pert HighScore Plus software package. Lattice parameters were determined using the Rietveld method on the Maud software.

3.3.2. Differential scanning calorimetry (DSC)

The DSC was used to determine the thermal behaviour of the alloys in both as-cast and solution heat treated conditions. A DSC is a thermo-analytical technique that measures the heat flow produced in a sample when it is heated or cooled. Thermal behaviour includes transformation temperatures, hysteresis and latent heats of transformation. The analysis was carried out using a Netzsch STA 449F3 Jupiter simultaneous thermal analyser (STA) instrument with a type-S thermocouple and a Rd-wound tube furnace with a maximum allowable heating rate of 50 ^{o}C/min. The DSC sample holder was made of Pt to allow for operation at high temperatures. Al_2O_3 pans with lids were used as crucibles; an empty crucible was used as a reference. DSC measurements were conducted at a ramp rate of 20 ^{o}C/min under a flow of Ar gas in the temperature range of 25–1500 ^{o}C. Samples were subjected to two temperature cycles; only results from the second cycle were reported. Data acquisition and analysis were carried out using the manufacturer supplied Proteus analysis software.

3.3.3. Scanning electron microscopy (SEM)

The SEM in backscattered mode with EDX was used to determine the homogeneity achieved, chemical composition, phase identification and microstructure of the Ti-Pt-V and Ti-V-Pt alloys in both as-cast and solution heat treated conditions. A JEOL JSM-6510 instrument with a tungsten electron gun was used. The accelerating voltage was varied between 5 and 15 kV depending on the imaging mode and energy dispersive X-ray spectroscopy (EDS) for elemental compositional analysis was used. The mounted sample was placed in a specimen mount where phase identification and chemical homogeneity was carried out in backscattered electron (BSE) imaging mode and EDS consisting of a Si (Li) detector.

3.3.4. Compression testing

An Instron^{TM} 1342 Servo-hydraulic machine having a load cell of 25 kN was used to perform room temperature compression tests, Figure 3.3.2(a). During testing, 3x3x6 mm Ti-Pt-V and Ti-V-Pt samples in both as-cast and solution heat treated conditions were compressed on a tungsten carbide platen using a compression cross head speed of 0.5mm/min at room temperature with no lubricant, Figure 3.3.2(b) and (c). Three samples were tested for each alloy and condition. The Instron Bluehill software automatically determined the results after testing. The compressive test was stopped either after failure of the sample or when the maximum load capacity (25 kN) of the test machine was reached. All tests were done according to the ASTM E9 standard.

Figure 3.3.2: (a) Instron 1342 servo-hydraulic machine used for room temperature compression tests, (b) an example of the samples and (c) the set-up of the machine during testing.

3.3.5. Hardness testing

Hardness tests were performed using a macro Vickers Hardness tester FV-700 under a load of 2 kg, with a dwelling time of 10 seconds. The mounted specimen was placed on the hardness tester and indented in order to give the Vickers hardness value of each alloy. Vickers hardness (VHN) was determined from the average of at least five readings per sample on Ti-Pt, Ti-Pt-V and Ti-V-Pt alloys in both as-cast and solution heat treated conditions.

CHAPTER 4: RESULTS

4. Results

In this chapter, the results of the effect of ternary alloying with V on the shape memory properties of Ti-Pt alloys in both the as-cast and solution heat treated samples are presented. Titanium and V are susceptible to oxidation and it is possible that there was continued oxygen pickup during processing of the alloys, which led to the formation of oxygen-stabilised phases on the Ti-Pt-V and Ti-V-Pt alloys. The β-TiPt phase, which is stable at higher temperatures (above 1000 ^{o}C) was not observed in this study. Therefore, all mention of the TiPt phase refers to the B19 orthorhombic α-TiPt phase formed after a displacive transformation from the B2 cubic β-TiPt phase.

The results are divided into two sections, (1) Vanadium additions of 6.25, 12.5 and 18.25 at.% replacing Pt and (2) Vanadium additions of 6.25 and 12.5 at.% replacing Ti. The microstructural evolution was studied using SEM backscattered electron microscopy with an EDS to determine the compositions of the phases in each alloy. Phase and crystal structure identification were confirmed using an XRD. The thermal behaviour, which includes transformation temperatures, hysteresis and latent heat of transformation were investigated using the DSC with a simultaneous thermal analyser (STA) technique. Mechanical properties were measured to determine the amount of compressive stresses and strains that each alloy could sustain before failing using room temperature compression tests. The shape memory effect was studied by deforming Ti-Pt-V and Ti-V-Pt samples using compression tests, followed by heating the alloy above the A_f temperature and measuring the recovery strain.

The following sub-sections are covered under each section:

- The effect of ternary alloying with V replacing either Pt or Ti on the microstructural evolution of Ti-Pt alloy in both the as-cast and solution heat treated conditions.
- The effect of ternary alloying with V on the crystal structure of Ti-Pt alloy using the XRD technique.
- The effect of ternary alloying on the phase transformation, such as the change in transformation temperatures, hysteresis and latent heat of transformation with additions of V on Ti-Pt alloys.
- The effect of V addition on mechanical properties of Ti-Pt alloy.
- The effect of V addition on shape memory properties of Ti-Pt alloy.

4.1. The effect of ternary alloying with V replacing Pt on the functional properties of Ti-Pt alloys

This section reports on the microstructural analysis, phase identification, crystal structure, phase transformation, mechanical properties and shape memory effect of Ti-Pt-V when replacing V for Pt in both the as-cast and solution heat treated conditions. The V content was varied from 0-18.25 at.%.

4.1.1. The effect of V ternary alloying on the evolution of microstructures

Figures 4.1.1 to 4.1.4 show SEM backscattered electron images (BEI) and EDX results of Ti_{50}-Pt_{50}, Ti_{50}-$Pt_{43.75}$-$V_{6.25}$, Ti_{50}-$Pt_{37.5}$-$V_{12.5}$ and Ti_{50}-$Pt_{31.75}$-$V_{18.25}$ in both as-cast and solution heat treated conditions. Both as-cast and solution heat treated microstructures had multiple phases. The chemical compositions shown for all phases are the average values taken from three different areas of the sample. The overall compositions (Tables 4-1 to 4-4) were slightly different from the initial intended compositions, but the difference was within the error margin of EDX measurements.

4.1.1.1. Binary Ti_{50}-Pt_{50} alloy

The microstructure of the Ti_{50}-Pt_{50} alloy in the as-cast and solution heat treated conditions including SEM-EDS results are presented in Figure 4.1.1. In the as-cast condition, the microstructure consisted of TiPt dendrites and Ti_3Pt in the interdendritic regions, Figure 4.1.1(a) and (b). The EDX revealed that the overall composition was Ti-rich (51.6±0.5 at. % Ti) after arc melting, Table 4-1.

After SHT at 1250 ^{o}C, the overall composition remained unchanged (51.7±1.1 at. % Ti). The matrix was comprised of the TiPt phase with small quantities of Ti_3Pt and Ti_5Pt_3 phases, Figure 4.1.1(c) and (d).

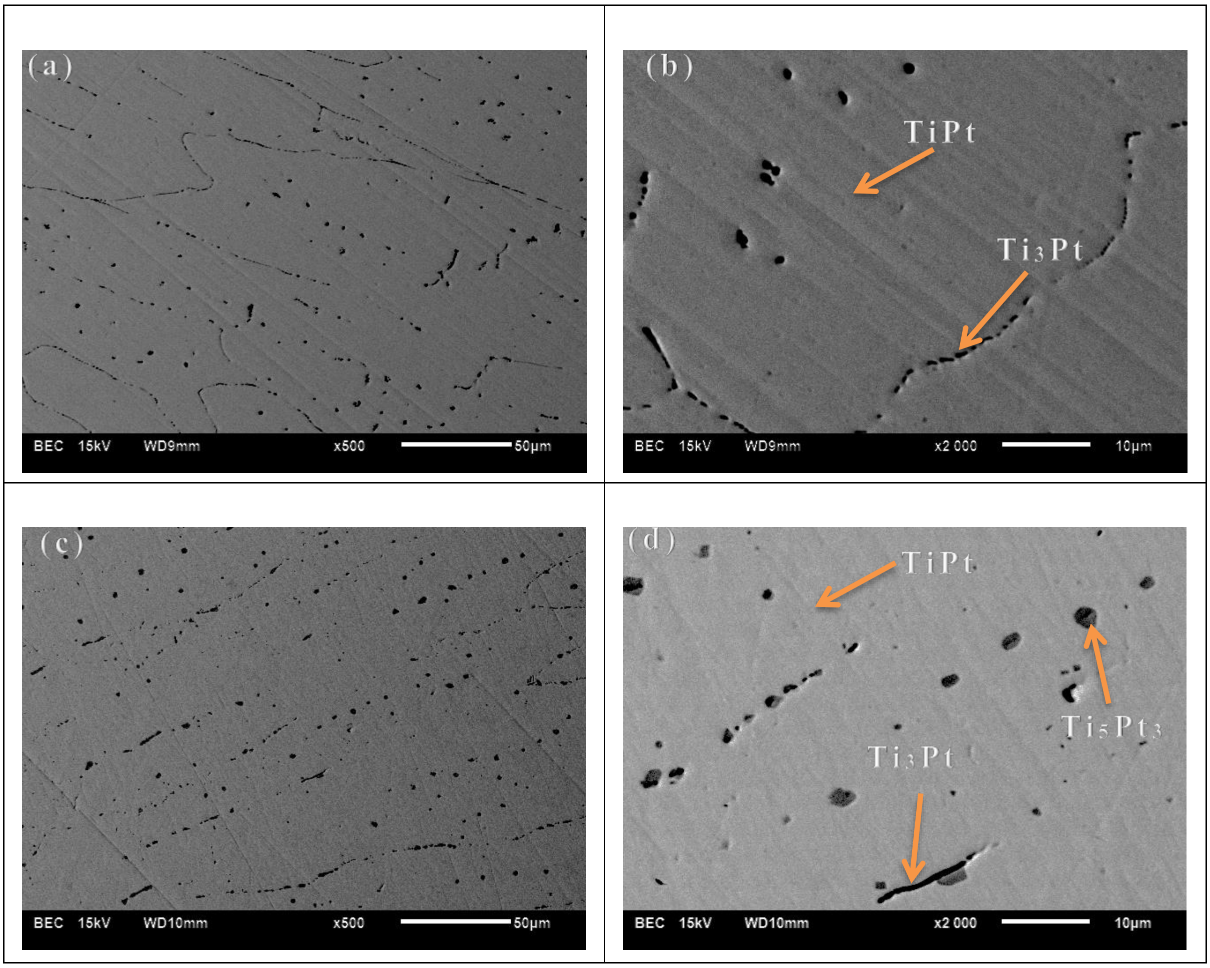

Figure 4.1.1: Low and high magnification SEM backscattered electron images (BEI) of Ti_{50}-Pt_{50} in the as cast condition (a-b) and solution heat treated at 1250 °C for 72 h followed by ice water quenching (c-d).

Table 4-1: SEM-EDX results of Ti_{50}-Pt_{50} in the as-cast and solution heat treated conditions.

	Ti	Pt
	As-cast (at.%)	
Overall	51.6±0.5	48.4±0.3
TiPt	51.2±1.2	48.8±0.7
Ti_3Pt	76.8±1.4	23.2±0.4
	Solution heat treated (at.%)	
Overall	51.7±1.1	48.3±0.5
TiPt	50.9±1.9	49.1±1.7
Ti_3Pt	75.5±2.3	24.5±0.8
Ti_5Pt_3	65.9±2.6	34.1±1.4

4.1.1.2. Ti_{50}-$Pt_{43.75}$-$V_{6.25}$ alloy

Figure 4.1.2(a) and (b) shows that the as-cast microstructure of Ti_{50}-$Pt_{43.75}$-$V_{6.25}$ alloy consisted of Ti(Pt,V) dendrites and interdendritic regions comprised $(Ti,V)_3Pt$ and $Ti_5(Pt,V)_3$. The microstructures and EDX overall composition revealed that the partial substitution of Pt with V resulted in interdendritic regions comprised of a large amount of Ti-rich phases. The transforming Ti(Pt,V) phase contained 4.5±0.7 at.% V, Table 4-2.

Backscattered electron images (BEI) of the solution heat treated structure revealed a matrix of the Ti(Pt,V) with large quantities of $Ti_4(Pt,V)_3$ and small quantities of $Pt(V,Ti)_3$ phases, Figure 4.1.2 (c) and (d). The EDX overall composition and amount of transforming Ti(Pt,V) phase remained unchanged after the SHT, Table 4-2.

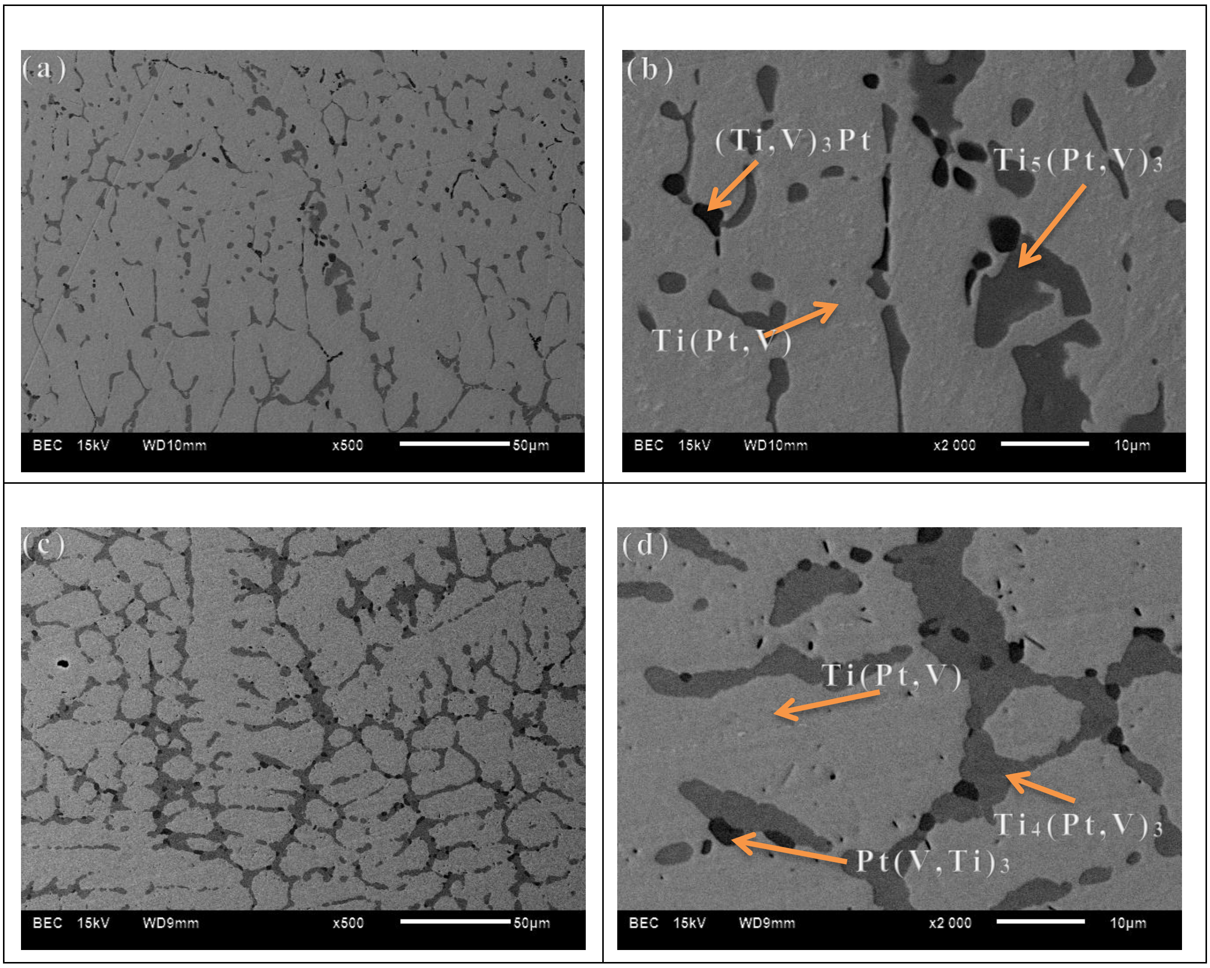

Figure 4.1.2: Low and high magnification SEM backscattered electron images (BEI) of Ti_{50}-$Pt_{43.75}$-$V_{6.25}$ in the as-cast condition (a-b) and solution heat treated at 1250 °C for 72 h followed by ice water quenching (c-d).

Table 4-2: SEM-EDX results of Ti_{50}-$Pt_{43.75}$-$V_{6.25}$ in the as-cast and solution heat treated conditions.

	Ti	V	Pt
As-cast (at.%)			
Overall	51.8±0.4	6.2±0.3	42.0±0.2
Ti(Pt,V)	51.5±0.9	4.5±0.7	44.0±0.3
$(Ti,V)_3Pt$	67.9±0.9	6.5±0.5	25.6±0.3
$Ti_5(Pt,V)_3$	63.9±0.8	3.9±0.3	32.2±0.3
Solution heat-treated (at.%)			
Overall	51.5±0.3	6.0±0.2	42.5±0.5
Ti(Pt,V)	51±0.7	4.6±0.3	44.4±0.3
$Ti_4(Pt,V)_3$	55.9±0.7	7.8±0.3	36.3±0.3
$Pt(V,Ti)_3$	36.9±0.6	36.1±0.6	27.0±0.2

4.1.1.3. Ti_{50}-$Pt_{37.5}$-$V_{12.5}$ alloy

The as-cast microstructure after ternary alloying with 12.5 at.% V when substituting Pt enlarged the eutectic regions while the volume fraction of Ti(Pt,V) dendrites decreased, Figure 4.1.3(a) and (b). The eutectic regions comprised $Pt(V,Ti)_3$, $Ti_4(Pt,V)_3$ and $Ti_3(Pt,V)$ phases, Figure 4.1.3(a) and (b). The EDX results from the SEM revealed that the transforming Ti(Pt,V) phase contained 7.9±0.3 at.% V in the as-cast condition, Table 4-3.

Solution heating the as-cast microstructure resulted in the elimination of the eutectic regions with an increased volume fraction of other phases and a decreased amount of the transforming Ti(Pt,V) phase. The microstructure of the Ti_{50}-$Pt_{37.5}$-$V_{12.5}$ comprised α-Ti(Pt,V) matrix with multiple phases of $Ti_4(Pt,V)_3$, $Pt(V,Ti)_3$ and Ti_3Pt phases, Figure 4.1.3(c) and (d). As observed, the volume fraction of $Pt(V,Ti)_3$ was more in the Ti_{50}-$Pt_{37.5}$-$V_{12.5}$ than in the Ti_{50}-$Pt_{43.75}$-$V_{6.25}$ alloy, indicating that with increasing V content, its volume fraction was increasing.

The EDX overall composition did not change much between the as-cast and solution heat treated conditions, Table 4-3. The amount of V in the Ti(Pt,V) phase was 4.5±0.5 at.% after SHT.

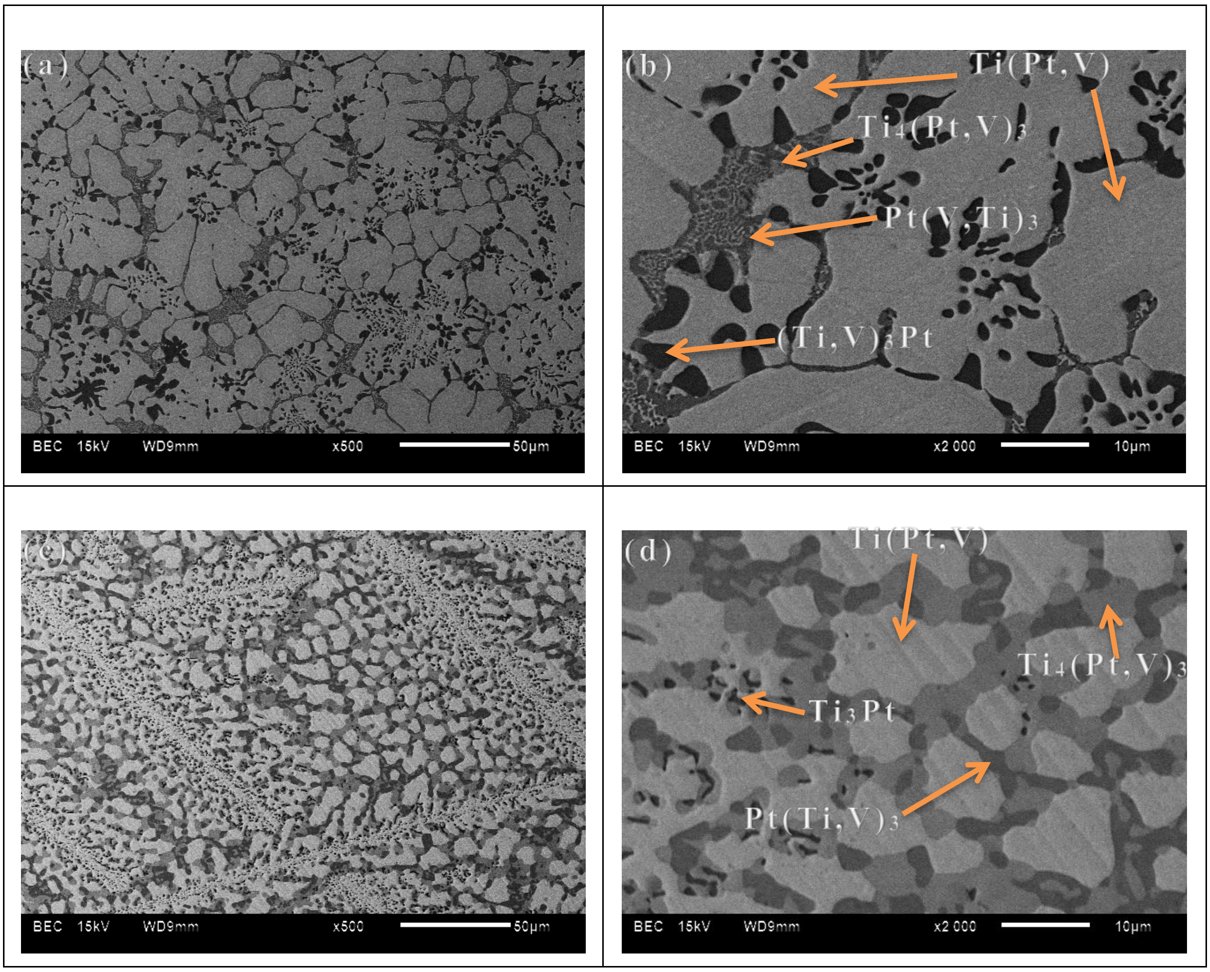

Figure 4.1.3: Low and high magnification SEM backscattered electron images (BEI) of Ti_{50}-$Pt_{37.5}$-$V_{12.5}$ in the as-cast condition (a-b) and solution heat treated at 1250 °C for 72h followed by ice water quenching (c-d).

Table 4-3: SEM-EDX results of Ti_{50}-$Pt_{37.5}$-$V_{12.5}$ in the as-cast and solution heat treated conditions.

	Ti	V	Pt
	As-cast (at.%)		
Overall	50.4±0.3	11.3±0.2	38.3±0.1
Ti(Pt,V)	48.5±0.6	7.9±0.3	43.6±0.3
$Ti_4(Pt,V)_3$	57.1±1.8	10.2±1.5	32.7±0.6
$Pt(V,Ti)_3$	38.4±0.6	34±0.6	27.6±0.2
$(Ti,V)_3Pt$	66.6±0.7	9.2±0.3	24.2±0.4
	Solution heat treated (at.%)		
Overall	49.8±0.3	11.8±0.3	38.4±0.1
Ti(Pt,V)	50.4±1.1	4.5±0.5	45.1±0.4
$Ti_4(Pt,V)_3$	56.1±1.0	7.6±0.5	36.3±0.4
$Pt(V,Ti)_3$	35.2±0.7	37.8±0.7	27±0.3
Ti_3Pt	73±0.9	-	27±0.3

4.1.1.4. Ti_{50}-$Pt_{31.75}$-$V_{18.25}$ alloy

Backscattered electron images (BEIs) of the as-cast Ti_{50}-$Pt_{31.75}$-$V_{18.25}$ alloy revealed that more additions of V (18.25 at.%) resulted in a complex microstructure. The microstructure comprised $Pt(V,Ti)_3$ and $Ti_2(Pt,V)O$ dendrites interspersed with low volume fractions of the Ti(Pt,V) and $Ti_4(Pt,V)_3$ phases in the interdendritic regions, Figure 4.1.4(a) and (b). The EDX results from the SEM revealed that the Ti(Pt,V) phase formed contained only 8.2±0.8 at.% V which is far off from the intended composition of 18.25 at.% V, indicating that higher V contents were not going into solution with Pt, Table 4-4.

The microstructures of the the Ti_{50}-($Pt_{31.75}$-$V_{18.25}$) alloy after SHT had a matrix of $Pt(V,Ti)_3$, $(TiO)_3Pt$, Ti(Pt,V) and $Ti_4(Pt,V)_3$ phases, Figure 4.1.4(c) and (d). The amount of the transforming Ti(Pt,V) phase had significantly decreased. The EDX results from the SEM revealed that the transforming Ti(Pt,V) phase contained 14.9±4.1 at.% V which is far off from the as cast condition (8.2±0.8 at.%), Table 4-4. The latter could be attributed to small amounts of Ti(Pt,V) phase that were difficult to detect on the SEM-EDS. Since the transforming phase of interest which is Ti(Pt,V) was in very small quantities, this alloy will not be reported further in the rest of the study.

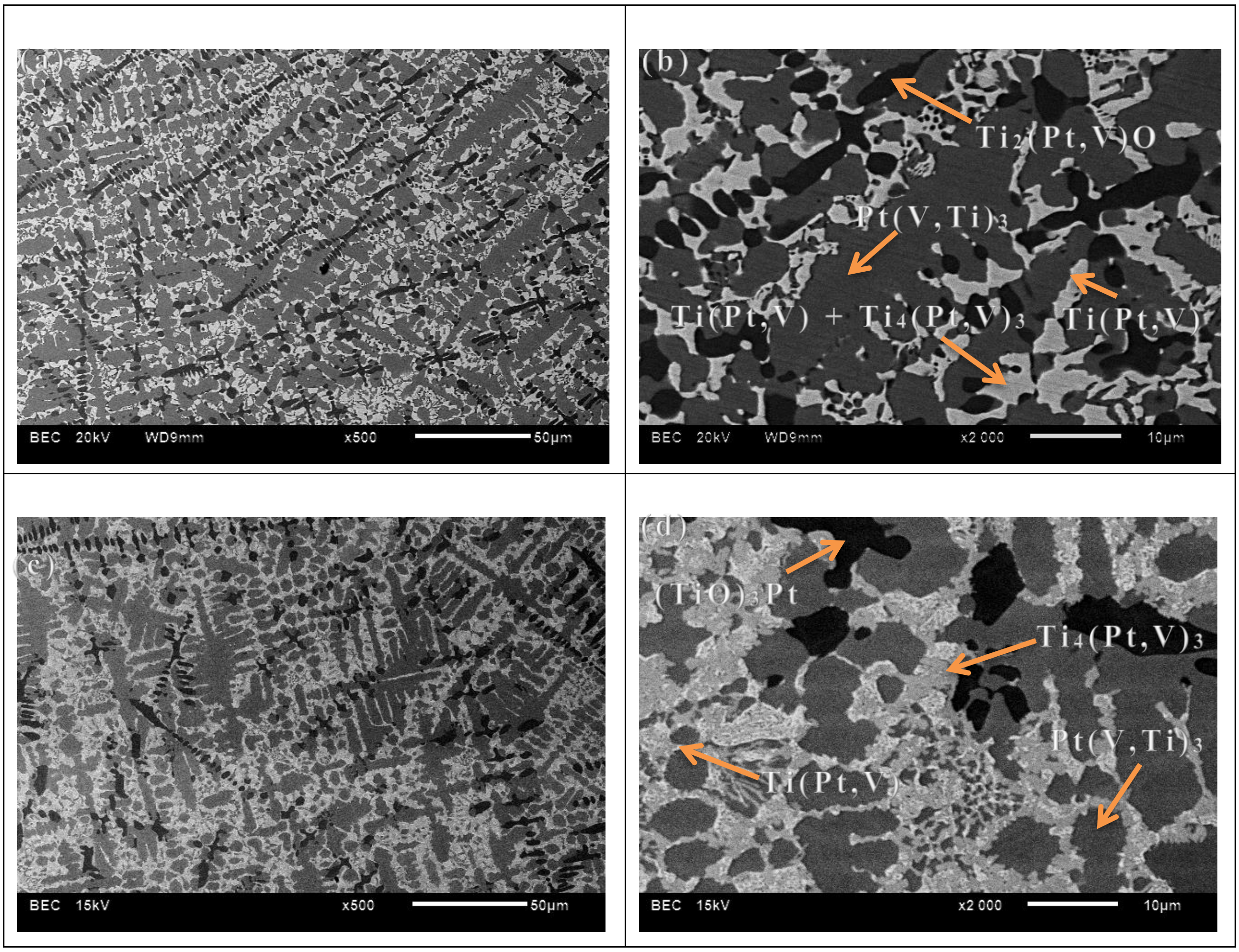

Figure 4.1.4: Low and high magnification SEM backscattered electron images (BEI) of Ti_{50}-$Pt_{31.75}$-$V_{18.25}$ in the as-cast condition (a-b), solution heat treated at 1250 °C for 72h followed by ice water quenching (c-d).

Table 4-4: SEM-EDX results of Ti_{50}-$Pt_{31.75}$-$V_{18.25}$ in the as-cast and solution heat treated conditions.

	O	Ti	V	Pt
		As-cast (at.%)		
Overall	-	50.2 ±0.3	18.9±0.2	30.9±0.5
Ti(Pt, V)	-	51.4±1.1	8.20±0.8	40.4±1.9
$Ti_4(Pt,V)_3$	-	59.3±1.1	12.1±0.5	28.6±2.1
$Pt(V,Ti)_3$	-	41.4±0.7	31.1±0.7	27.5±2.0
$Ti_2(Pt,V)O$	32.4±2	44.8±0.8	6.10±0.4	16.7±1.3
		Solution heat treated (at.%)		
Overall	-	50.9±0.7	19.7±0.6	29.4±0.3
Ti(Pt, V)	-	52.6±2.9	14.9±4.1	32.5±1.3
$Ti_4(Pt,V)_3$	-	57.7±1.9	9.2±1.3	33.1±0.8
$Pt(V,Ti)_3$	-	42.9±1.4	31.0±1.9	26.1±0.8
$(Ti,O)_3Pt$	43.9±2.8	42.5±1.0	-	13.6±0.4

4.1.2. The effect of ternary alloying with V on the crystal structure of Ti-Pt alloys

X-ray diffraction (XRD) analysis was conducted for the identification of phases on Ti-Pt-V alloys at room temperature. Figure 4.1.5 shows the XRD results of the Ti-Pt alloy with V additions (0, 6.25 and 12.5 at.%) replacing Pt in the as-cast and solution heat treated conditions. SEM micrographs revealed that the Ti_{50}-$Pt_{31.75}$-$V_{18.25}$ alloy had very small amounts of the phase of interest, which is the Ti(Pt,V); therefore its XRD patterns are not displayed. The binary Ti_{50}-Pt_{50} XRD results are included for comparison.

The diffraction patterns of the B19 Ti(Pt,V) martensite structure were clearly identified in the as-cast and solution heat treated conditions for all alloys, indicating that an austenite to martensite transformation occurred after ternary alloying with V. The lattice parameters of the B19 martensite structure were estimated by the Rietveld method using Maud software and are summarized in Table 4-5. The addition of V to Ti-Pt did not change the angle of the B19 orthorhombic structure from 90^o.

In the as-cast condition, the addition of V to Ti-Pt shifted the B19 diffraction peaks to slightly higher 2θ angles. This corresponds to a reduction of the unit cell along the a and c axis. The diffraction peaks of the B19 martensite phase observed in the as-cast condition had shifted to lower 2θ angles after SHT for the Ti_{50}-Pt_{50}, Ti_{50}-$Pt_{43.75}$-$V_{6.25}$ and Ti_{50}-$Pt_{37.5}$-$V_{12.5}$ alloys, indicating an increase in the lattice parameters of the unit cell. However, a decrease in lattice parameters with increasing V content was maintained after SHT.

Several other phases were formed and identified as the Ti_3Pt and $Pt(V,Ti)_3$ phases. The difference between the two phases is that the latter had very high amounts of V in the ranges of 36.1±0.6 at.% V in the Ti_{50}-$Pt_{43.75}$-$V_{6.25}$ alloy which increased to 37.8±0.7 at.% V in the Ti_{50}-$Pt_{37.5}$-$V_{12.5}$ alloy. The Ti_3Pt phase was not detected in the binary Ti-Pt compositions by XRD due to the small amounts of the phase at approximately less than 3% which is the detection limit of XRD. The remaining diffraction peaks were estimated to be $Ti_4(Pt,V)_3$ (red dotted line on XRD pattern) and Ti_5Pt_3 (black dotted line on XRD pattern) phases. These phases could not be accurately identified by XRD because their prototypes and crystal structure have not been confirmed by XRD to date. In addition, these difraction peaks were more prominent after SHT, indicating an increased amount of these phases.

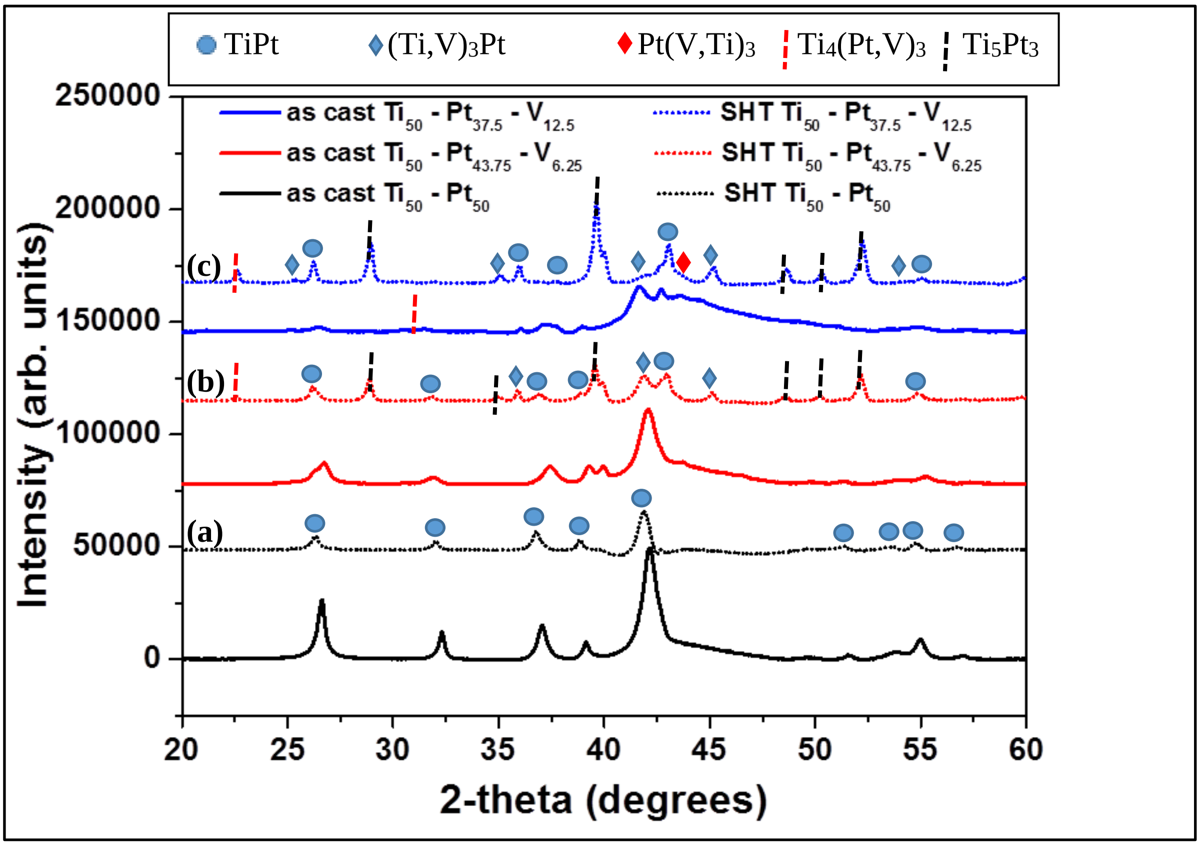

Figure 4.1.5: XRD results of (a) Ti_{50}-Pt_{50}, (c-d) Ti_{50}-$Pt_{43.75}$-$V_{6.25}$ and (b) Ti_{50}-$Pt_{37.5}$-$V_{12.5}$ in the as-cast (c) and solution heat treated conditions, solid and dashed lines respectively.

Table 4-5: Lattice parameters of the B19 TiPt phase in the as-cast and solution heat treated conditions of Ti-Pt alloyed with V when replacing Pt.

Lattice parameter (Å)	As-cast	Solution heat treated
	Ti_{50} – Pt_{50} : B19 TiPt	
a	4.60±0.090	4.64±0.001
b	2.77±0.072	2.79±0.145
c	4.86±0.111	4.93±0.001
	Ti_{50} – $Pt_{43.75}$ – $V_{6.25}$: B19 Ti(Pt,V)	
a	4.58±0.001	4.56±0.006
b	2.78±0.001	2.77±0.005
c	4.86±0.003	4.88±0.010
	Ti_{50} – $Pt_{37.5}$ –$V_{12.5}$: B19 Ti(Pt,V)	
a	4.55±0.002	4.56±0.053
b	2.77±0.002	2.81±0.003
c	4.84±0.004	4.90±0.006

In Figure 4.1.6, the lattice parameter ratios a/b, c/b and c/a were plotted as a function of V concentrations. The lattice pararmeter ratios of all the alloys were greater than 1.0 with a/b and c/b greater than 1.4, indicating that the addition of V to Ti-Pt alloys did not change the orthorhombic structure of TiPt.

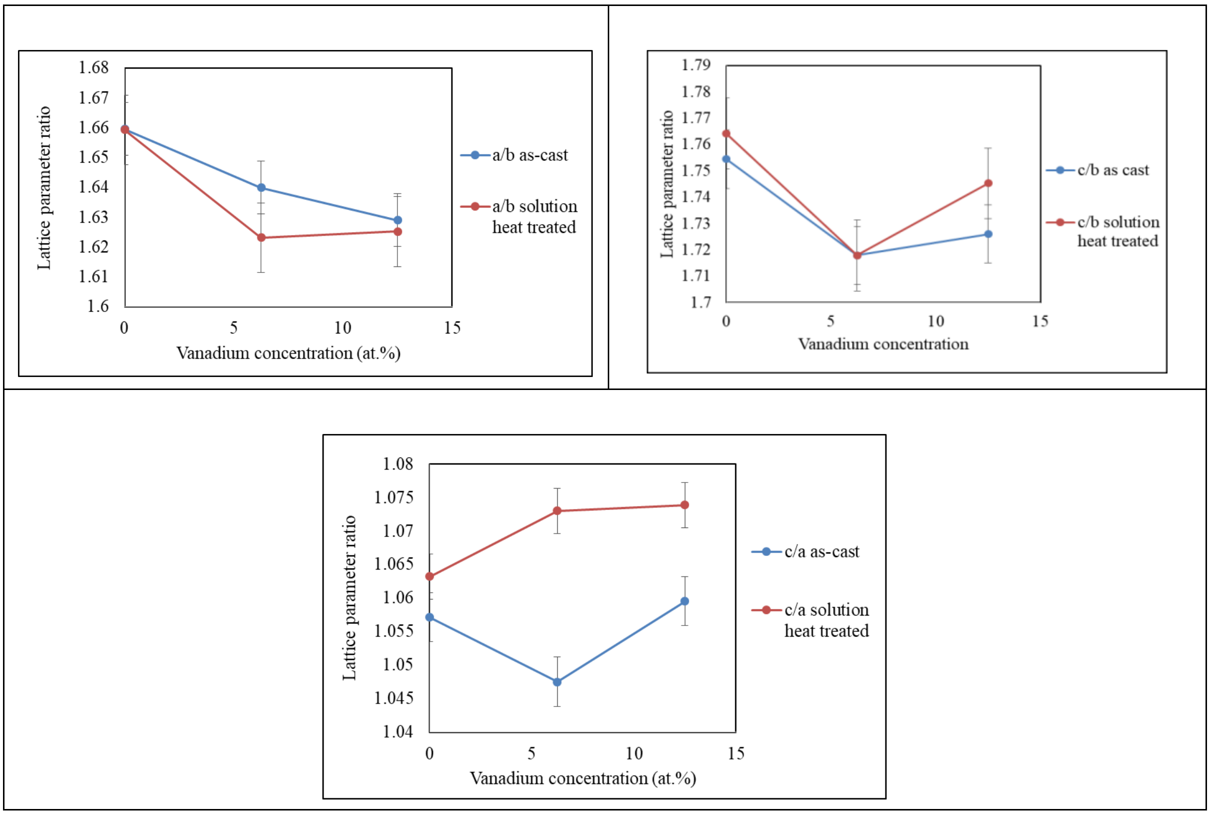

Figure 4.1.6: Change in lattice parameter ratio of the B19 phase as a function of V concentration, (a) a/b, (b) c/b and (c) c/a.

4.1.3. The effect of ternary alloying with V on the phase transformation of Ti-Pt alloys

The DSC was performed on the as-cast and solution heat treated Ti-Pt-V alloys. The DSC results measured the transformation temperature of the resulting composition of the TiPt phase after arc melting and SHT. In this study, the SEM-EDX results of Ti-Pt-V alloys in the as-cast and solution heat treated conditions revealed that the exact compositions of the transforming TiPt phase were slightly different from the intended nominal compositions as follows: The Ti_{50}-Pt_{50} sample formed $Ti_{51.2}Pt_{48.8}$ (at.%) and $Ti_{50.9}Pt_{49.1}$, the Ti_{50}-$Pt_{43.75}$-$V_{6.25}$ sample formed $Ti_{51.5}(Pt_{44},V_{4.5})$ and $Ti_{51}(Pt_{44.4},V_{4.6})$, the Ti_{50}-$Pt_{37.5}$-$V_{12.5}$ sample formed $Ti_{48.5}(Pt_{43.6},V_{7.9})$ and $Ti_{50.4}(Pt_{45.1},V_{4.5})$ and the Ti_{50}-$Pt_{31.75}$-$V_{18.25}$ formed $Ti_{51.4}(Pt_{40.4},V_{8.2})$ and $Ti_{49.7}(Pt_{28.2},V_{22.1})$. The samples were heated and cooled twice from room temperature and only results for the second heating /cooling cycles are reported. Based on the microstructure results, the Ti_{50}-$Pt_{31.75}$-$V_{18.25}$

sample had very small amounts of the transforming TiPt phase, thus, its DSC result was not reported.

4.1.3.1. Phase transformation in Ti_{50}-Pt_{50} alloy sample

Figure 4.1.7 shows two heating and cooling DSC cycles of the binary Ti_{50}-Pt_{50} sample in the as-cast and solution heat treated conditions. In the as-cast condition (solid line): the first heating curve (bottom) showed a single step transformation labelled M→A with austenite start and finish temperatures of A_s = 1035.2 °C and A_f = 1078.0 °C. During cooling, the forward transformation proceeded via a multi-stage transformation sequence. The first peak labelled $A \rightarrow M_1$ with the martensite start and finish temperatures of M_s = 1018.5 °C and M_f = 990.6 °C was the transformation of austenite to martensite phase. On further cooling, the remaining austenite transformed into a martensite ($A \rightarrow M_2$) structure characterised by a small latent heat with a peak and finish temperature of M_{2p} = 980.7 °C and M_{2f} = 969.7 °C. During the second heating cycle, the reverse transformation proceeded through two transformation steps. The first peak was a reverse transformation of the M_2 structure into the austenite, $M_2 \rightarrow A$, followed by a reverse transformation of the first type of martensite in the reaction $M_1 \rightarrow A$. Table 4-6 shows that the characteristic temperatures of the second heating cycle $M_1 \rightarrow A$ transformations were closer to those of the first heating cycle M → A transformation, thus indicating that they belong to the same reversible transformation of the B2 to B19 TiPt martensite phase with similar martensite types of M and M_1. The alloy did not show a significant change in the transformation temperatures after SHT, except a slight decrease in the transformation temperatures and latent heat of formation, Table 4-6.

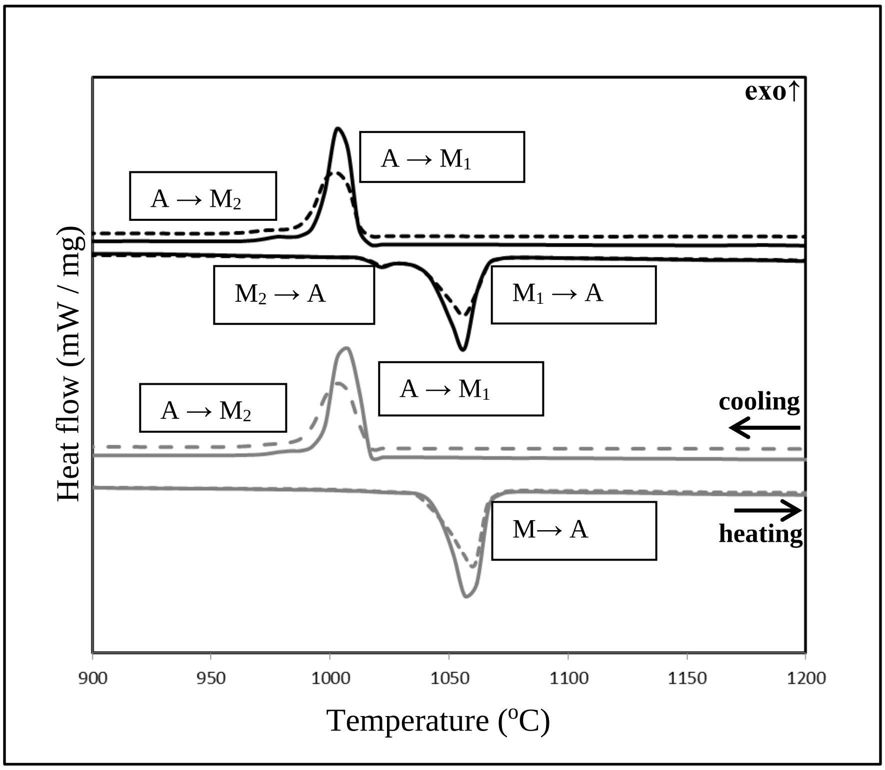

Figure 4.1.7: First (bottom) and second (top) heating and cooling DSC cycles of $Ti_{51.2}Pt_{48.8}$ phase in the as-cast condition and $Ti_{50.9}Pt_{49.1}$ phase in the solution heat treated condition (dotted line) Ti-Pt alloy, solid and dashed lines respectively.

The thermal hysteresis for the first and second transformation cycles were calculated using the formula [47]: $\Delta T = A_f - M_s$ was 60 and 61°C in the as-cast condition and 58 and 60°C in the solution heat treated condition, Table 4-6.

The latent heat of transformation is the heat/energy involved to generate a phase and was calculated from the area under the heating and cooling peak cycles The latent heats of formation of $Ti_{51.2}Pt_{48.8}$ and $Ti_{50.9}Pt_{49.1}$ for the forward and reverse transformations were similar to what has been previously observed in Ti-Pt alloys [65]. The latent heats of the M_2 structure for the forward and reverse transformations was 0.11 J/g for the first cycle during cooling, 0.25 and -0.11 J/g for the second cycle. The latter were lower than previously observed in Ti-Pt alloys [65], indicating that the amount of this structure on the current alloy sample was low.

Table 4-6: Transformation temperatures, transformation hysteresis and transformation enthalpy during heating and cooling for the first and second DSC thermal cycles of the $Ti_{51.2}Pt_{48.8}$ and $Ti_{50.9}Pt_{49.1}$ phases in the as-cast and solution heat treated conditions.

Cycle	Phase	A_s (°C)	A_f (°C)	M_{1s} (°C)	M_{1f} (°C)	M_{2p} (°C)	M_{2f} (°C)	ΔT (°C)	ΔH (J/g) forward/reverse	
As-cast										
1st	$Ti_{51.2}Pt_{48.8}$	1035	1078	1018	991	981	970	60	26.4	-26.8
2nd		1031	1076	1015	986	978	971	61	26.0	-23.5
Solution heat treated										
1st	$Ti_{50.9}Pt_{49.1}$	1032	1075	1017	984	975	965	58	19.2	-20.7
2nd		1031	1074	1014	981	973	965	60	18.6	-16.9

4.1.3.2. Phase transformations in Ti_{50}-Pt_{50}, Ti_{50}-($Pt_{43.75}$-$V_{6.25}$) and Ti_{50}-($Pt_{37.5}$-$V_{12.5}$) alloy samples

During DSC analysis, there was no significant variation between the first and second heating and cooling cycles of Ti-Pt-V alloy samples in both the as-cast and solution heat treated conditions. Therefore, only the second cycle heating and cooling curves were reported. Figure 4.1.8 presents DSC second cycle curves for Ti_{50}-$Pt_{43.75}$-$V_{6.25}$ and Ti_{50}-$Pt_{37.5}$-$V_{12.5}$ alloy samples in the as-cast and solution heat treated conditions. The binary Ti-Pt second cycle curves was replotted for comparison. The addition of V when replacing Pt, changed the transformation from multiple to single step transformation and resulted in a decrease of the transformation temperatures. For example, the M_s temperature decreased from 1015 °C (binary) to 891 °C for $Ti_{51.5}(Pt_{44},V_{4.5})$ and 875 °C for $Ti_{48.5}(Pt_{43.6},V_{7.9})$ in the as-cast condition, Figure 4.1.8 and Table 4-7. After SHT, the transformation temperatures of the forward reaction had slightly decreased with increasing V contents, Figure 4.1.9(a) and Table 4-7.

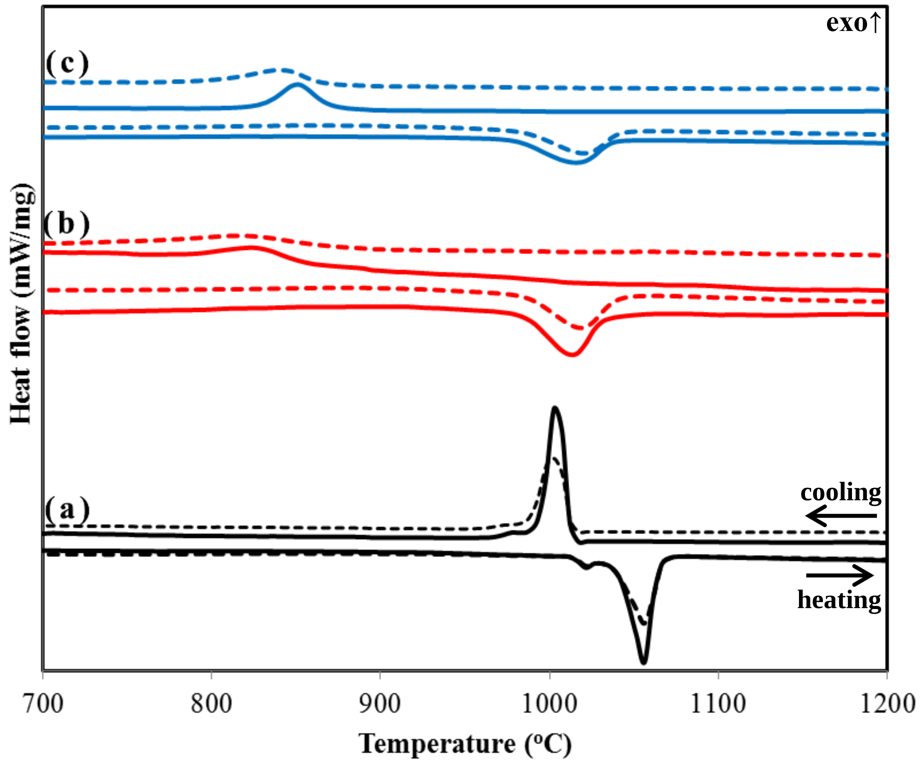

Figure 4.1.8: Second cycling DSC curves of the (a) $Ti_{50}Pt_{50}$, (b) Ti_{50}-$Pt_{43.75}$-$V_{6.25}$ and (c) Ti_{50}-$Pt_{37.5}$-$V_{12.5}$ (at.%) alloy samples in the as-cast and solution heat treated conditions, solid and dashed lines respectively.

The addition of V widened the thermal hysteresis of TiPt with increasing V content, from 61 °C for $Ti_{51.2}Pt_{48.8}$ to 165.8 °C for $Ti_{51}(Pt_{44.4},V_{4.6})$ and 171.4 °C for $Ti_{48.5}(Pt_{43.6},V_{7.9})$ phase, Table 4-7 and Figure 4.1.9(b). There was an increase in the thermal hysteresis of solution heat treated alloy samples. The peak sizes and latent heats of formation reduced with increasing V content, signalling a reduced amount of the transforming TiPt phase.

Table 4-7: Transformation temperatures, transformation hysteresis and transformation enthalpy of (a) $Ti_{51.2}Pt_{48.8}$ and $Ti_{50.9}Pt_{50.1}$, (b) $Ti_{51.5}(Pt_{44},V_{4.5})$ and $Ti_{51}(Pt_{44.4},V_{4.6})$ and (c) $Ti_{48.5}(Pt_{43.6},V_{7.9})$ and $Ti_{50.4}(Pt_{45.1},V_{4.5})$ phases during heating and cooling for the second DSC thermal cycle.

Phase	A_s (ºC)	A_f (ºC)	M_s (ºC)	M_f (ºC)	ΔT (ºC)	ΔH (J/g) forward/reverse	
			As-cast				
$Ti_{51.2}Pt_{48.8}$	1031	1076	1015	986	61	26.0	-23.5
$Ti_{51.5}(Pt_{44},V_{4.5})$	974	1057	891	791	166	9.9	-19.4
$Ti_{48.5}(Pt_{43.6},V_{7.9})$	968	1048	875	814	173	9.4	-12.7
			Solution heat treated				
$Ti_{50.9}Pt_{49.1}$	1031	1074	1014	981	60	18.6	-16.9
$Ti_{51}(Pt_{44.4},V_{4.6})$	961	1060	889	705	171	14.5	-17.7
$Ti_{50.4}(Pt_{45.1},V_{4.5})$	964	1059	878	768	181	9.9	-12.8

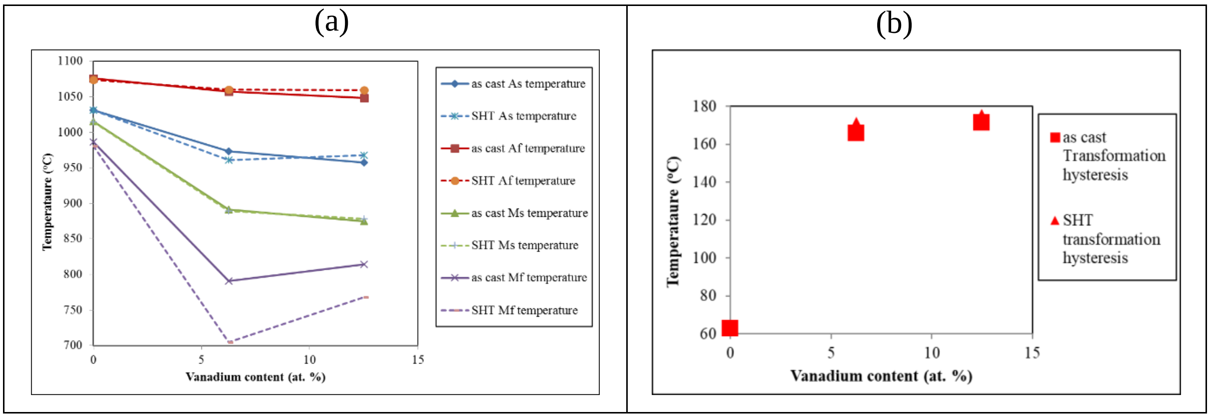

Figure 4.1.9: Composition dependence of the transformation temperatures (a) and transformation hysteresis (b) as a function of V content on the as-cast and solution heat treated Ti-(Pt-V) alloy samples. Solid and dashed lines respectively.

4.1.4. The effect of ternary alloying with V on the mechanical properties of Ti-Pt alloys

Figure 4.1.10 displays compressive stress-strain curves of as-cast and solution heat treated Ti_{50}-Pt_{50}, Ti_{50}-$Pt_{43.75}$-$V_{6.25}$ and Ti_{50}-$Pt_{37.5}$-$V_{12.5}$ alloys. The detwinning stress (σ_{det}), 0.2% yield strength (σ_y), fracture strength (σ_f) and plastic strain (ε_p) of the alloys are summarized in Table 4-8.

The binary Ti_{50}-Pt_{50} exhibited a typical double yielding behavior of shape memory alloys, representing the detwinning stress and yield strength from the stress-strain curve, Figure 4.1.10. The alloy achieved a σ_{det} and σ_y of 513±33 and 1478±24 MPa. The detwinning stress indicated an accommodation of the applied strain by the martensite reorientation process. The maximum applied strain and stress that the alloy could endure before fracture was 23.4±0.03% and 2475±257 MPa. The σ_{det}, σ_y and σ_f of Ti-Pt increased after SHT with a slight decrease in the plastic strain, Table 4-8. The decrease in plastic strain after SHT was associated with a slight decrease in the ductility of the material, which is the ability of a material to undergo significant plastic deformation before failure or fracture.

The partial substitution of Pt with V changed the typical double yielding behaviour of shape memory alloys to a single yielding point behaviour, indicating the occurrence of simultaneous slip deformation along with the martensite reorientation process, Figure 4.1.10. The addition of V increased the σ_y of the Ti-Pt alloy with increasing V content. However, the plastic strain was significantly decreased with the increasing V content, from 23.4±0.03 to 15.6±0.1% for Ti_{50}-$Pt_{43.75}$-$V_{6.25}$ and 10.6±0.4% for Ti_{50}-$Pt_{37.5}$-$V_{12.5}$ in the as cast condition, indicating an accommodation of higher stresses with low plastic strains before fracture, Figure 4.1.11. The decrease in plastic strains of Ti-Pt with increasing V content was associated with a decrease in ductility of Ti-Pt with increasing V content. It was worth noting that the fracture strength was decreasing with increasing V additions to Ti-Pt. Solution heat treatment of the as-cast alloys further increased the yield strength of Ti-Pt with increasing V content, Figure 4.1.10 and Table 4-8. The plastic strain and fracture strength of Ti-Pt was further decreased with increasing V contents after SHT, Table 4-8 and Figure 4.1.11.

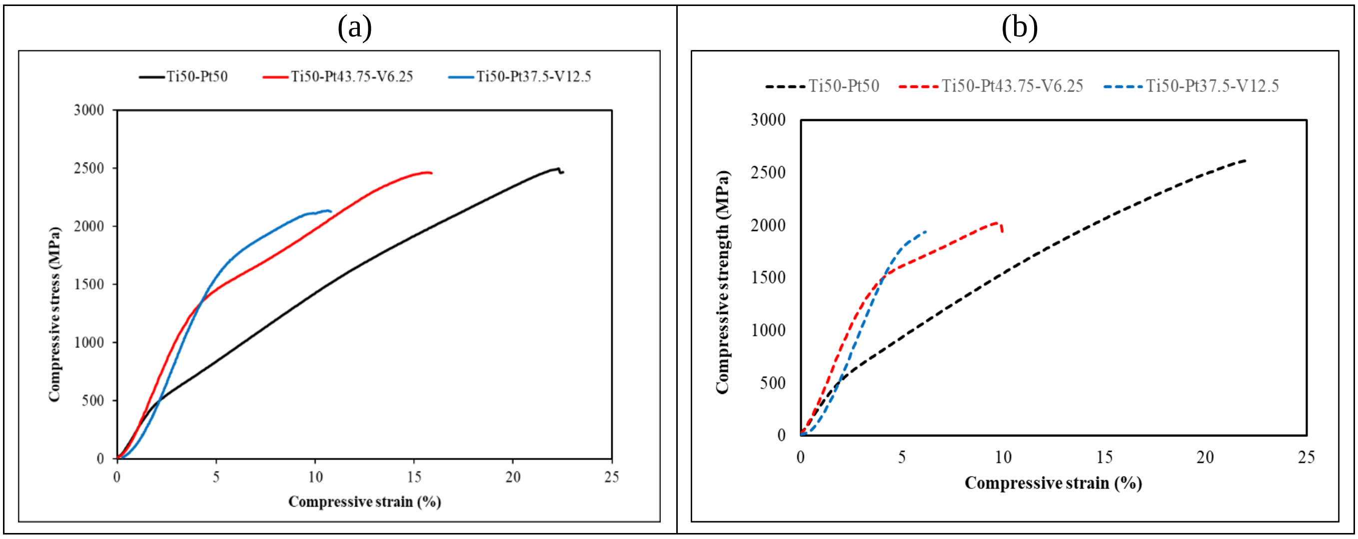

Figure 4.1.10: Compressive stress-strain curves of Ti_{50}-Pt_{50}, Ti_{50}-$Pt_{43.75}$-$V_{6.25}$ and Ti_{50}-$Pt_{37.5}$-$V_{12.5}$ alloys in the (a) as-cast and (b) solution heat treated conditions.

Table 4-8: Mechanical properties of Ti_{50}-Pt_{50}, Ti_{50}-$Pt_{43.75}$-$V_{6.25}$ and Ti_{50}-$Pt_{37.5}$-$V_{12.5}$ alloys in the as-cast and solution heat treated conditions: detwinning stress (σ_{det}), yield strength (σ_y), fracture strength (σ_f) and plastic strain (ε_p).

Alloy	σ_{det} (MPa)	0.2% σ_y (MPa)	σ_f (MPa)	ε_p (%)
		As-cast		
Ti_{50}-Pt_{50}	513±33	1478±24	2475±257	23.4±0.04
Ti_{50}-$Pt_{43.75}$-$V_{6.25}$	-	1518±28	2463±119	15.6±0.1
Ti_{50}-$Pt_{37.5}$-$V_{12.5}$	-	1920±16	2137±100	10.6±0.4
		Solution heat treated		
Ti_{50}-Pt_{50}	658±3	1500±14	2614±86	21.8±0.1
Ti_{50}-$Pt_{43.75}$-$V_{6.25}$	-	1589±65	2021±79	9.8±0.01
Ti_{50}-$Pt_{37.5}$-$V_{12.5}$	-	1849±164	1936±82	6.1±0.02

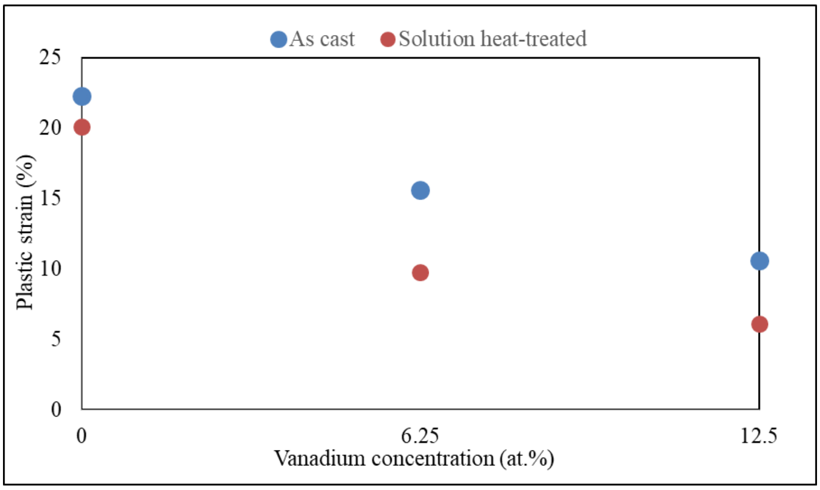

Figure 4.1.11: The influence of V content on the plastic strain, ε_p of Ti-Pt-V alloys.

Macro Vickers hardness tests were carried out on the as-cast and solution heat treated Ti-Pt-V alloys in order to further investigate the hardening effect of V to Ti-Pt. The Vickers hardness (VHN) values are summarized in Table 4-9. The binary Ti-Pt alloy had a Vickers hardness value of 321±5 HV in the as-cast condition, and after SHT, the hardness was 347±10 HV, showing an increase after SHT.

Figure 4.1.12 shows that the addition of V to Ti-Pt significantly increased the hardness with increasing V contents. Higher hardness values were obtained after SHT, indicating that Ti-Pt was further hardened by the SHT.

Table 4-9: Macro Vickers hardness values of the as-cast and solution heat treated Ti-(Pt-V) alloys.

Alloy	Macro Vickers hardness (VHN)
As-cast	
Ti_{50}-Pt_{50}	321±5
Ti_{50}-$Pt_{43.75}$-$V_{6.25}$	522±11
Ti_{50}-$Pt_{37.5}$-$V_{12.5}$	565±13
Solution heat treated	
Ti_{50}-Pt_{50}	347±10
Ti_{50}-$Pt_{43.75}$-$V_{6.25}$	547±13
Ti_{50}-$Pt_{37.5}$-$V_{12.5}$	669±15

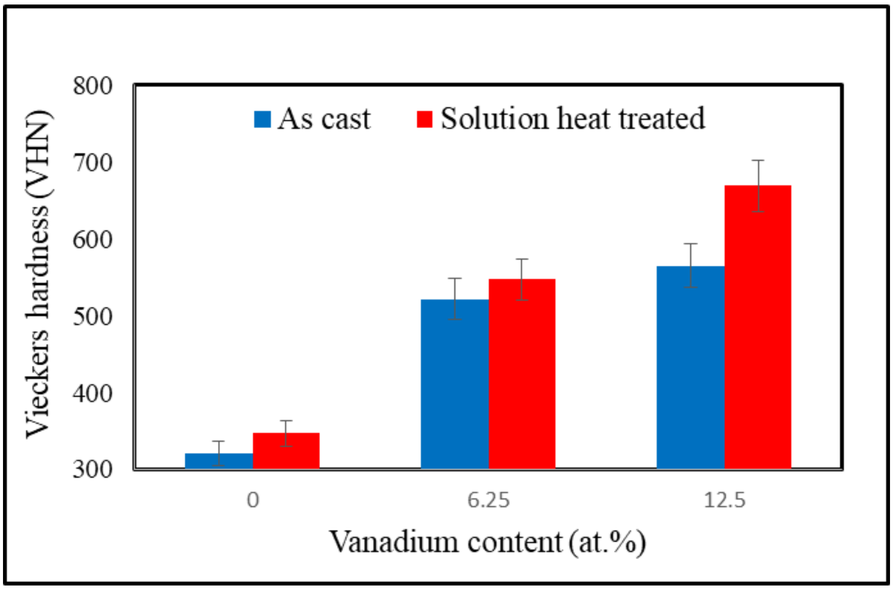

Figure 4.1.12: Macro Vickers hardness of Ti-Pt-V alloys as a function of V content after arc melting and SHT.

4.1.5. The effect of ternary alloying with V on the shape memory effect of Ti-Pt alloys

A loading–unloading compression test was done at room temperature i.e. below the martensitic transformation temperature, on as-cast and solution heat treated Ti-Pt-V alloys. The shape memory effect was studied by the compressive deformation of the alloys up to a compressive strain of 5%. Prior to deformation, the alloys had a twinned B19 martensite structure. It is assumed that after deformation at room temperature, the deformed phase called the detwinned B19 martensite phase was formed. The recoverable strain was associated with the transformation of the detwinned martensite to the austenite phase. After quenching the alloy samples from the austenite phase region, the martensite again formed into a self-accommodated, twinned martensite structure.

Table 4-10 shows that the binary Ti-Pt alloy obtained a shape memory strain and shape recovery ratio (SRR) of 1.7% and 83.5% in the as-cast condition, However, after SHT, the shape memory strain and SRR significantly decreased to 0.8% and 31.2%, indicating a deterioration of the shape memory behaviour after SHT. The decrease in the SRR was associated with an increased irrecoverable strain, ε_{irr}.

Figure 4.1.13 shows that the partial substitution of Pt with V decreased the shape memory strain and shape recovery ratio of Ti-Pt with increasing V content in the as-cast condition, except for Ti_{50}-$Pt_{37.5}$-$V_{12.5}$. The Ti_{50}-$Pt_{37.5}$-$V_{12.5}$ alloy did not show any clear difference between the yield strength and fracture strength, which is evidence that at deformation strains of 5%, the alloy was in the elastic region of the compressive stress-strain curve, hence the 100% SRR, corresponding to no irrecoverable strain (ε_{irr}), Table 4-10.

After SHT, the addition of 6.25 at.% V improved the shape memory strain and shape recovery of the Ti-Pt alloy, Figure 4.1.13. The increase in SRR was significant although it was lower than in the as-cast condition. There was a slight decrease in the shape memory strain with the addition of 12.5 at.% V after SHT, while the SRR was improved from 31.2% for Ti_{50}-Pt_{50} to 67% for Ti_{50}-$Pt_{37.5}$-$V_{12.5}$ alloy. This indicated that the SRR of solution heat treated binary Ti-Pt was significantly increased by the addition of V after SHT.

Table 4-10: Room temperature shape memory behaviour of Ti_{50}-Pt_{50} and Ti-Pt-V alloys at an applied strain of 5%.

Alloy	ε_{irr}	ε_{sme} (%)	SRR (%)
As-cast			
Ti_{50}-Pt_{50}	0.003	1.7	83.5
Ti_{50}-$Pt_{43.75}$-$V_{6.25}$	0.002	0.8	83
Ti_{50}-$Pt_{37.5}$-$V_{12.5}$	0	1.0	100
Solution heat treated			
Ti_{50}-Pt_{50}	0.018	0.8	31.2
Ti_{50}-$Pt_{43.75}$-$V_{6.25}$	0.005	1.0	66.67
Ti_{50}-$Pt_{37.5}$-$V_{12.5}$	0.003	0.7	67.0

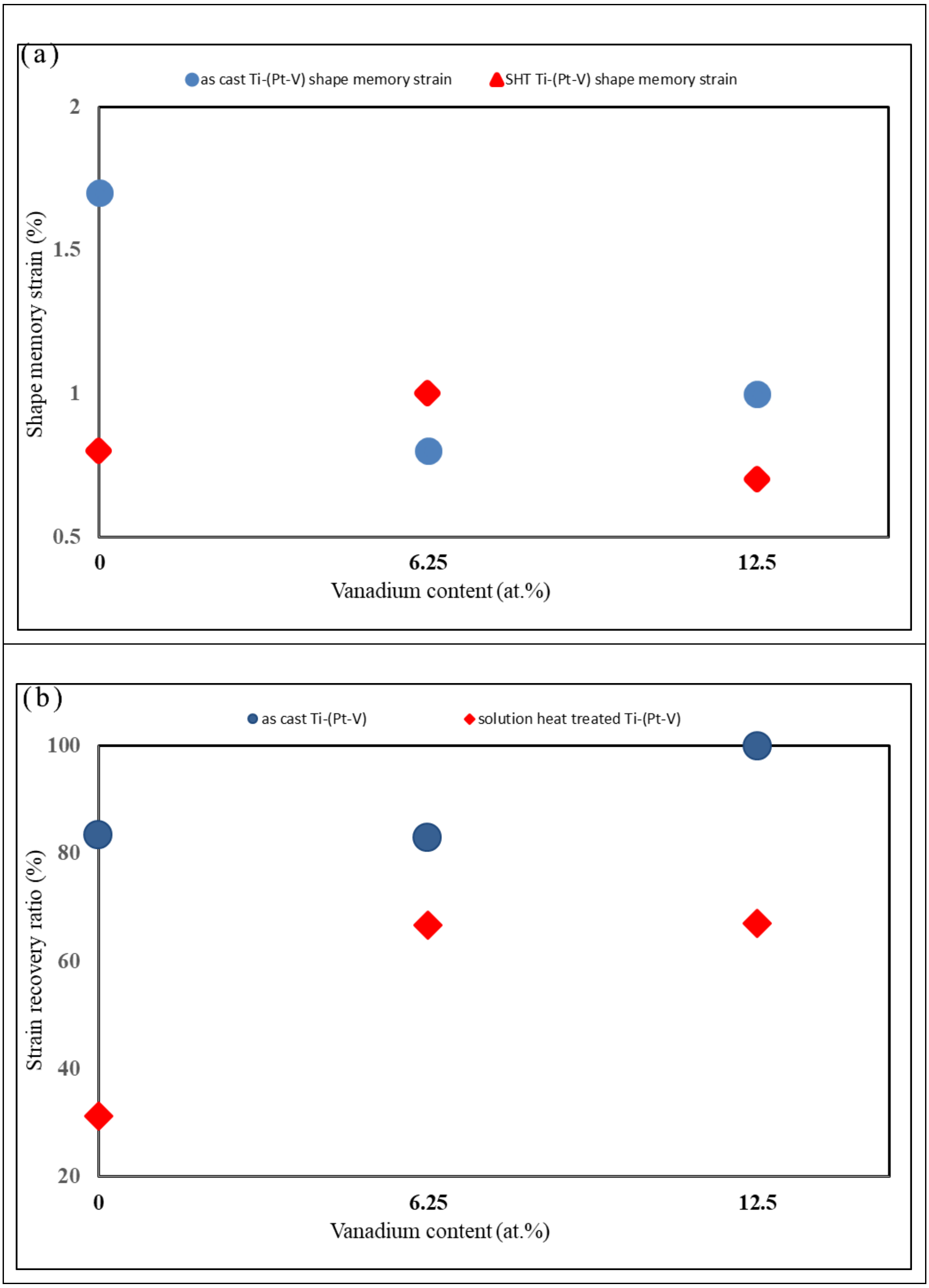

Figure 4.1.13: The effect of V content on the (a) shape memory strain and (b) strain recovery ratio of Ti-Pt-V alloys at an applied strain of 5%.

The Ti-Pt-V alloys were also deformed with compressive strains greater than 5% at room temperature. The mechanical properties determined in Section 4.1.4 were used to obtain maximum compressive strains where shape memory behaviour could be exhibited below the plastic limit on the compressive stress-strain curve. Since Ti-Pt-V alloys exhibited a single yielding point, it was difficult to differentiate between the martensite reorientation stress and yield stress. However, the DSC analysis clearly showed that there was a B2 to B19 transformation in these alloys. Therefore, specimens deformed above a compressive strain of 5% at room temperature were used to measure the shape memory behaviour. The applied strains were varied due to differences in the elastic behaviour of the alloys observed in Figure 4.1.10. According to the compressive stress-strain curve for each alloy, compression tests were carried out at compressive strains of 15% for the as-cast and solution heat treated Ti_{50}-Pt_{50}, 10.1 and 7.5% for Ti_{50}-$Pt_{43.75}$-$V_{6.25}$ and, 7.5 and 4.5% for Ti_{50}-$Pt_{37.5}$-$V_{12.5}$ alloys.

The ε_{sme} and SRR of binary Ti-Pt deteriorated after deforming at a compressive strain of 15%, which was greater than 5%, Table 4-11. This behaviour was expected since the alloy was deformed at a higher strain, which was at the plastic region of the compressive stress-strain curve i.e. regions between the yield strength and the plastic limit, which was believed to be associated with higher irrecoverable strains, Table 4-11. After SHT of the binary Ti-Pt, the ε_{sme} and SRR had decreased further.

Figure 4.1.14 shows that the SRR of Ti-Pt increased with increasing V content at deformation strains greater than 5% in both the as-cast and solution heat treated conditions. However, this SRR of Ti-Pt-V alloys was lower than at deformation strains of 5%. The shape recovery ratio of 100% for Ti_{50}-$Pt_{37.5}$-$V_{12.5}$, was because the applied strain of 4.45% to this alloy was in the elastic region of the stress-strain curve in Figure 4.1.10.

The Ti_{50}-$Pt_{43.75}$-$V_{6.25}$ alloy exhibited an improved shape memory strain of 2.9% and 1.7% in the as-cast and solution heat treated conditions, compared to deformations at compressive strains of 5%, Figure 4.1.14. This indicated that at deformation strains greater than 5%, the addition of V improves the shape memory effect of Ti-Pt. The shape memory effect of Ti_{50}-$Pt_{37.5}$-$V_{12.5}$ at deformation strains of 7.5% was better than at deformation strains of 5% in the as-cast condition. The ε_{sme} of Ti_{50}-$Pt_{37.5}$-$V_{12.5}$ of 0.5% could not be used, since the applied compressive strain of 4.45% was in the elastic region of the stress-strain curve after SHT.

Table 4-11: Shape memory effect calculations of Ti_{50}-Pt_{50}, Ti_{50}-$Pt_{43.75}$-$V_{6.25}$ and Ti_{50}-$Pt_{37.5}$-$V_{12.5}$ alloys at compressive strains greater than 5%.

Alloy	ε_{irr}	ε_{sme} (%)	SRR (%)
As-cast			
Ti_{50}-Pt_{50}	0.09	1.7	16.5
Ti_{50}-$Pt_{43.75}$-$V_{6.25}$	0.02	2.9	55.8
Ti_{50}-$Pt_{37.5}$-$V_{12.5}$	0.01	1.5	68.2
Solution heat treated			
Ti_{50}-Pt_{50}	0.09	1.2	11.1
Ti_{50}-$Pt_{43.75}$-$V_{6.25}$	0.01	1.7	53.1
Ti_{50}-$Pt_{37.5}$-$V_{12.5}$	0	0.5	100

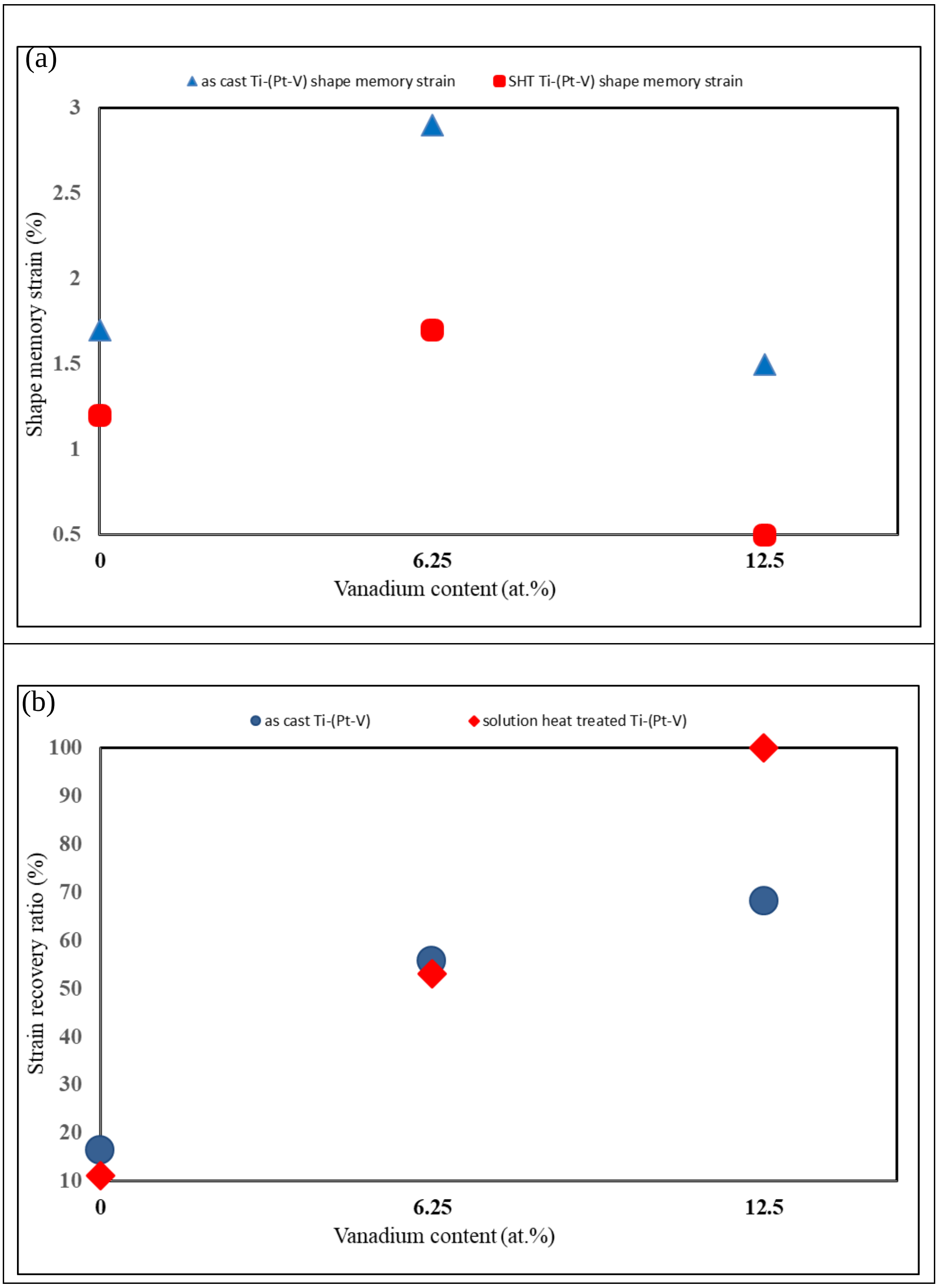

Figure 4.1.14: The effect of V content on the (a) shape memory strain and (b) strain recovery ratio of Ti-Pt-V alloys at applied strains greater than 5%.

4.2. The effect of ternary alloying with V replacing Ti on the functional properties of Ti-Pt alloys

Microstructural analysis, phase identification, crystal structure, phase transformation and mechanical properties of Ti-Pt when V substituted Ti was carried out in the as-cast and solution heat treated conditions. The binary Ti-Pt alloy was used as a baseline and the V content was varied from 0 to 12.5 at.%.

4.2.1. The effect ternary alloying with V when substituting for Ti on the microstructural evolution of Ti-Pt alloy

Figures 4.2.1 and 4.2.2 show SEM backscattered electron images (BEI) and EDX results of $Ti_{43.75}$-$V_{6.25}$-Pt_{50} and $Ti_{37.5}$-$V_{12.5}$-Pt_{50} alloys in the as-cast and solution heat treated conditions. The SHT was done at 1250 ^{o}C for 72 hours, followed by ice water quenching. Both as-cast and solution heat treated microstructures had multiple phases. The chemical compositions for all phases are the average values taken from three different areas of the sample. The overall compositions in Tables 4-12 and 4-13 were slightly different from the intended compositions, but the difference was within the error margin of EDX measurements.

4.2.1.1. $Ti_{43.75}$-$V_{6.25}$ -Pt_{50} alloy

The microstructure of $Ti_{43.75}$-$V_{6.25}$-Pt_{50} alloy consisted of (Ti,V)Pt dendrites and fine interdendritic regions, Figure 4.2.1(a) and (b). The interdendritic regions comprised TiO and fine TiPt and Ti_3Pt phases. The composition of the (Ti,V)Pt and Ti_3Pt phases in the interdendritic regions was undetectable due to SEM limitations. The EDX overall composition showed that the alloy had 49.5±0.2 at.% Pt with (Ti,V)Pt phase comprised of 5.2±0.3 at.% V, Table 4-12.

The SHT of the as-cast structure resulted in the elimination of interdendritic regions and formation of (Ti,V)Pt matrix and TiO phase, Figure 4.2.1(c) and (d). The EDX overall composition showed that the alloy had 49.4±0.2 at. % Pt after the SHT with a (Ti,V)Pt phase consisting of 5.2±0.2 at.% V which was still close to the as-cast (5.3±0.7 at.% V), Table 4-12.

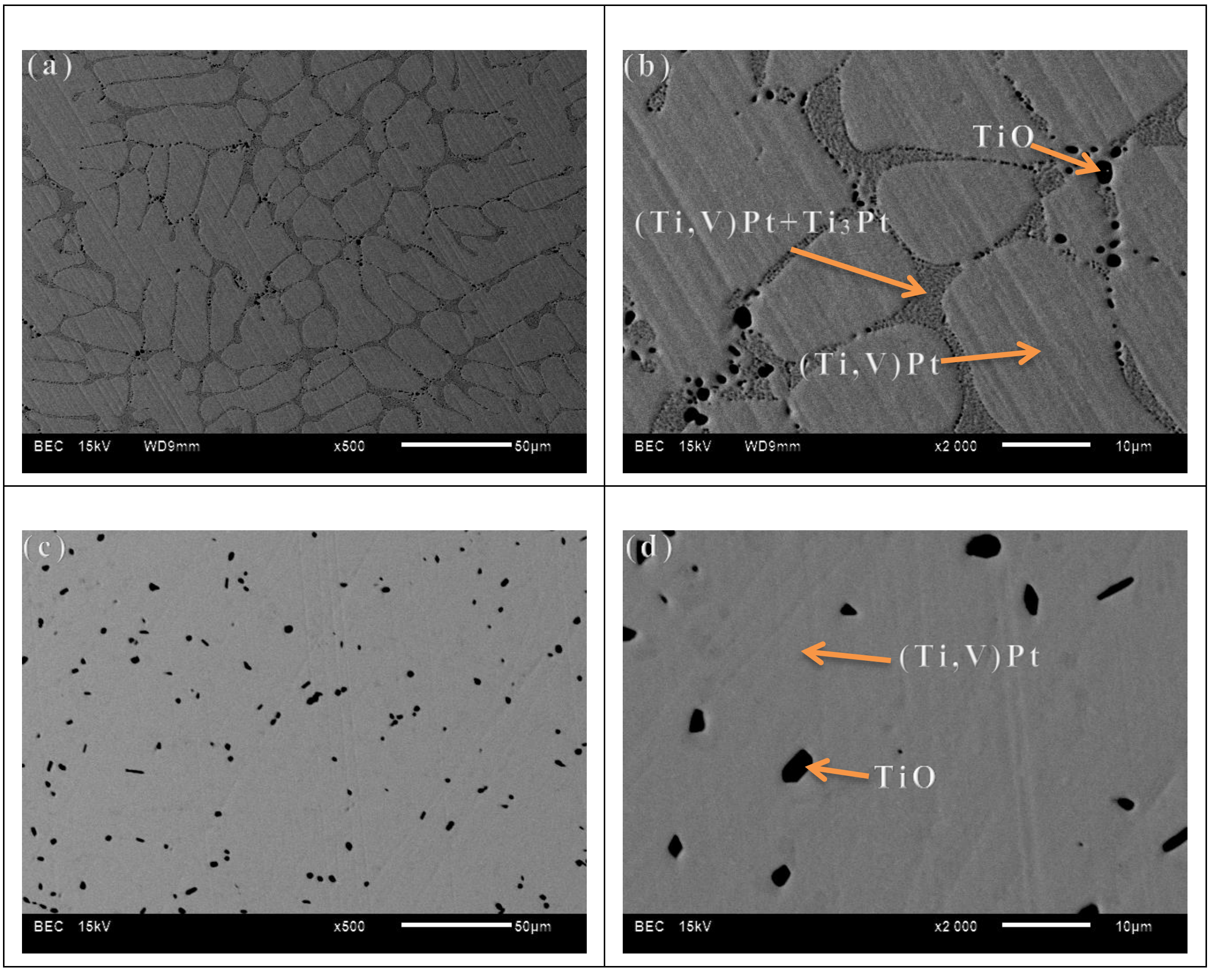

Figure 4.2.1: SEM backscattered electron images (BEI) of $Ti_{43.75}$-$V_{6.25}$-Pt_{50}, low and high magnification in the as-cast condition (a-b) and solution heat treated at 1250°C for 72 hr followed by ice water quenching (c-d).

Table 4-12: SEM-EDX results of $Ti_{43.75}$-$V_{6.25}$-Pt_{50} in the as-cast and solution heat treated conditions.

	O	Ti	V	Pt
		As-cast (at. %)		
Overall	-	45.3±0.4	5.2±0.3	49.5±0.2
(Ti,V)Pt	-	44.6±0.9	5.3±0.5	50.1±0.5
TiO	44.4±1.9	48.8±0.6		6.8±0.1
		Solution heat treated (at. %)		
Overall	-	45.8±0.5	4.8±0.2	49.4±0.2
(Ti,V)Pt	-	44.9±1.2	5.2±0.7	49.9±0.6
TiO	50.1±2	45.5±0.6	-	4.4±0.2

4.2.1.2. $Ti_{37.5}$-$V_{12.5}$-Pt_{50} alloy

The as-cast $Ti_{37.5}$-$V_{12.5}$-Pt_{50} had a microstructure that consisted of (Ti,V)Pt dendrites and interdendritic regions comprised of Ti_3Pt, (Ti,V)Pt and TiO oxide phases, Figure 4.2.2(a) and (b). The TiO oxide phase was similar to the one detected in the $Ti_{43.75}$-Pt_{50}-$V_{6.25}$ alloy, however, it was larger in amounts and size. The EDX results from the SEM revealed that the alloy had 47.9±0.2 at.% Pt and the transforming (Ti, V) Pt phase contained 11.7±0.7 at.% V, Table 4-13.

The SHT of the $Ti_{37.5}$-Pt_{50}-$V_{12.5}$ alloy led to the formation of (Ti, V)Pt and coarsened TiO phases, Figure 4.2.2(c) and (d). The EDX overall composition showed that the alloy had 47.6±0.4 at. % Pt with a (Ti,V)Pt phase consisting of 12±2.6 at.% V after the SHT, Table 4-13.

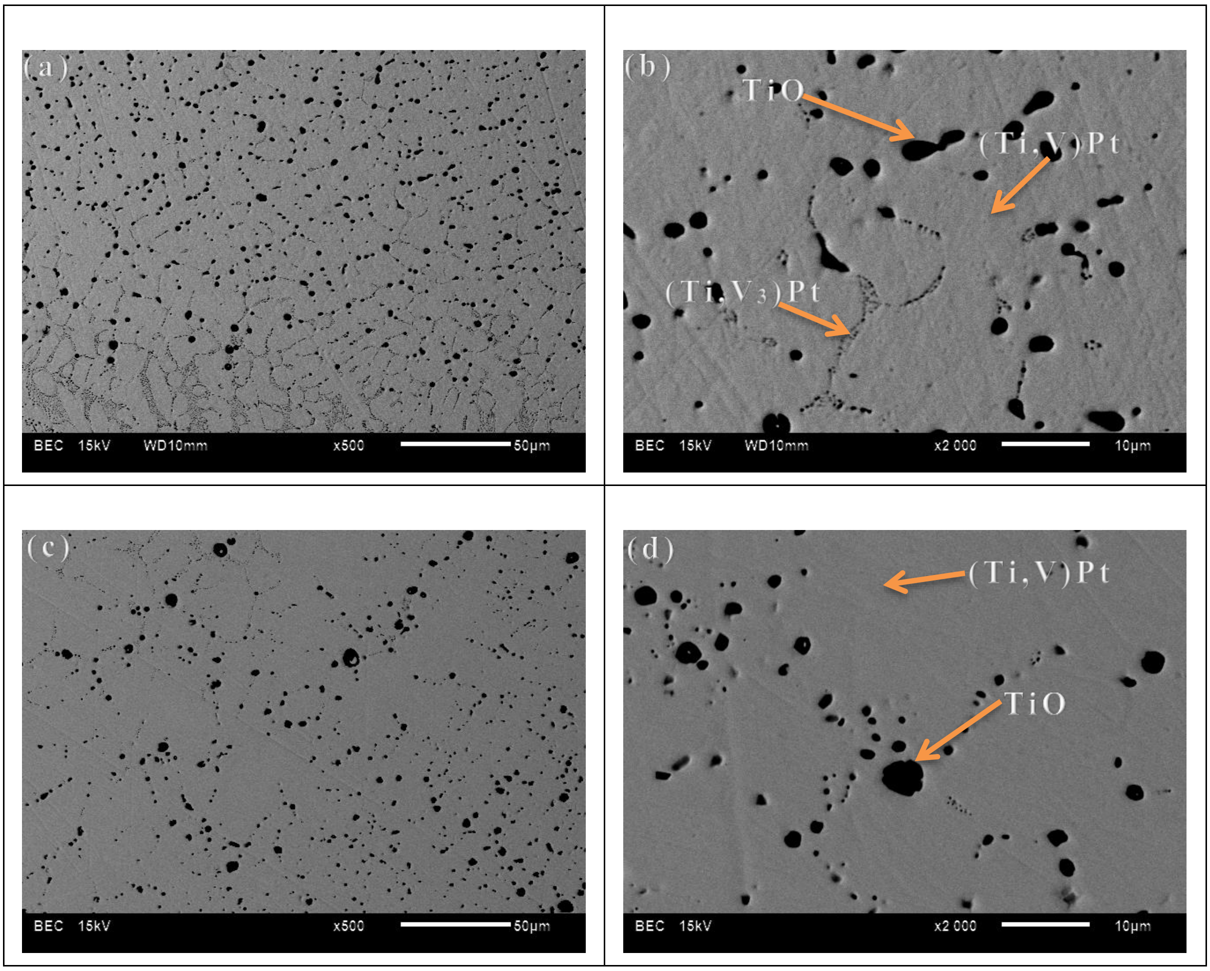

Figure 4.2.2: SEM backscattered electron images (BEI) of $Ti_{37.5}$-$V_{12.5}$-Pt_{50}, low and high magnification in the as-cast condition (a-b) and solution heat treated at 1250°C for 72 hr followed by ice water quenching (c-d).

Table 4-13: SEM-EDX results of $Ti_{37.5}$-$V_{12.5}$-Pt_{50} in the as-cast and solution heat treated conditions.

	O	Ti	V	Pt
		As-cast (at. %)		
Overall	-	39.5±0.4	12.6±0.4	47.9±0.2
(Ti,V)Pt	-	38.5±0.8	11.7±0.7	49.8±0.6
$(Ti,V_3)Pt$	-	60.6±0.7	9.3±0.3	30.1±0.2
TiO	53.6±1.7	45.4±0.5		1±0.04
		Solution heat treated (at. %)		
Overall	-	40.6±0.9	11.8±0.7	47.6±0.4
(Ti,V)Pt	-	39.4±3.5	12.0±2.6	48.6±2.0
TiO	54.3±1.7	45.2±0.5	-	0.4±0.03

4.2.2. The effect of ternary alloying with V on the crystal structure of Ti-Pt alloys

Figure 4.2.3 depicts XRD results of Ti-Pt after partial substitution of Ti with V (6.25 and 12.5 at.%) in the as-cast and solution heat treated conditions. The binary Ti_{50}-Pt_{50} XRD results were included for comparison. All alloys, both in the as-cast and solution heat treated conditions show diffraction patterns of B19 (Ti,V)Pt crystal structure and the angle did not change from 90°. This indicated that the austenite to martensite transformation occurred with the addition of V.

The Ti_3Pt phase observed during SEM analysis was not detected in the $Ti_{43.75}$-$V_{6.25}$-Pt_{50} and $Ti_{37.5}$-$V_{12.5}$-Pt_{50} alloys, which was contrary to SEM-EDX results. The latter was attributed to the low quantities of Ti_3Pt phase in the Ti_{50}-Pt_{50}, $Ti_{43.75}$-$V_{6.25}$-Pt_{50} and $Ti_{37.5}$-$V_{12.5}$-Pt_{50} , which were below the detection limits of the X-ray technique. Table 4-14 shows a summary of the lattice parameters of the B19 (Ti,V)Pt martensite structure estimated by the Rietveld method using the Maud software. The lattice parameter ratios of the B19 phase were plotted as a function of increasing V concentration in Figure 4.2.4.

The addition of V when replacing Ti shifted the B19 diffraction peaks to slightly higher 2θ angles in the as-cast condition, indicating a reduction of the unit cell volume. The XRD patterns of the alloys shifted to slightly lower 2θ angles after SHT, indicating an increase in the lattice parameters of the unit cell. However, a decrease in lattice parameters with increasing V content was maintained after SHT.

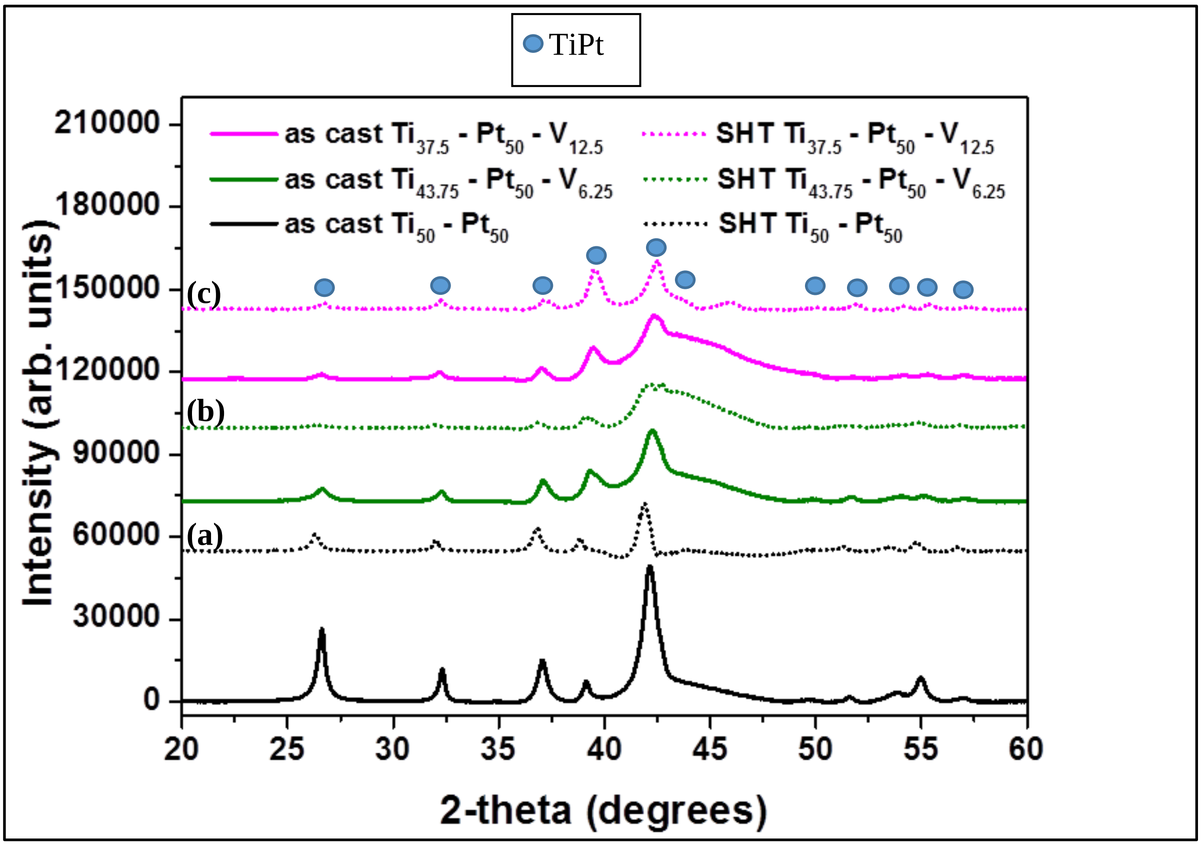

Figure 4.2.3: XRD results of (a) Ti_{50}-Pt_{50}, (b) $Ti_{43.75}$-$V_{6.25}$-Pt_{50} and (c) $Ti_{37.5}$-$V_{12.5}$-Pt_{50} in the as-cast and solution heat treated conditions using Cu-K_{α} radiation.

Table 4-14: Lattice parameters of the B19 (Ti,V)Pt phase in the as-cast and solution heat treated conditions of Ti-V-Pt alloys.

Lattice parameter (Å)	As-cast	Solution heat treated
	Ti_{50} – Pt_{50} : B19 TiPt	
a	4.60±0.090	4.64±0.001
b	2.77±0.072	2.79±0.145
c	4.86±0.111	4.93±0.001
	$Ti_{43.75}$-$V_{6.25}$-Pt_{50} : B19 (Ti,V)Pt	
a	4.58±0.001	4.58±0.002
b	2.78±0.001	2.78±0.002
c	4.86±0.003	4.86±0.004
	$Ti_{37.5}$-$V_{12.5}$-Pt_{50} : B19 (Ti,V)Pt	
a	4.55±0.002	4.54±0.002
b	2.77±0.002	2.76±0.001
c	4.84±0.004	4.83±0.002

In Figure 4.2.4, a/b, c/b and c/a lattice parameter ratios were found to be greater than 1.0 with a/b and c/b greater than 1.4, indicating that the structure of the B19 martensite phase remained orthorhombic throughout.

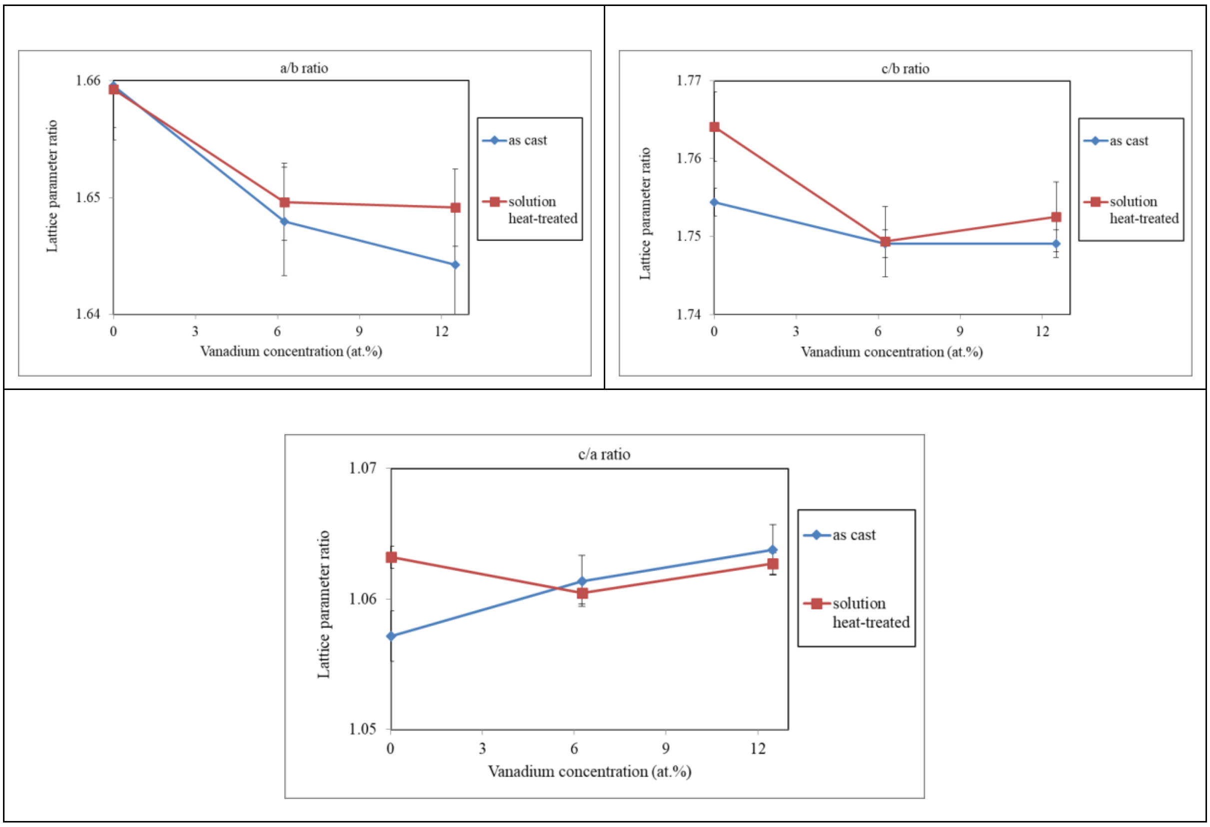

Figure 4.2.4: Change in lattice parameter ratio of the B19 phase as a function of V concentration when substituting Ti, (a) a/b, (b) c/b and (c) c/a.

4.2.3. The effect of ternary alloying with V on the phase transformation of Ti-Pt alloys

Differential scanning calorimetry (DSC) was performed on the as-cast and solution heat treated Ti-V-Pt alloy samples. The SEM-EDX results revealed that the exact compositions of the transforming TiPt phases deviated from the nominal compositions as follows: The Ti$_{50}$-Pt$_{50}$ sample formed Ti$_{51.2}$Pt$_{48.8}$ and Ti$_{50.9}$Pt$_{49.1}$ (at.%), the Ti$_{43.75}$-V$_{6.25}$-Pt$_{50}$ sample formed (Ti$_{44.6}$,V$_{5.3}$)Pt$_{50.1}$ and (Ti$_{44.9}$,V$_{5.2}$)Pt$_{49.9}$, and the Ti$_{37.5}$-V$_{12.5}$-Pt$_{50}$ formed (Ti$_{38.5}$,V$_{11.70}$)Pt$_{49.8}$ and Ti$_{38.7}$-Pt$_{50.1}$-V$_{11.2}$. The DSC results measured the transformation temperature of the resulting composition of the TiPt phase after arc melting and SHT. The samples were heated and cooled twice from room temperature and only results for the second heating /cooling cycles were reported.

The DSC results of Ti$_{43.75}$-V$_{6.25}$-Pt$_{50}$ and Ti$_{37.5}$-V$_{12.5}$-Pt$_{50}$ are shown in Figure 4.2.5. The partial substitution of Ti by V changed the transformation from multiple to single step transformation. The addition of V increased the transformation temperatures of Ti-Pt with increasing V content. For example, the M$_s$ temperature increased from 1015 ^{o}C (binary) to 1095 ^{o}C for

$(Ti_{44.6},V_{5.3})Pt_{50.1}$ and 1296 °C for $(Ti_{38.5},V_{11.70})Pt_{49.8}$ phases in the as-cast condition. There was no significant change in transformation temperatures after SHT, Figure 4.2.6(a).

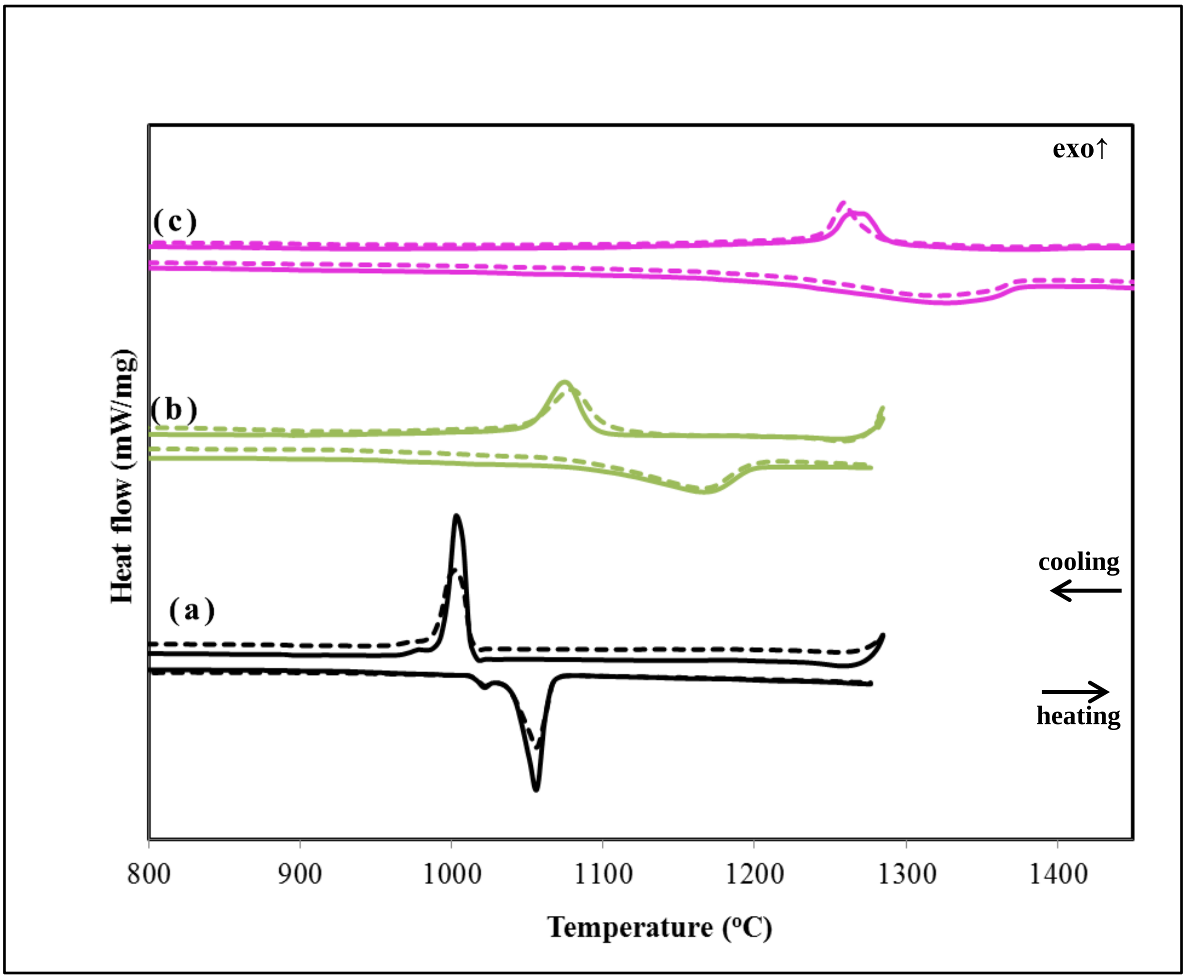

Figure 4.2.5: Second cycling DSC curves of (a) $Ti_{50}Pt_{50}$, (b) $Ti_{43.75}$-$V_{6.25}$-Pt_{50} and (c) $Ti_{37.5}$-$V_{12.5}$-Pt_{50} (at.%) alloys in the as-cast and solution heat treated conditions, solid and dashed lined.

The addition of V increased the thermal hysteresis (ΔT) of Ti-Pt from 61 to 113 °C for $(Ti_{44.6},V_{5.3})$ $Pt_{50.1}$ and 90 °C for $(Ti_{38.5},V_{11.7})Pt_{49.8}$, Table 4-15 and Figure 4.2.6(b). However after SHT, the thermal hysteresis decreased but were still above that of binary TiPt, Figure 4.2.6(b).

There was a decrease in peak sizes and latent heats of formation (ΔH) of the forward transformation with increasing V contents. Solution heat treatment further decreased the latent heats of formation, Figure 4.2.5 and Table 4-15.

Table 4-15: Transformation temperatures, hysteresis and enthalpy of (Ti,V)Pt during the second DSC heating and cooling thermal cycles in the as-cast and solution heat treated conditions.

Phase	A_s (°C)	A_f (°C)	M_s (°C)	M_f (°C)	ΔT (°C)	ΔH (J/g) forward/reverse	
As-cast							
$Ti_{51.2}Pt_{48.8}$	1031	1076	1015	986	61	26.0	-23.5
$(Ti_{44.6}, V_{5.3})Pt_{50.1}$	1077	1208	1095	1041	113	16.4	-22.2
$(Ti_{38.5},V_{11.70})Pt_{49.8}$	1171	1386	1296	1228	90	12.6	-29.2
Solution heat treated							
$Ti_{50.9}Pt_{49.1}$	1031	1074	1014	981	60	18.6	-16.9
$(Ti_{44.9}, V_{5.2})Pt_{49.9}$	1070	1215	1112	1032	103	17.9	-27.8
$(Ti_{38.7},V_{11.2})Pt_{50.1}$	1175	1380	1292	1193	88	12.8	-25.4

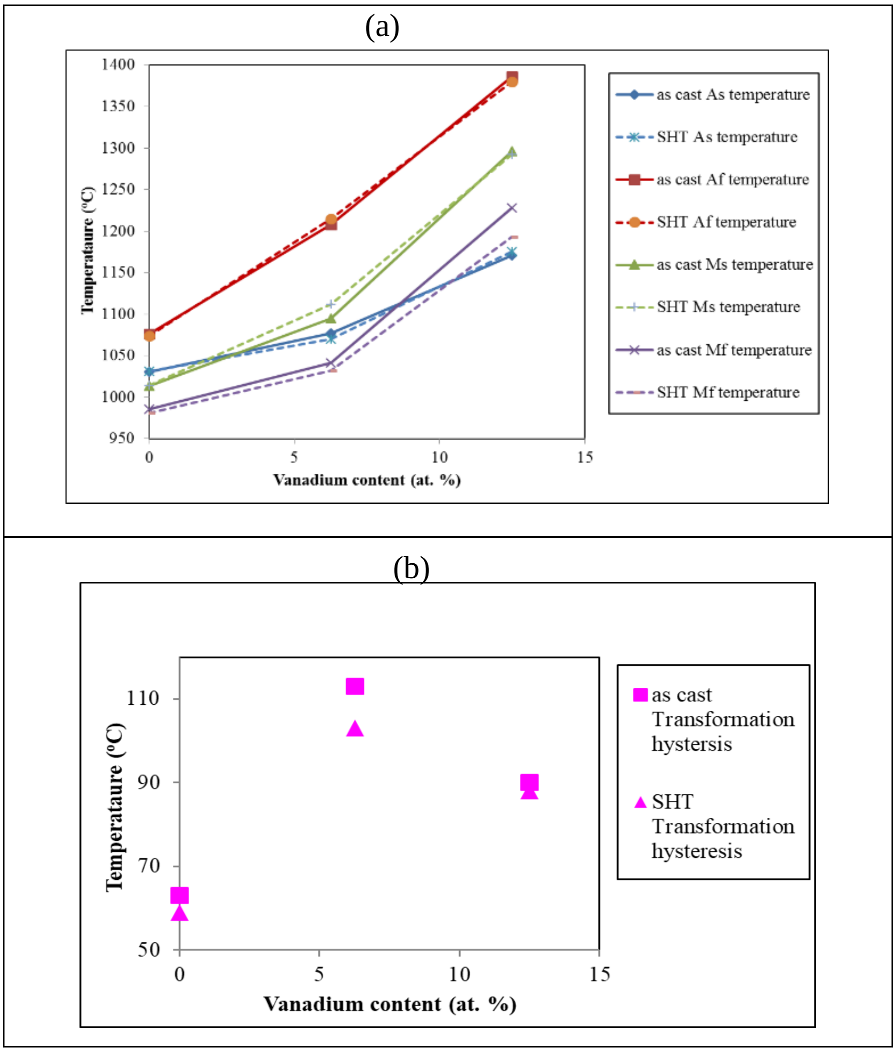

Figure 4.2.6: (a) Transformation temperatures and (b) Transformation hysteresis as a function of V content of (Ti,V)Pt in the as-cast and solution heat treated conditions, solid and dashed lines respectively.

4.2.4. The effect of ternary alloying with V on the mechanical properties of Ti-Pt alloys

Figure 4.2.7 shows the compressive stress-strain curves of Ti_{50}-Pt_{50}, $Ti_{43.75}$-$V_{6.25}$-Pt_{50} and $Ti_{37.5}$-$V_{12.5}$-Pt_{50} alloys after arc melting and SHT. The detwinning stress (σ_{det}), yield strength (σ_y), fracture strength (σ_f) and plastic strain (ε_p) of the (Ti-V)-Pt alloys are summarized in Table 4-16. The binary Ti_{50}-Pt_{50} was used for ease of comparison.

The addition of V eliminated the typical double yielding behaviour of Ti-Pt shape memory alloys, indicating the occurrence of simultaneous slip deformation along with the martensite reorientation process, Figure 4.2.7. Ternary alloying increased the σ_y of Ti-Pt with the increasing V addition, from 1478±24 (binary Ti-Pt) to 1550±12 MPa for $Ti_{43.75}$-$V_{6.25}$-Pt_{50} and 1678±91 MPa for $Ti_{37.5}$-$V_{12.5}$-Pt_{50} in the as-cast condition, Table 4-16. There was a decrease in the yield strength of Ti-V-Pt alloys after SHT. The $Ti_{43.75}$-$V_{6.25}$-Pt_{50} and $Ti_{37.5}$-$V_{12.5}$-Pt_{50} alloy samples did not fail during the compression test and the machine was stopped when the maximum load capacity was reached, except for the solution heat treated $Ti_{37.5}$-$V_{12.5}$-Pt_{50} which had a plastic strain of 15.7±0.1% associated with a σ_f of 2232±67 MPa. The behaviour of $Ti_{37.5}$-$V_{12.5}$-Pt_{50} indicated that the alloy was brittle with the addition of 12.5 at.% V.

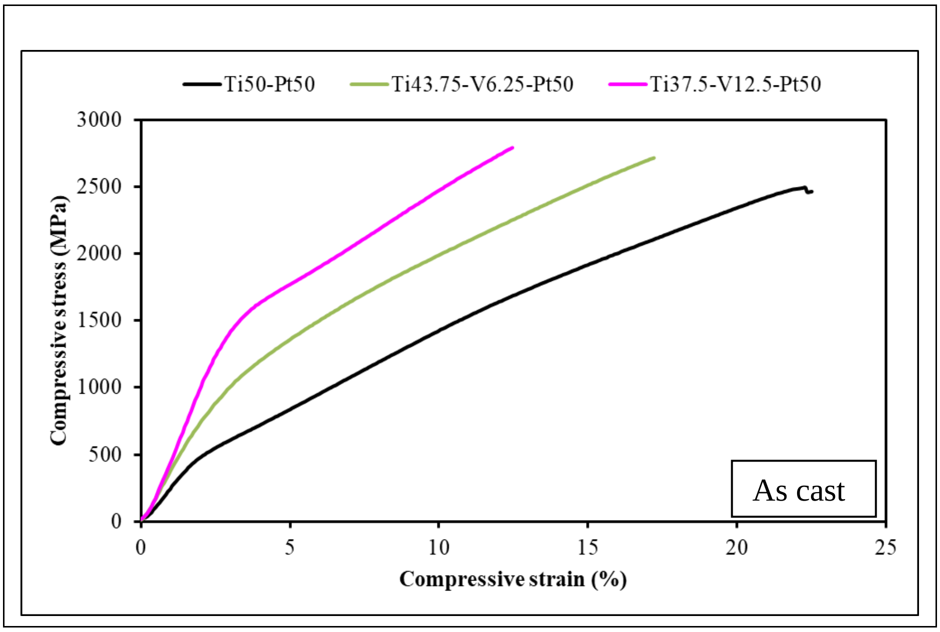

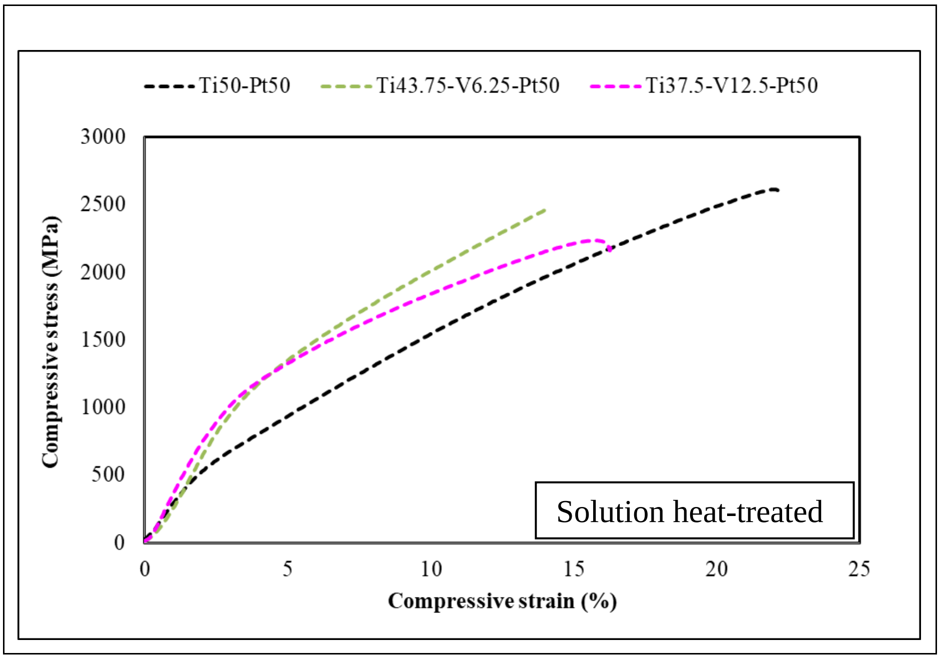

Figure 4.2.7: Compressive stress-strain curves of Ti_{50}-Pt_{50}, $Ti_{43.75}$-$V_{6.25}$-Pt_{50} and $Ti_{37.5}$-$V_{12.5}$-Pt_{50} alloys in the as-cast and solution heat treated conditions, solid and dashed lines respectively.

Table 4-16: Mechanical properties of Ti_{50}-Pt_{50}, $Ti_{43.75}$-$V_{6.25}$-Pt_{50} and $Ti_{37.5}$-$V_{12.5}$-Pt_{50} alloys in the as-cast and solution heat treated conditions: detwinning stress (σ_{det}), yield strength (σ_y), fracture strength (σ_f) and plastic strain (ε_p).

Alloy	σ_{det} (MPa)	0.2% σ_y (MPa)	σ_f (MPa)	ε_p (%)
		As-cast		
Ti_{50}-Pt_{50}	513±33	1478±24	2475±257	23.4±0.03
$Ti_{43.75}$-$V_{6.25}$-Pt_{50}		1550±12	>2749±8	>17.2±0.1
$Ti_{37.5}$-$V_{12.5}$- Pt_{50}		1678±91	>2793±153	>12.5±0.1
		Solution heat treated		
Ti_{50}-Pt_{50}	658±3	1500±14	2614±86	21.8±0.1
$Ti_{43.75}$-$V_{6.25}$-Pt_{50}		1520±118	>2471±143	>14.1±0.01
$Ti_{37.5}$-$V_{12.5}$- Pt_{50}		1480±64	2232±67	15.7±0.1

Macro Vickers hardness test results revealed that the addition of V increased the hardness of the Ti-Pt alloy with the increasing V content. For example, the hardness increased from 321±5 to 495±25 HV for $Ti_{43.75}$-$V_{6.25}$-Pt_{50} and 614±14 HV for $Ti_{37.5}$-$V_{12.5}$-Pt_{50}, Table 4-17. After SHT, the Vickers hardness slightly increased on the $Ti_{43.75}$-$V_{6.25}$-Pt_{50} alloy, but the hardness of the $Ti_{37.5}$-$V_{12.5}$-Pt_{50} was decreased. Although there was no significant improvement in hardness after SHT, the Vickers hardness values were still above that of the binary Ti-Pt.

Table 4-17: Macro Vickers hardness values of as-cast and solution heat treated Ti-V-Pt alloys.

Alloy	Macro Vickers hardness (VHN)
As-cast	
Ti_{50}-Pt_{50}	321±5
$Ti_{43.73}$-$V_{6.25}$-Pt_{50}	495±25
$Ti_{37.5}$-$V_{12.5}$-Pt_{50}	614±14
Solution heat-treated	
Ti_{50}-Pt_{50}	347±10
$Ti_{43.73}$-$V_{6.25}$-Pt_{50}	500±23
$Ti_{37.5}$-$V_{12.5}$-Pt_{50}	491±15

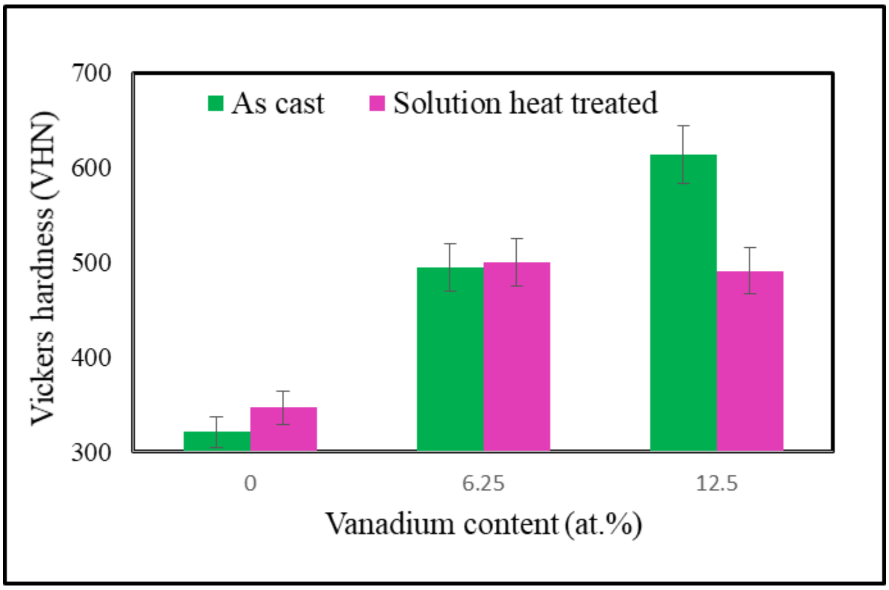

Figure 4.2.8: Macro Vickers hardness of Ti-V-Pt alloys as a function of V content after arc melting and SHT.

4.2.5. The effect of ternary alloying with V on the shape memory effect of Ti-Pt alloys

The shape memory strain and shape recovery ratio results of the Ti-V-Pt alloys at a constant applied strain of 5% are summarized in Table 4-18 and Figure 4.2.9. The partial substitution of Ti with 6.25 at.% V increased the shape memory strain and shape recovery ratio of Ti-Pt in the as-cast condition. However, the addition of 12.5 at.% V to the Ti-Pt slightly decreased the shape memory strain and shape recovery ratio in the as-cast condition. After SHT, binary Ti-Pt had the lowest shape memory strain and shape recovery ratio, indicating a significant improvement in the ε_{sme} and SRR with increasing V concentrations, Figure 4.2.9.

Table 4-18: Room temperature shape memory behaviour of Ti_{50}-Pt_{50} and Ti-V-Pt alloys at an applied strain of 5%.

Alloy	ε_{irr}	ε_{sme} (%)	SRR(%)
As-cast			
Ti_{50}-Pt_{50}	0.003	1.7	83.5
$Ti_{43.75}$-$V_{6.25}$-Pt_{50}	0.002	1.8	91.5
$Ti_{37.5}$-$V_{12.5}$- Pt_{50}	0.003	1.5	81.6
Solution heat treated			
Ti_{50}-Pt_{50}	0.02	0.8	31.2
$Ti_{43.75}$-$V_{6.25}$-Pt_{50}	0.01	1.2	57.5
$Ti_{37.5}$-$V_{12.5}$- Pt_{50}	0.01	1.7	66.8

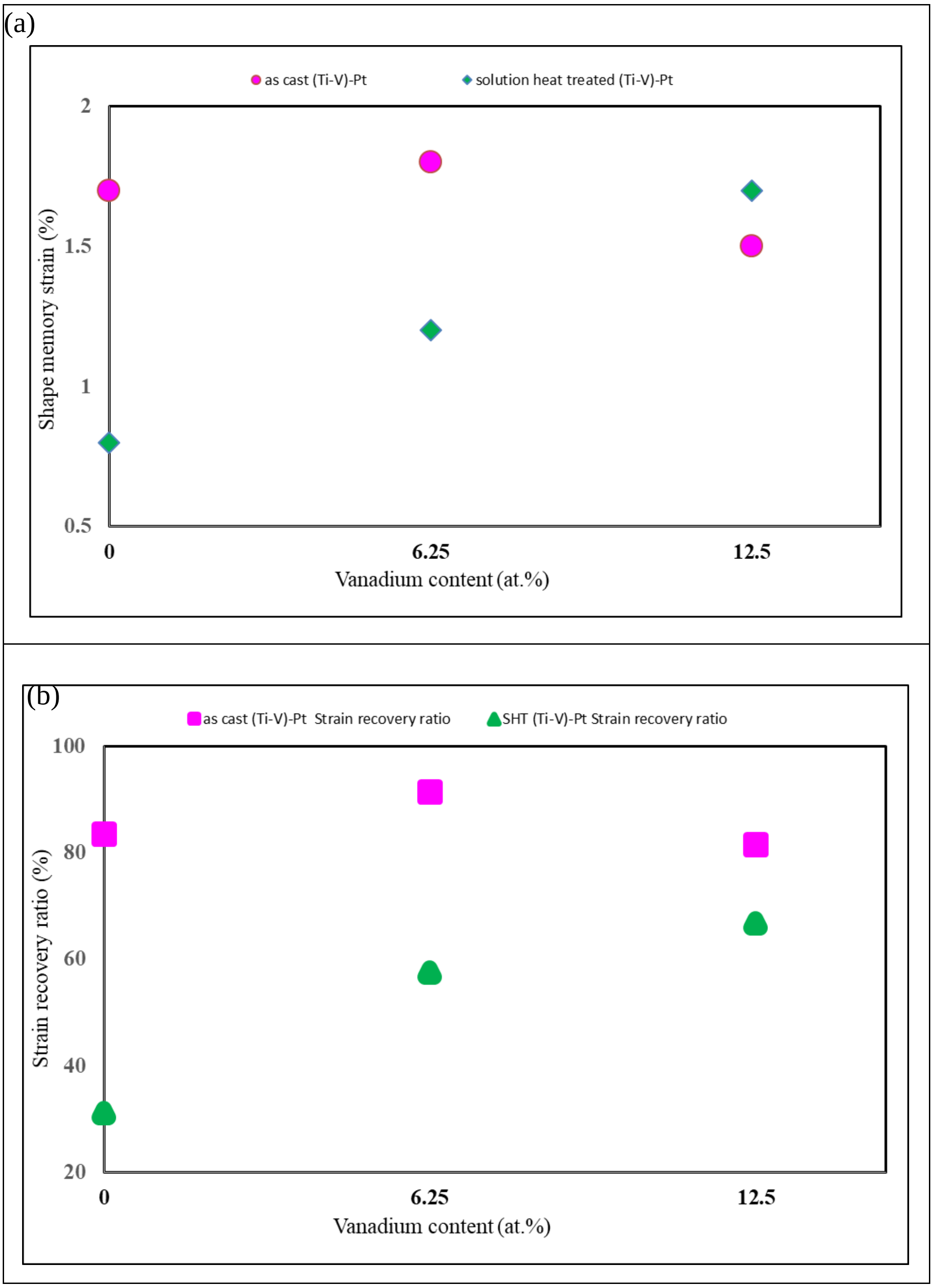

Figure 4.2.9: The effect of V content on the (a) shape memory strain and (b) strain recovery ratio of Ti-V-Pt alloys deformed up to an applied strain of 5%.

Shape memory properties were also investigated at applied strains that were greater than 5%. As a result, $Ti_{43.75}$-$V_{6.25}$-Pt_{50} was deformed at a compressive strain of 13.6% for the as-cast and solution heat treated conditions, while, $Ti_{37.5}$-Pt_{50}-$V_{12.5}$ was deformed at a compressive strain to 11.8% for the as-cast and solution heat treated conditions. The binary Ti-Pt was used for comparison; it was deformed at compressive strains of 15% for the as-cast and solution heat treated conditions. These compressive strains were obtained from Ti-V-Pt compressive stress-strain curves in Figure 4.2.7.

Figure 4.2.10 shows that the addition of V increased the SRR of Ti-Pt with the increasing V content in both the as-cast and solution heat-treated conditions. However, these shape recovery ratios were lower than those obtained at deformation strains of 5%, which was expected, since higher applied strains are associated with higher irrecoverable strains even after heating the alloys above the A_f temperature. The shape memory strain of Ti-Pt was significantly improved at applied strains greater than 5% with the addition of 6.25 at.% V in both the as-cast and solution heat treated conditions, indicating that at higher applied strains the (Ti,V)Pt martensite accommodated some strain. In the as-cast condition, the addition of 12.5 at.% V slightly decreased the shape memory strain of Ti-Pt. However, after SHT, ($Ti_{37.5}$-$V_{12.5}$)-$Pt_{37.5}$ exhibited better shape memory strain than binary Ti-Pt (1.1%). This was lower than what was obtained at an applied compressive strain of 5%, which was expected, since higher irrecoverable strains were obtained with the increased applied strain, Table 4-18 and 4-19.

Table 4-19: Shape memory effect calculations of Ti_{50}-Pt_{50}, $Ti_{43.75}$-$V_{6.25}$-Pt_{50} and $Ti_{37.5}$-$V_{12.5}$-Pt_{50} alloys at applied strains greater than 5%.

Alloy	ε_{irr}	ε_{sme}(%)	SRR (%)
	As-cast		
Ti_{50}-Pt_{50}	0.09	1.7	16.5
$Ti_{43.75}$-$V_{6.25}$- Pt_{50}	0.06	2.0	24.1
$Ti_{37.5}$- $V_{12.5}$-Pt_{50}	0.07	1.4	17.3
	Solution heat treated		
Ti_{50}-Pt_{50}	0.09	1.1	11.1
$Ti_{43.75}$-$V_{6.25}$- Pt_{50}	0.06	1.7	21.0
$Ti_{37.5}$- $V_{12.5}$-Pt_{50}	0.06	1.3	17.6

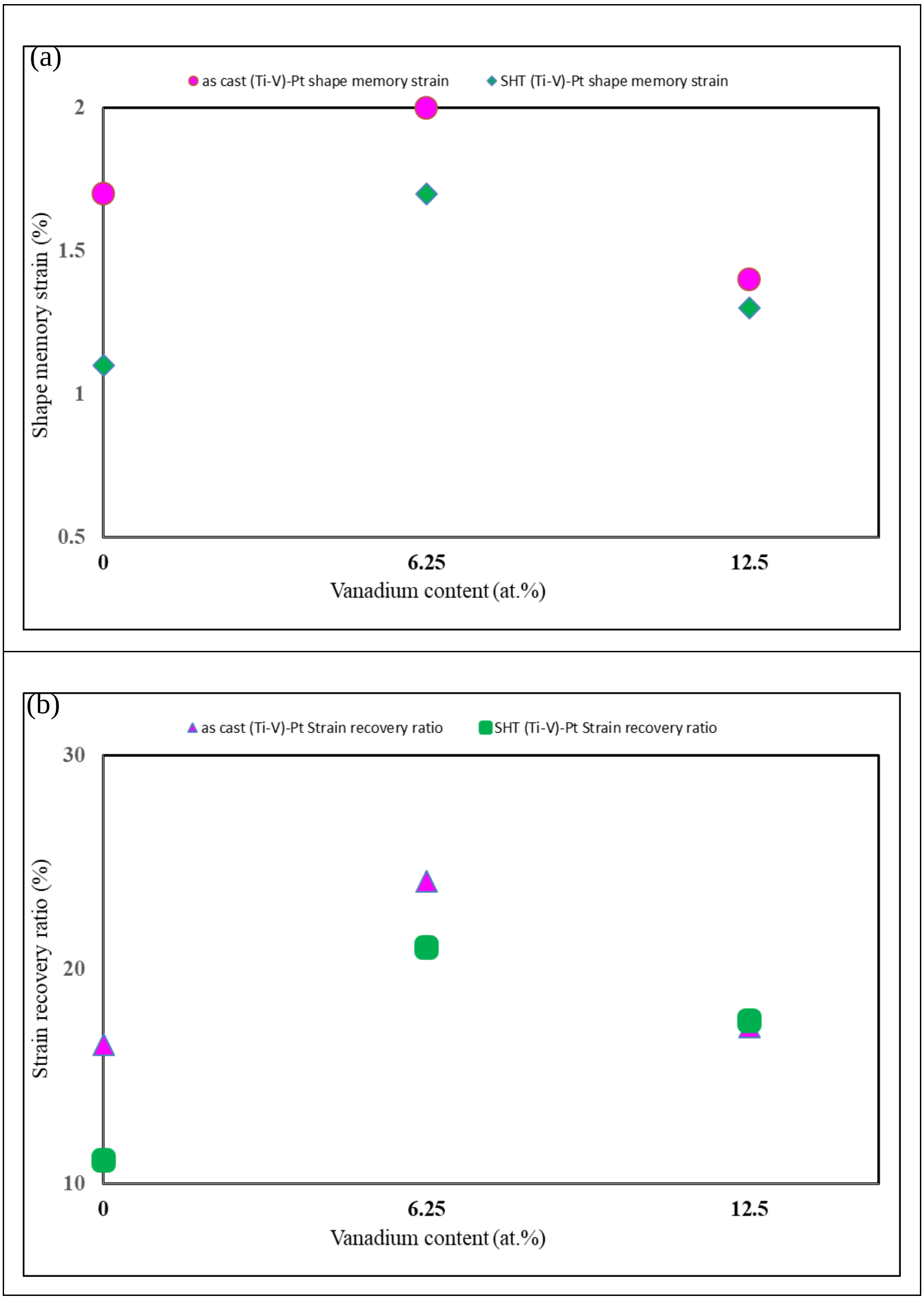

Figure 4.2.10: The effect of V content on the (a) shape memory strain and (b) strain recovery ratio of Ti-V-Pt alloys at applied strains greater than 5%.

CHAPTER 5: Discussion

5. Discussion

This chapter is divided into six main sections and these are:

- Effects of ternary alloying with V on microstructural evolution of Ti-Pt alloy in the as-cast and solution heat treated conditions.
- The effect of ternary alloying with V on the crystal structure of Ti-Pt.
- The effect of ternary alloying with V on the phase transformation of Ti-Pt.
- The effect of ternary alloying with V on the mechanical properties of Ti-Pt.
- The effect of ternary alloying on the shape memory behaviour of Ti-Pt.
- Summary on the effect of ternary alloying with V on the shape memory properties of the Ti-Pt alloy.

5.1. Effects of ternary alloying with V on microstructural evolution of Ti-Pt alloys

Microstructural studies of Ti-Pt after ternary alloying with varying contents of V (0-12.5 at.%) were carried out in the as-cast and solution heat treated conditions. The binary Ti-Pt alloy was used for comparison. Microstructural evolution studies were done in order to understand the solidification sequence of the Ti-Pt alloy after substitution of either Pt or Ti with V in the as-cast and solution heat-treated conditions. The microstructures of the Ti-Pt-V and Ti-V-Pt alloys had multiple phases, indicating that the alloys followed different solidification sequences during production. Binary Ti-Pt comprised TiPt, Ti_3Pt and Ti_5Pt_3 phases, while the partial substitution of Pt with V resulted in the formation of Ti(Pt,V), $(Ti,V)_3Pt$, $Ti_4(Pt,V)_3$, $Pt(V,Ti)_3$, $Ti_2(Ti,V)O$ and $(TiO)_3Pt$ phases, and the partial substitution of Ti with V had (Ti,V)Pt, Ti_3Pt and TiO phases. These resultant phases caused different solidification sequences during solidification. In addition, after SHT, the phase boundaries of TiPt narrowed at lower temperatures, so there was more of the other phases.

The microstructures showed that ternary alloying with V influences the microstructural evolution of the Ti-Pt alloy in the as-cast and solution heat treated conditions. The binary Ti-Pt and partial substitution of either Ti or Pt with V exhibited variations in the microstructures. For purposes of discussion on the effect of ternary alloying with V on microstructural evolution, each was discussed separately to avoid confusion. The discussion proceeded in the following order:

- Microstructural evolution of the binary Ti-Pt alloy
- Effect of substituting Pt with V on the microstructural evolution of the Ti-Pt alloy

- Effect of substituting Ti with V on the microstructural evolution of the Ti-Pt alloy

5.1.1. Microstructural evolution of binary Ti-Pt alloy

The overall composition of the binary Ti-Pt was Ti-rich in both the as-cast and solution heat treated conditions, however, the composition was still within the TiPt single-phase region of the Ti-Pt phase diagram, indicating a concentration of point defects such as Ti antisites and Pt vacancies. Biggs *et al.* [37] studied the microstructure, martensitic transformation and mechanical properties of binary the Ti-Pt alloy. They reported that the presence of point defects affected the martensitic transformation behaviour and mechanical properties of the Ti-Pt alloy.

The binary Ti_{50}-Pt_{50} alloy followed this solidification sequence during cooling: above the eutectic temperature, the alloy was comprised of liquid (L) and β-TiPt dendrites (L → β-TiPt). At the, eutectic temperature, the remaining liquid containing all the contaminants (including oxygen) transformed to Ti_3Pt and β-TiPt phase in the interdendritic regions (L → β-TiPt + Ti_3Pt). At lower temperatures, below the martensitic transformation temperature, the β-TiPt phase in the dendrites and interdendritic regions transformed to α-TiPt (β-Ti-Pt → α-TiPt).

During SHT of the as-cast structure at 1250 ^{o}C, the microstructure was composed of a β-TiPt matrix with Ti_3Pt and Ti_5Pt_3 phases. During SHT, there was an interdiffusion between TiPt and Ti_3Pt to form the Ti_5Pt_3 phase, which was stabilized by the presence of oxygen in the Ti-Pt system. The β-TiPt dendrites transformed to α-TiPt after quenching below the martensitic transformation temperature. The Ti_5Pt_3 phase does not appear on the Ti-Pt phase diagram in Figure 2.5.3, but, Biggs [80] observed a similar phase in heat-treated Ti-(30-61)Pt samples using XRD, SEM and microprobe, where it was predicted to be a distorted Ti_3Pt phase because it was formed as a consequence of the presence of oxygen in the Ti-Pt system. Tello [25] confirmed the presence of the Ti_5Pt_3 phase in the as-cast and solution heat treated Ti-44Pt and Ti-42Pt alloys using SEM and TEM. This was attributed to the presence of interstitial atoms, such as oxygen, which allows its stabilization. Oxygen could have been picked up in the starting elemental powers or during arc-melting or thermal processing of the alloys [25].

5.1.2. Effect of substituting Pt with V on the microstructural evolution of Ti-Pt alloy

Figures 4.1.2 to 4.1.4 reveal that the partial substitution of Pt with V resulted in multiple phases with the amount of martensitic Ti(Pt,V) phase decreasing with increasing V content. With increasing V content, the volume fraction of Ti-rich phases also increased. The microstructures revealed that replacing Pt with V resulted in a composition that was within in a three-phase region and not in a TiPt single-phase region.

As mentioned earlier, the partial ubstitution of Pt with V followed a similar solidification path as the binary Ti-Pt alloy, however the Ti_3Pt and β-TiPt formed from the remaining liquid at the eutectic temperature ($L \rightarrow \beta\text{-TiPt} + Ti_3Pt$) reacted peritectoidally to form the Ti_4Pt_3 phase at 1205 °C ($\beta\text{-TiPt} + Ti_3Pt \rightarrow Ti_4Pt_3$). This resulted in the narrowing of the Ti(Pt,V) at lower temperatures and an increased volume fraction of the $(Ti,V)_3Pt$, $Ti_5(Pt,V)_3$, $Ti_4(Pt,V)_3$, $Pt(V,Ti)_3$ phases with increasing V content. The difference between $Pt(V,Ti)_3$ and Ti_3Pt phase was the amount of V, with the former having higher amounts of V. The formation of Ti_5Pt_3 during solidification was attributed to the enrichment of the remaining liquid with solute and impurity atoms, such as oxygen, which stabilizes this phase [25]. The SHT of the as-cast structures increased the volume fraction of the other phases with increasing V content while the amount of the Ti(Pt,V) phase decreased. The decreased amount of the Ti(Pt,V) phase was attributed to the new alloy compositions that lie in three-phase regions with increasing V content, Figure 5.1.1.

The isothermal section at 1250 °C in Figure 5.1.1 together with the microstructures of the Ti_{50}-$Pt_{43.75}$-$V_{6.25}$ alloy had a composition that lies in the a single field TiPt phase region, numbered point 1. The addition of 12.5 at.% V resulted in alloy compositions that laid in three- phase region between TiPt, Ti_4Pt_3 and Ti_3Pt phase region, Figure 5.1.1.

The $Ti_2(Pt,V)O$ phase in the Ti_{50}-$Pt_{31.75}$-$V_{18.25}$ alloy was a distorted Ti_3Pt phase that was stabilized by the absorption of high oxygen content during arc melting. The isothermal section at 1250 °C confirmed that Pt substitution with 18.25 at.% V resulted in an alloy composition that lies in a three-phase region between TiPt, Ti_3Pt and Ti_4Pt_3 but much closer to the Ti_3Pt phase region, Figure 5.1.1. The amount of Ti(Pt,V) phase, which is a prerequisite for shape memory behaviour, had drastically decreased with ternary alloying of Ti-Pt with 18.25 at.% V. Therefore, this alloy was not investigated further in this study.

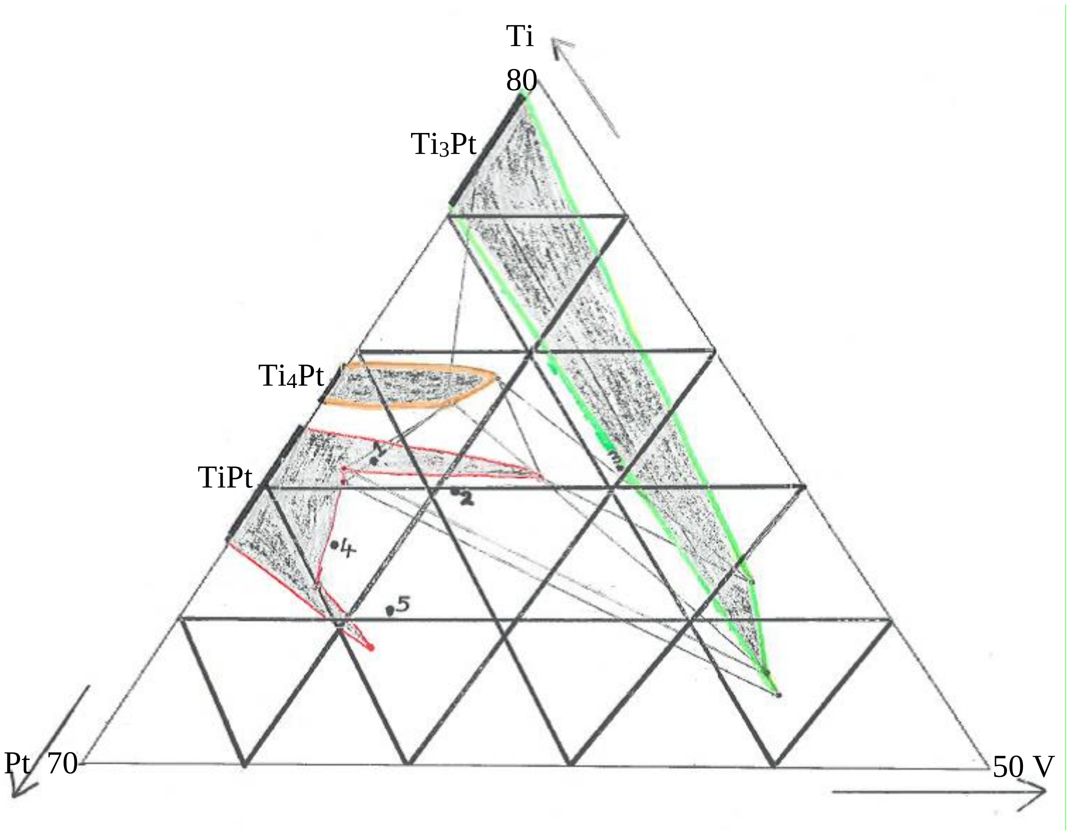

Figure 5.1.1: Ternary phase diagram of Ti-Pt-V and Ti-V-Pt alloys at 1250°C after soaking for 72 hrs to achieve equilibrium conditions and thereafter quenched vigorously in ice water: showing SEM-EDX compositions of 1- Ti_{50}-$Pt_{43.75}$-$V_{6.25}$, 2- Ti_{50}-$Pt_{37.5}$-$V_{12.5}$, 3- Ti_{50}-$Pt_{31.75}$-$V_{18.25}$, 4- $Ti_{43.75}$-$V_{6.25}$-Pt_{50} and 5- $Ti_{37.5}$-$V_{12.5}$-Pt_{50} alloy (at.%).

5.1.3. Effect of substituting Ti with V on the microstructural evolution of Ti-Pt alloy

The partial substitution of Ti with 6.25 and 12.5 at.% V followed a similar solidification sequence of binary Ti-Pt alloy, with the formation of (Ti,V)Pt as a major phase, Ti_3Pt and TiO phases in the interdendritic regions. Solution heat treatment resulted in the elimination of interdendritic regions, with (Ti,V)Pt and TiO phases. The amount of TiO and Ti_3Pt phases increased with increasing V content due to the increased proneness of the alloy to oxidation with increasing V content. The isothermal section at 1250°C show that the partial substitution of Ti with V (points 4 and 5) resulted in a single phase TiPt region, Figure 5.1.1.

5.2. The effect of ternary alloying with V on the crystal structure of Ti-Pt alloy

The XRD measurements of Ti-Pt-V and Ti-V-Pt alloys were carried out in order to confirm the phases observed by the SEM-EDX. Most of the diffraction peaks were identified as the B19 martensitic structure for all compositions and no residual B2 phase was detected, indicating that an austenite to martensite transformation occurred with the addition of V.

The broadening and disapperance of some Ti(Pt,V) diffraction peaks in Ti_{50}-$Pt_{37.5}$-$V_{12.5}$ alloy in Figure 4.1.5 indicated some significant lattice distortions of the B19 martensite phase, showing that there were small volume fractions of B19 martensite phase in the alloy. The $Ti_4(Pt,V)_3$ and Ti_5Pt_3 phase peaks were prominent after SHT in the Ti-(Pt-V) alloys due to the increased amount of these phases after SHT. In addition, the Ti_3Pt phase was found to contain varying amounts of oxygen, which was possibly from the starting powders or oxygen pickup during processing.

The lattice parameters of the B19 crystal structure for all compositions was determined using the Rietvield analysis in Maud software. The lattice parameters of the binary TiPt were determined to be a = 4.636, b = 2.794 and c = 4.929 nm. The lattice parameters for the B19 martensitic structure reported in different publications are within the range of the values obtained in this study, confirming the consistency of the results in this study with most of the previously reported results in the literature [19,22,23,34,55,66]. The addition of V to Ti-Pt shifted the diffraction peaks to slightly higher 2θ angles, indicating a reduction of the lattice parameters of the unit cell. Such behaviour was expected since V with a small atomic radius of 0.134 nm was replacing either Pt or Ti with a large atomic radius of 0.139 nm and 0.147 nm. A similar finding has been reported in other SMA system where a small atomic radius atom replaced a large atomic radius atom [22,81]. After SHT, diffraction peaks shifted to slightly lower 2θ angles, indicating an increase in the lattice parameters. The increase in the lattice parameters was attributed to ice water quenching of the alloys from high temperatures after SHT, resulting in larger B19 TiPt lattice parameters derived from larger parameters of high temperature B2 crystal structure. Also, SEM-EDX revealed that less V atoms went into solution to form the TiPt phase during SHT, so the lattice parameters would increase since less V atoms with a small radius were going into solution However, a decrease in lattice parameters of the unit cell with increasing V content was maintained after SHT.

Yamabe-Mitarai *et al.* [66] studied high temperature XRD analysis of equiatomic Ti-Pt. They reported that the transformation from the B19 to B2 phase takes place when the lattice parameter ratios a/b and c/b are close to 1.414 or less, meaning that lattice parameter ratios greater than 1.414 are associated with a B2 to B19 transformation. Figures 4.1.6 and 4.2.4 show that lattice parameter ratios a/b and c/b were all greater than 1.4.14, indicating that the structure of the B19 martensite phase remained orthorhombic in all alloy compositions studied.

5.3. The effect of ternary alloying with V on phase transformation in Ti-Pt

The binary Ti-Pt, which acted as a benchmark, exhibited double transformation peaks during the forward and reverse transformations, indicating the existence of a multistage austenite to martensite transformation. However, the addition of V resulted in the presence of a single transformation peak during forward and reverse transformation for all alloys, indicating the existence of a single stage B2 to B19 transformation. This transformation behaviour had different transformation temperatures of Ti-Pt-V and Ti-V-Pt alloys. In addition, the thermal hysteresis (ΔT) of Ti-Pt-V and Ti-V-Pt alloys samples increased with increasing V content. However, there was no significant change in transformation temperatures after subjecting the alloys to SHT. This was attributed to the not significant change in composition of TiPt phase after SHT.

The composition of the TiPt phase was found to be different for each alloy due to the partial substitution of either Pt or Ti with varying V content. This showed different effects of ternary alloying with V and resulted in variations in the transformation temperatures, thermal hysteresis and latent heats of formation of the Ti-Pt-V and Ti-V-Pt alloys in both the as-cast and solution heat treated conditions. The binary Ti-Pt and substitution of either Ti or Pt with V exhibited different martensitic transformation behaviours. The effects of ternary alloying with V on the phase transformation in Ti-Pt-V alloys are discussed in Sections 5.3.1, 5.3.2 and 5.3.3.

5.3.1. Phase transformation in binary Ti-Pt alloy

In Figure 4.1.7, the second peak during the forward transformation in the binary Ti-Pt alloy could be associated with the remaining austenite transforming to a long period microtwin (LP) structure [65]. This behaviour is quite common in binary Ti-Pt alloys and was attributed to slight variations in composition or stress in the sample leading to a mixture of B19 and LP structures, as observed by Rotaru *et al* using TEM [65,82]. Rotaru e*t al* [65] did a study of the LP structure in binary Ti-Pt using TEM and SEM-EDX where they reported that the LP phase is a low energy structure, which showed no composition difference between the LP and B19 TiPt phase. The formation of double peak transformation can also be caused by local stress fields around the precipitates, local composition inhomogeneity around the precipitates and the atmosphere during production and heat treatment of the alloys causing a slightly inhomogeneous system in which a small portion of the material transforms into a structure other than the expected B19 martensite [65,82]. Biggs *et al.* [64] associated the presence of double peak transformation with the formation of intermediate phases.

There was no significant change in transformation temperatures of the TiPt phase after SHT, except a slight decrease in the transformation temperatures. This was explained using SEM-EDX results, where the alloy was off-stoichiometric (Ti-rich) in both the as-cast and solution heat treated conditions, indicating the presence of Ti antisites and Pt vacancies. According to Biggs *et al* [64] and Donkersloot *et al* [53], highest transformation temperatures occur at the point of stoichiometry with 50 at.% Pt and deviations from stoichiometry above 50 at.% Pt reduce the transformation temperatures. In this study, the Ti-Pt alloy consisted of higher Pt amounts in the solution heat treated condition i.e. 50.80±0.7 at.% versus 49.53±1.7 at.% for the as-cast condition, indicating a deviation of the Pt amounts from stoichiometry after SHT, hence, the resultant decrease in transformation temperatures. In addition, based on the SEM microstructures, the volume fraction of other phase particles (Ti_3Pt and Ti_5Pt_3) was increased after SHT, and might have contributed to the reduction of the transformation temperatures. The other phases formed during production or SHT constrained the martensite growth and increased the frictional force needed to overcome the driving force required for martensite nucleation [83]. This resulted in a decrease of the martensitic transformation temperatures.

The thermal hysteresis of the first and second transformation cycles calculated using the formula [47], i.e. $\Delta T = A_f - M_s$ was 59.5 and 60.7 ^oC in the as-cast condition and 58.6 and 59.3 ^oC in the solution heat treated condition, which was higher than previously reported for Ti-Pt alloys [65]. This could be attributed to the fact that the alloy was non-stoichiometric, resulting in point defects such as antisite and vacancies [37].

5.3.2. The effect of replacing Pt with V on the phase transformation in Ti-Pt alloy

The addition of V when replacing Pt decreased the transformation temperatures of Ti-Pt with the increasing V content, Figure 4.1.8. The decrease in transformation temperatures of Ti-Pt with increasing V content was attributed to the other phases and concentration of valence electrons (C_v). Based on the SEM-EDX results, the addition of V resulted in microstructures with an increased amount of the other phases compared to the binary Ti-Pt. During nucleation of the martensite, an additional driving force is required to overcome the non-chemical energy barrier that is affected by the stored elastic energy and frictional work that can be estimated by considering microstructural factors. The presence of other phases formed in these alloys during casting, restricted martensite growth and increased the frictional work, thereby, decreasing the transformation temperatures of the alloy [83]. In this study, it was found that the volume fraction of the other phases increased with increasing V content, thus further decreasing the transformation temperatures.

The decrease of transformation temperatures with increasing V content was also explained by using the dependence of transformation temperature on the valence electrons per atom number

(e_v/a) and concentration of valence electrons (C_v) with respect to the change in composition [70]. The binary as cast $Ti_{51.2}Pt_{48.8}$ had an (e_v/a) = 6.93 and (C_v) = 0.140. The partial substitution of Pt by 6.25 at.% vanadium resulted in (e_v/a) = 6.685 and (C_v) = 0.143, where (C_v) was higher than the binary $Ti_{51.2}$-$Pt_{48.8}$. This corresponded to a reduction of transformation temperatures with the addition of V. The addition of 12.5 at.% had (e_v/a) = 6.695 and (C_v) = 0.144, where (C_v) had increased further. The latter resulted in a further degrading of the transformation temperatures due to the formation of stronger bonds in the B2 phase that are more difficult to break, and supressed the nucleation of B19 martensite phase.

This decrease in transformation temperatures was in agreement with first principles calculations that predicted the reduction of transformation temperatures with the addition of V being due to the stability of the B2 cubic phase that increases the shear modulus C' with the increase of V concentrations [21,77]. Therefore, the increasing concentration of valence electrons with increasing V content stabilized the high temperature B2 phase, thereby suppressing the formation of B19 martensite and thus decreasing the transformation temperatures.

Increasing of the thermal hysteresis (ΔT) with increasing V content was likely to occur due to the increasing volume fraction of the other phases, such as Ti_3Pt, Ti_4Pt_3, $Pt(V,Ti)_3$ and Ti_5Pt_3, with increasing V contents. Evirgen *et al* [84] did a study on the transformation thermal hysteresis of Ni-rich Ni-Ti-Zr and Ni-Ti-Hf showing the B2 to B19' martensitic transformation as a function of the microstructure. They reported that the presence of other phases restricts the martensite growth within the space between the other phases. Therefore more energy is dissipated during the martensitic transformation in order to form a large number of constrained martensite variants, leading to an increased thermal hysteresis [84]. In this study, the larger amounts of other phases with increasing V content could have changed the martensite morphology, resulting in the relatively large volume changes and energy dissipation during the martensitic transformation and the thermal hysteresis was increased. Based on the SEM micrographs, the volume fraction of the other phases had increased after SHT, hence the increase in the thermal hysteresis with increasing V content. The widening of the thermal hysteresis could be an advantage for vibration and damping applications that would allow a large temperature range over which elevated damping might occur [9,48]. However large hysteresis could be a disadvantage for actuator applications that require a narrow hysteresis [9].

The latent heat of formation (Δ_H) decreased with increasing V content, indicating a decreasing volume fraction of the transforming Ti(Pt,V) phase with increasing V content. The increasing volume fraction of the other phases with increasing V content might also have contributed to the reduction of Δ_H by increasing the stored elastic energy during transformation through the introduction of elastic constraints [85].

Lastly, the decrease in transformation temperatures, latent heats of transformation and widening of transformation hysteresis with increasing V content can be partly addressed using Humer Rothery rules of alloying that describes the solubility limit of V in Pt [69]. The mismatch in atomic radius between Pt and V was less than 15%, which is the only rule regarding solubility that it matches, meaning partial solubility can be achieved. The crystal structure of the two elements was different. Hume-Rothery rule of alloying [69]: (a) maximum solubility can be achieved when the solute and solvent have similar valence electrons. The valence electrons of vanadium and platinum calculated using the *d* and *s* orbitals were 5 and 10, which is far apart from each other, meaning that the tendency of Pt to dissolve V is very low. (b) The electronegativity difference being close to zero allows maximum solubility. The electronegativity difference between V (1.63) and Pt (2.28) equated to 0.65. However, if the same rules are applied when V is substituting for Ti, better partial solubility can be achieved between Ti and V because the valence electrons of Ti (4) and V(5) are not far apart compared to Pt and V. In addition, the electronegativity difference between Ti and V is 0.09. Therefore, V would prefer to occupy Ti sites rather than Pt sites because of better partial solubility between Ti and V.

This was in contradiction to what Bozzolo *et al.* [12] found when modelling the site occupancy of a large number of ternary additions to Ti-Pd and Ti-Pt alloys using computational modelling. They reported that V has no site preference for Ti or Pt during alloying of Ti-Pt alloys. However, from SEM-EDX and DSC results, it can be deduced that V has a site preference for Ti, since the concentration of Ti rich phases increased with the increasing additions of V content in the alloy

As a result, the fact that the transformation temperatures decrease with increasing V concentrations could be due to the formation of antisite defects by V atoms on Pt lattice positions. Not all of the V goes to Pt, some of the V split to Ti due to close valence electrons. The split of V to Ti stabilizes the B2 phase due to structural relaxation around the sites. Frenzel *et al.* [86] studied the effect of alloy composition on the martensitic start temperature and latent heat of formation in Ni-Ti based SMAs. They reported that antisite defects in Ni-Ti-Cu and Ni-Ti-Cr alloys are accompanied by large local displacements of atoms leading to changes in the atomic coordination surrounding the Cu/Cr-antisite atoms [86]. The displacement of the atoms in the surroundings of the Cr/Cu-antisites was associated with a significant energy gain that lead to the stabilization of the B2 phase structure and thus supress the formation of the martensite phase [86]. Further verification using *ab initio* density functional theory (DFT) calculations is needed to confirm if Ti-Pt-V follows a similar mechanism.

5.3.3. The effect of replacing Ti with V on the phase transformation in Ti-Pt alloy

In Figure 4.2.5, the replacement of Ti with V increased the transformation temperatures of Ti-Pt with increasing V content. This was due to the amounts of Pt closer to 50 at.% observed during SEM-EDX analysis, valence electrons per atom of the alloy samples and site preference and occupancy of V using the chemical affinity of V towards Ti and Pt and Hume-Rothery rules of alloying. These mechanisms will be discussed in detail.

According to Biggs *et al.* [37] and Donkersloot *et al.* [53], the highest M_s and A_s temperatures are attained at the stoichiometric compositions with 50 at.% Pt. The addition of V when substituting for Ti had high amounts of Pt that were very close to 50 at.% compared to the binary Ti-Pt in the as-cast and solution heat treated conditions. Therefore, the high content of Pt close to 50 at.% might have contributed to the high transformation temperatures.

Normally, higher valence electrons per atom (e_v/a) means high bond strength and, therefore, it was expected that the transformation temperatures would decrease. However, the addition of V when replacing Ti resulted in higher valence electrons per atom (e_v/a) and higher transformation temperatures than binary Ti-Pt. However, this did not result in any significant decrease in transformation temperatures. Zarinejad *et al.* [70] reported that for $6.8< e_v/a <7.2$, the M_s and A_s temperatures were scattered and did not show any clear trend with respect to e_v/a. The addition of 6.25 and 12.5 at.% V had e_v/a values of 7.06 and 7.10, which are within the range of 6.8 and 7.2, where there seems to be no clear trend and this is in agreement with what was observed in this study.

According to Zarinejad *et al.* [70], if an alloying element has strong affinity to Ti by having a large negative formation enthalpy but has a weak affinity to Ni , this alloying element tends to substitute for Ni as it has similar chemical properties as Ni. The latter, affects the site preference and occupancy of the ternary element. In this study, the enthalpy of formation between Ti-Pt was ΔH = -74 kJ/mol, between Ti-V was ΔH = -2 kJ/mol and between Pt-V was = -45 kJ/mol [83]. This indicated that V has a stronger affinity to Pt and a weak chemical affinity to Ti. Therefore, vanadium tends to substitute for Ti. The latter means that V has a site preference and occupancy of Ti, hence the resultant increase in transformation temperatures more than when V was replacing Pt. This would result in a decrease in the shear modulus of the B2 crystal structure, thereby promoting the formation of B19 martensite phase.

Hume-Rothery rules of alloying show that Ti and V exhibit better partial solid solubility than Pt because their valence electrons are close to each other and the electronegativity difference between Ti and V is lower than that for Pt and V. As a result, the transformation temperatures might have increased due to the improved partial solid solubility between Ti and V. This means that the partial substitution of Ti with V destabilized the B2 phase and promoted the formation of B19 martensite.

The SHT of $Ti_{43.75}$-$V_{6.25}$-Pt_{50} alloy resulted in higher transformation temperatures due to the low volume fraction of the other phases on the microstructures after SHT. The addition of 12.5 at.% V showed decreased transformation temperatures after SHT. This could be due to the enhancement and growth of the oxide phase on the microstructures after SHT.

The widening of the thermal hysteresis with increasing V contents was attributed to the existence of other phases (Ti_3Pt and TiO), as explained in the previous section. However, after SHT, the thermal hysteresis was decreased but was still above that of the binary Ti-Pt. This was attributed to the elimination of some interdendritic phases, such as Ti_3Pt, after SHT, indicating the decreasing resistance to martensite transformation due to the low volume fraction of the other phases that could restrict martensite growth.

The addition of V when substituting for Ti also resulted in M_s temperatures that were slightly higher than A_s temperatures. This behaviour was also reported by Donkersloot *et al.* [55] in the binary Ti-Pt alloy and it was speculated that this might have been caused by the formation of intermediate phases between the B2 and B19. Therefore, further analysis is needed to confirm if the (Ti,V) Pt martensite phase transformation follows a similar mechanism.

5.4. The effect of ternary alloying with V on the mechanical properties of Ti-Pt alloys

In general, the SMAs exhibit a double yielding behaviour in the martensite phase [23,87,88]. The first yield point is caused by reorientation of martensite variants and is usually called the detwinning stress. During the first yielding point, the detwinning of twinned martensite takes place by an inelastic rearrangement of atoms due to the deformation caused by the applied stress [9,88]. With further deformation, the twinned martensite plates disappear by detwinning and lattice distortions initiate at the second yielding point. The second yield point indicates critical stress for slip; that is where plastic deformation occurs. In this study, the binary Ti-Pt alloy exhibited this behaviour with a detwinning stress and 0.2 % yield strength of 513±33 and 1478±24 MPa, which was within the range of the values obtained by Yamabe-Mitarai *et al.* [87], confirming the results of this study to be consistent with previously reported in the literature.

The observed increase in the detwinning stress and yield strength of binary Ti-Pt alloy after SHT was in agreement with the Vickers hardness results, where the Vickers hardness of Ti-Pt had increased after SHT. According to Biggs *et al.* [37], the hardness of TiPt martensite is low with around 50 at.% Pt, but increases rapidly as the stoichiometry deviates on either side of the ideal stoichiometry. They attributed the increase in hardness within the range of single-phase homogeneity but off-stoichiometry to the variation of point defects such as vacancies or antisite defects across the range of stoichiometric TiPt. In this study during SEM analysis, TiPt phase was Ti-rich in both the as-cast and solution heat treated conditions, meaning that there is a variation of Ti antisites and Pt vacancies, which could significantly play a role in increasing the yield strength and hardness. Therefore, the concentration of Ti antisites and Pt vacancies might have increased during SHT at high temperatures which were retained by quenching, resulting in higher yield strength values. The increased volume fraction of Ti anitisites after SHT might have contributed to the lowering of the plastic strain by restricting dislocation mobility.

In addition, the increased amounts of the other phases (Ti_3Pt and Ti_5Pt_3) after SHT might have contributed to the higher strength of the alloy through the precipitation strengthening mechanism. These other phases impeded the movement of dislocations, thereby requiring high stresses for deformation to take place. The latter resulted in high stresses accommodating low plastic strains.

The addition of V eliminated the typical yielding behaviour of binary TiPt, and exhibited only one inflection point corresponding to a single yielding behaviour due to the occurrence of simultaneous slip deformation along with the martensite reorientation process. Yamabe-Mitarai *et al.* [20] reported this behaviour in Ti-Pt and Ti-Pt-Ir alloys during the investigation of the detwinning stress and yield strength after deformation strains of 20%. They mentioned that such behavior indicates that the critical stress for slip was lower than the detwinning stress and, therefore dislocations could easily move. According to Hong Wan *et al.* [88], the occurrence of a single yielding point in Ni-Ti-Hf-Zr alloy was attributed to the formation of additional internal twins inside the twinned martensite plates. During deformation, the internal twins underwent detwinning by reorientation of martensite plates at the yielding point, followed by plastic deformation without the second yield point, leading to a substantially reduced plastic strain. It was also mentioned that the formation of more internal twins inside the martensite plates contributed to the high yield strength [88]. Therefore, the Ti-Pt-V and Ti-V-Pt alloys could also be following a similar mechanism, but further TEM is required to confirm this.

The significant increase in yield strength and hardness of Ti-Pt with increasing V contents was due to the solid solution and precipitation strengthening of the alloy with increasing V contents. Yamabe-Mitarai *et al.* [20,65,85] and Wadood *et al.* [19] observed a similar behavior where alloying of Ti-Pt with Zr, Hf and Ru increased the yield strength through solid solution and precipitation strengthening.

Solid solution strengthening can be controlled by the following factors: concentration of solute atoms, shear modulus of solute atoms, size of solute atoms and valency of solute atoms. In the current study where V was substituting for Pt, the amount of V was varied between 0 and 12.5 at.%, the atomic radius of V (0.134 nm) was smaller than that of Pt (0.139 nm) which introduces tensile lattice strains. The shear modulus of V (47 GPa) was smaller than that of Pt (61 GPa) and the valency of V (5) was lower than for Pt (10). The most controlling factor to solid solution strengthening of Ti-Pt-V was the concentration of V solute atoms. For example, based on SEM-EDX results, with the partial substitution of Pt with 6.25 at.% V, only 4.5 at.% V went into solution to form Ti(Pt,V), resulting in solid solution strengthening of the TiPt phase. When V was added as a solute atom, local stress fields were formed which interact with the mobile dislocations, restricting their mobility. Dislocations piled up, multiplied during loading, and further restricted each other from moving; resulting in a higher work hardening rate i.e. the addition of vanadium increased the work hardening rate by restricting dislocation mobility [76,84].

Precipitation strengthening also contributed to further strengthening of the Ti-Pt-V alloys through the formation of $(Ti,V)_3Pt$, $Pt(V,Ti)_3$ and $Ti_4(Pt,V)_3$ phases [16,18,88]. The volume fraction of the other phases increased with increasing V content and these phases act as barriers to dislocation mobility and, therefore, higher stresses were required to move the dislocations, resulting in higher yield strength and hardness.

After SHT of Ti-Pt-V alloys, the yield strength and hardness increased to higher values of 1589±65 and 1849±164 MPa for Ti_{50}-$Pt_{43.75}$-$V_{6.25}$ and Ti_{50}-$Pt_{37.5}$-$V_{12.5}$ respectively. The increase was attributed to the increased volume fraction of the other phases. The noted decrease in plastic strain with increasing V content was due to the increased immobility of dislocations that restricted deformation from taking place. This means that the ductility of Ti-Pt-V was degraded with increasing V concentrations.

The yield strength and hardness of the Ti-V-Pt alloys had decreased after SHT, Figures 4.2.7 and 4.2.8. This was attributed to the coarsening of the other phase particles during SHT, Figure 4.2.2. Coarsening of particles reduces the effective pinning effect of particles, allowing dislocations to move easier than in the as-cast condition, resulting in decreased yield strength [89]. The decrease in yield strength could result in more ductility than that of the as-cast condition. However, the latter could not be determined due to the maximum load restriction.

According to Figures 4.1.10 and 4.2.7, the binary Ti-Pt alloy exhibited the biggest area under the stress-strain curve, meaning it absorbed more energy than the rest of the alloys during deformation. It means the alloy was more ductile than the rest of the alloys in the study.

5.5. The effect of ternary alloying with V on the shape memory properties of Ti-Pt alloys

The shape memory strain and shape recovery ratio of the binary Ti-Pt alloy was not improved after SHT, Table 10 and Figure 4.1.13. According to Yamabe-Mitarai *et al.* [20], shape recovery of Ti-Pt is improved when the yield stress of the martensite phase becomes high to suppress plastic deformation and the detwinning stress becomes small to move the martensite variants easily. It means that higher shape recovery is obtained with a small ratio of the detwinning stress (σ_dt) and yield stress (σ_y), i.e. when σ_dt/ σ_y becomes small, shape recovery is expected to be high since it allows the TiPt martensite matrix to accommodate the strain by detwinning and reorientation. In this study, Ti-Pt had ratios of 0.3 (513/1478) and 0.4 (658/1500) in the as-cast and solution heat treated conditions, indicating a low shape recovery after SHT. The low shape recovery after SHT was associated with the small difference between the detwinning and yield stress. In addition, the increased volume fraction of Ti_3Pt and Ti_5Pt_3 phases observed in Figure 4.1.1 might have had an adverse effect on the shape memory behaviour of Ti-Pt. The possibility of dislocations forming along the other phase particle-matrix interface is high [76], especially as the martensite matrix required higher stress for detwinning. The higher stresses might have locally initiated slip deformation near the other phase particle-matrix interface, which would hinder the reverse martensitic transformation process necessary for recovering the strain. Hence, there was a substantial reduction in the shape recovery of the binary TiPt phase.

After deforming the binary TiPt at higher compressive strains greater than 5%, the shape memory strain and shape recovery ratios were degraded further. This was expected, since deformation at high-applied strains of 14.97% was in the plastic region of the stress-strain curve, which is associated with plastic deformation and high irrecoverable strains, resulting in low shape recoveries.

The partial substitution of Pt with V decreased the shape memory strain and shape recovery ratio of Ti-Pt at an applied compressive strain of 5% in the as-cast condition. The addition of V eliminated the typical double yielding behaviour during deformation, indicating that slip deformation would have initiated immediately after the martensite reorientation [20,76]. The early initiation of slip was believed to be the cause of poor shape recovery in these alloys [20]. It was clear from SEM-EDX observations that the volume fraction of the Ti(Pt,V) martensite reduced with increasing V contents due to the increasing volume fraction of the other phases with increasing V contents. Therefore, it was expected that a low amount of Ti(Pt,V) would accommodate only a small amount of applied strain by the martensite reorientation process resulting in a low recovery strain.

The SHT significantly improved the SRR of Ti-Pt-V alloys. Although the values were lower than in the as-cast condition, which was attributed to the increased amounts of the other phases after SHT, they were above that of the binary Ti-Pt alloy. The other phases prevented reverse martensitic transformation, causing low shape recovery [75].

The replacement of Ti with 6.25 at.% V increased the shape memory strain and shape recovery of Ti-Pt, which was associated with low irrecoverable strain. This was attributed to the low volume fraction of the other phases in the alloy, indicating high amounts of the (Ti,V)Pt martensite phase which was able to accommodate the applied strain. The volume fraction of the other phases had increased in amount and size with the replacement of Ti with 12.5 at.% V, causing a decrease in the shape memory strain and shape recovery of Ti-Pt. The shape memory strain and shape recovery ratio of Ti-Pt was significantly improved after SHT with the increasing V content . However, these values were lower than in the as-cast condition, which was attributed to the growth of the TiO phase after SHT. The growth of the other phase particles decreased the volume fraction of martensitic (Ti,V)Pt phase, resulting in low shape memory effect and shape recovery [76].

The shape memory properties were improved with the increasing V content after SHT. Therefore, it can be deduced that ternary alloying of Ti-Pt with V improved the shape memory properties.

The decrease in shape memory strain and shape recovery ratios of the binary Ti-Pt alloy after deformation of various compressive strains greater than 5% was because the applied strains were in the plastic region i.e. the region between the yield stress and fracture stress of the stress-strain curve. The plastic region is associated with higher irrecoverable strain even after heating the sample above A_f temperature. This also contributed to the decreased shape recovery ratio of all the alloys at applied strains greater than 5%. The improved shape memory strain of Ti-Pt-V and Ti-V-Pt alloys at higher deformation strains greater than 5% was attributed to the additional formation of fine internal twins through solid solution strengthening with V associated with the single yielding behaviour [88].

5.6. Summary

The effects of adding V as an alloying element on microstructure, crystal structure, martensitic transformation temperature, hysteresis, mechanical properties, shape memory effect and shape recovery was studied for Ti-Pt. Table 5-1 shows a summary of the results.

Table 5-1: Summary of the effects of ternary alloying with V on the shape memory properties of Ti-Pt alloy.

	Ti_{50}-Pt_{50}		Ti_{50}-$Pt_{43.75}$-$V_{6.25}$		Ti_{50}-$Pt_{37.5}$-$V_{12.5}$		$Ti_{43.75}$-$V_{6.25}$-Pt_{50}		$Ti_{37.5}$-$V_{12.5}$-Pt_{50}	
	As-cast	SHT	As-cast	SHT	As-cast	SHT	As-cast	SHT	As-cast	SHT
Phases	2	3	3	3	4	4	3	2	3	2
M_s temperature (^{o}C)	1015	1014	891	889	875	878	1095	1112	1296	1292
Hysteresis (^{o}C)	61	60	166	171	173	181	113	103	90	88
σ_{det} (MPa)	513±33	658±3	-	-	-	-	-	-	-	-
σ_y (MPa)	1478±24	1500±14	1518±28	1589±65	1920±16	1849±164	1550±12	1520±118	1678±91	1480±64
σ_f (MPa)	2475±257	2614±86	2463±119	2021±79	2137±100	1936±82	>2749±8	>2471±143	>2793±153	2232±67
ε_p (%)	23.4±0.03	21.8±0.1	15.6±0.1	9.8±0.01	10.6±0.4	6.1±0.02	>17.2±0.03	>14.1±0.01	>12.5±0.01	15.7±0.1
Hardness, VHN	321±5	347±10	522±11	547±13	565±13	669±15	495±25	500±23	614±14	491±15
Shape memory strain (%)	1.7	0.8	0.8	1.0	1.0	0.7	1.8	1.2	1.5	1.7
SRR (%)	83.5	31.2	83	66.7	100	67	91.5	57	81.6	66.8

5.6.1. Microstructures

The addition of V to Ti-Pt alloy resulted in multiples phases of TiPt, Ti_3Pt, $Pt(V,Ti)_3$, TiO, $(TiO)_3Pt$, Ti_4Pt_3 and Ti_5Pt_3 phases.

The partial substitution of Pt with V resulted in compositions that lie in a three-phase region, resulting in a high volume fraction of the other phases with the increasing V concentrations, and a decrease in the volume fraction of the transforming Ti(Pt,V) phase. Solution heat-treating the Ti-Pt-V alloys increased the volume fraction of the other phases, indicating a decrease of the TiPt phase at lower temperatures with the increasing V content.

The partial substitution of Ti with V was achieved since there was not a high volume fraction of the other phases with increasing V concentrations. This suggested that the composition of the alloy was not significantly shifted with increasing V concentrations, since the matrix retained a high volume fraction of the (Ti,V)Pt phase. Further SHT improved the Ti-V-Pt alloy by eliminating the interdendritic regions, resulting in a higher quantity of the transforming (Ti,V)Pt phase.

Overall, when V was replacing Ti, the volume fraction of the other phases was lower than when V was replacing Pt. Moreover, the retained (Ti,V)Pt phase consisted of higher V content than when V was substituting for Pt. This indicated that V was more soluble in Ti than Pt.

5.6.2. Structure

The XRD results revealed that all alloys had the B19 martensite phase in the matrix as the major phase. The addition of V decreased the lattice parameters of the B19 unit cell volume due to the small atomic radius of V (0.134 nm) compared to Ti (0.147 nm) and Pt (0.139 nm), causing a contraction of the unit cell.

The XRD spectra of the Ti-Pt-V alloys revealed a disappearance of some Ti(Pt,V) peaks and an increased amount of other peaks corresponding to the other phases with increasing V content, indicating a decreased amount of the transforming Ti(Pt,V) phase with the increasing V concentrations. However, the (Ti,V)Pt peaks of Ti-V-Pt alloys did not disappear with increasing V content, suggesting that the formation of the (Ti,V)Pt phase was promoted with increasing V contents.

5.6.3. Martensitic transformation temperature and thermal hysteresis

The martensitic transformation temperature determines the application temperature of a material. Table 5-1 shows that the partial substitution of Pt with V decreased the martensitic transformation temperature of Ti-Pt with the increasing V content, while the partial substitution of Ti with V increased the martensitic transformation temperature. This was attributed to the fact that the partial substitution of Pt with V stabilises the B2 cubic phase and the partial substitution of Ti with V stabilises the B19 martensite phase. Therefore, the former does not promote the formation of the B19 martensite phase, but the latter promotes the formation of the B19 martensite phase.

The addition of V to Ti-Pt widened the thermal hysteresis with increasing V content. However, the replacement of Pt with V exhibited the largest thermal hysteresis, which was attributed to the high volume fraction of the other phases with increasing V content.

5.6.4. Mechanical properties

The addition of V eliminated the double yielding behaviour of the binary Ti-Pt SMA and exhibited a single yielding behaviour indicating an occurrence of simultaneous slip deformation along with the martensite reorientation process. The yield strength and Vickers hardness of the Ti-Pt alloy was increased by solid solution and precipitation strengthening with the addition of V. Table 5-1 shows that the partial substitution of Pt with V exhibited higher yield strength, which increased with the increasing V concentrations. However, the higher yield strength was associated with a decrease in plastic strain with increasing V content, indicating a deterioration in the ductility of the alloy. The brittleness of Ti-Pt-V got worse with increasing V contents up to a point where there was no clear difference between the yield strength and fracture strength Ti_{50}-$Pt_{37.5}$-$V_{12.5}$, i.e. no work hardening was observed. The high volume fraction of the other phases with increasing V concentrations was responsible for the brittleness of the material.

Although the plastic strains of Ti-V-Pt alloys could not be determined according to the ASTM standards due to the sample size limitation, compression tests were carried out and. The plastic strains were higher compared to Ti-Pt-V alloys, suggesting that the replacement for Ti improved the ductility of the alloys. The high volume fraction of (Ti,V)Pt martensite matrix with a low volume fraction of the other phases was responsible for the improved ductility

5.6.5. Shape memory behaviour

The partial substitution of Ti with V achieved better shape memory effect and shape recovery than when V was replacing Pt. The microstructures had a substantial influence on the shape memory behaviour of these alloys. The partial substitution of Pt with V was associated with the highest volume fraction of the other phases, hence, the lowest shape memory behaviour. The addition of V significantly improved the shape memory behavior of Ti-Pt alloys after SHT. The 100 % strain recovery ratio of Ti-Pt_{50}-$V_{12.5}$ was because at applied deformation strain of 5 %, the alloy was in the elastic region of the stress-strain curve.

Overall, the results suggested that the partial substitution of Ti with 6.25 and 12.5 at.% V was the most viable option for further development, as it exhibited higher transformation temperatures with the increasing V contents and better shape memory behaviour. Further work should evaluate the shape memory properties of the alloy at higher temperatures above the A_f temperature.

CHAPTER 6: CONCLUSIONS

The effects of ternary alloying with 0 to 12.5 at.% V on the shape memory properties of as-cast and solution heat-treated Ti-Pt alloy were investigated and the observations can be summarized as follows:

- The addition of V resulted in multiple phase microstructures. The partial substitution of Pt with V resulted in a two and three-phase region while the partial substitution of Ti with V resulted in a single-phase region. Despite these differences, both alloys consisted of B19 TiPt as a major phase in the matrix.

- The formation of B19 martensite phase was observed in all alloys. The lattice parameters of the B19 TiPt phase decreased with increasing V concentrations. The SHT and ice water quenching of the alloys from high temperatures increased the lattice parameters of the B19 martensite phase.

- The partial substitution of Pt with V reduced the martensitic transformation temperature of the alloy due to the stabilization of the B2 cubic phase, while the partial substitution of Ti with V increased the transformation temperatures of the alloy due to the stabilization of the B19 martensite phase. The thermal hysteresis was widened by the addition of V, thus limiting its actuation applications.

- The typical double yielding behaviour of Ti-Pt was eliminated by the addition of V. The addition of V increased the yield strength and hardness of Ti-Pt alloy with increasing V concentrations. The addition of V decreased the ductility of the Ti-Pt alloy, with the partial substitution of Pt with V exhibiting the worst.

- The partial substitution of Pt with V decreased the shape memory strain and shape recovery in the as cast condition but they were significantly improved after solution heat treatment. The partial substitution of Ti with 6.25 at.% V increased the shape recovery of the Ti-Pt in both the as cast and solution heat treated conditions. The shape memory effect of Ti-Pt deteriorated with the application of higher strains greater than 5%. However, the addition of V improved the shape memory properties at higher applied strains. The partial substitution of Ti with V exhibited better shape memory effect than Pt.

CHAPTER 7: RECOMMENDATIONS

The following areas could be considered for further investigation of Ti-Pt-V and Ti-V-Pt shape memory alloys:

- TEM study of all Ti-Pt-V and Ti-V-Pt alloys is critical in order to determine the composition of the phases and investigate the kind of martensite plates forming in the alloys.
- TEM study on the formation of the LP structure in binary Ti_{50}-Pt_{50} alloy.
- A study of high temperature mechanical and shape memory properties.

CHAPTER 8: RESEARCH CONTRIBUTIONS

This research will add to the available literature on high temperature SMAs and possibly broaden the application range of PGMs through research and development of SMAs that can be potentially used in high temperature environments with good and acceptable properties.

CHAPTER 9: REFERENCES

[1] Inman D . 2007 Smart materials and Structures *Mechanical Vibration: Where do we stand?* (Springer, Vienna) pp 139–49

[2] Kamila S 2013 Introduction, classification and applications of smart materials: An overview *Am. J. Appl. Sci.* **10** 876–80

[3] Bozzoloabi G, Noebeb R D, Mosca H and Glenn N 2018 *Site preference of ternary alloying additions to NiTi :*

[4] Lin H-C, Lin K M, Lin C-S and Chang S K 1999 A study of TiNiV ternary shape memory alloys *J. Alloys Compd.* **284** 213–7

[5] Ma L W, Cheng H S, Cao C W and Chung C Y 2012 Study of thermal scanning rates on transformations of Ti-19Nb-9Zr (at.%) by means of Differential Scanning Calorimetry analysis *J. Mater. Eng. Perform.* 2675–9

[6] Jani J M, Leary M, Subic A and Giibson M A 2014 A review of shape memory alloy research , applications and opportunities *Mater. Des.* **56** 1078–113

[7] Calkins F T and Mabe J H 2007 Variable Geometry Jet Nozzle Using Shape Memory Alloy Actuators

[8] Oehler S D, Hartl D J, Lopez R, Malak R J and Lagoudas D C 2012 Design optimization and uncertainty analysis of SMA morphing structures *Smart Mater. Struct.* **21**

[9] Hartl D J and Lagoudas D C 2007 Aerospace applications of shape memory alloys *Proc. Inst. Mech. Eng. Part G J. Aerosp. Eng.* **221** 535–52

[10] Hwan S, Tae J, Jin H, Seok Y, Yoo J, Sang Y, Ram K, Hwee C, Man J and Buem K 2017 In fluence of Zr content on phase formation , transition and mechanical behavior of Ni-Ti-Hf-Zr high temperature shape memory alloys *J. Alloys Compd.* **692** 77–85

[11] Canadinc D, Trehern W, Karaman I, Sun F and Chaudhry Z 2019 Ultra-high temperature multi-component shape memory alloys *Scr. Mater.* **158** 83–7

[12] Bozzolo G, Mosca H O and Noebe R D 2007 Phase structure and site preference behavior of ternary alloying additions to PdTi and PtTi shape-memory alloys *Intermetallics* **15** 901–11

[13] Karakoc O, Hayrettin C, Bass M, Wang S J, Canadic D, Mabe J H, Lagoudas D C and Karaman I 2017 Effects of upper cycle temperature on the actuation fatigue response of NiTiHf high temperature shape memory alloys *Acta Mater.* **138** 185–97

[14] Benafan O, Gaydosh D J, Noebe R D, Qiu S and Vaidyanathan R 2016 In Situ Neutron Diffraction Study of NiTi–21Pt High-Temperature Shape Memory Alloys *Shape Mem. Superelasticity* **2** 337–46

[15] Ramaiah K V, Saikrishna C N, Sujata M and Bhaumik S K 2013 Ni30 Ti50 Pt20 High Temperature Shape Memory Alloy (HTSMA) Wires : Processing Related Issues *J. ISSS* **2** 1–9

[16] Padulla II S, Bigelow G, Noebe R, Gaydosh D and Garg A 2019 Challenges and Progress in the Development of High-Temperature Shape Memory Alloys Based on NiTiX Compositions for High-Force Actuator Applications

[17] Rios O, Noebe R, Biles T, Garg A, Palczer A, Scheiman D, Seifert H J and Kaufman M 2005 Characterization of ternary NiTiPt high-temperature shape memory alloys *Smart Structures and Materials 2005: Active Materials: Behavior and Mechanics* vol 5761 p 376

[18] Saghaian S M, Karaca H E, Souri M, Turabi A S and Noebe R D 2016 Tensile shape memory behavior of Ni50.3Ti29.7Hf20 high temperature shape memory alloys *Mater. Des.* **101** 340–5

[19] Wadood A and Yamabe-mitarai Y 2014 TiPt-Co and TiPt-Ru high temperature shape memroy alloys *Mater. Sci. Eng. A* **601** 106–10

[20] Yamabe-Mitarai Y, Arockiakumar R, Wadood A, Suresh K S, Kitashima T, Hara T, Shimojo M, Tasaki W, Takahashi M, Takahashi S and Hosoda H 2015 Ti(Pt, Pd, Au) based high temperature shape memory alloys *Mater. Today Proc.* **2S** S517–22

[21] Chikosha S, Mahlatji M, Modiba R and Chikwanda H 2018 The effect of vanadium on structure and martensitic transformation temperature of TiPt alloy *Conference of the South African Advanced Materials Initiative (COSAAMI-2018)*

[22] Yamabe-mitarai Y, Hara T, Miura S and Hosoda H 2012 Phase transformation and shape memory effect of Ti(Pt, Ir) *Metall. Mater. Trans. A Phys. Metall. Mater. Sci.* **43** 2901–11

[23] Yamabe-Mitarai Y, Hara T, Miura S and Hosoda H 2006 Mechanical properties of Ti-50(Pt,Ir) high-temperature shape memory alloys *Mater. Trans.* **47** 650–7

[24] Wadood A, Takahashi M, Takahashi S, Hosoda H and Yamambe-Mitarai Y 2013 High temperature mechanical and shape memory properties of TiPt-Zr and TiPt-Ru alloys *Mater. Sci. Eng. A* **564** 34–41

[25] Tello E K A 2012 *Phase transformations and equilibria of titanium platinum alloys the composition range 30-50 atomic percent platinum*

[26] Kousbroek R 2018 Shape memory alloys *Met. Ceram. Biomater. Vol. II Strength Surf.* **2** 63–90

[27] Christian J . 2002 Shape memory alloys

[28] Chang L C and Read T A 1951 Plastic Deformation and Diffusionless Phase Changes in Metals — the Gold-Cadmium Beta Phase *Jom* **3** 47–52

[29] Greninger A B and Troiano A R 1938 Orientation habit of martensite *Nature* **141**

[30] Kurjumov G . and Khandros L . 1949 First reports of the thermoelastic behaviour of the martensitic phase of Au-Cd *Dokl. Akad. Nauk SSSR* **66** 211–3

[31] Kumar P K and Lagoudas D C 2008 Introduction to Shape Memory Alloys Available in https://pdfs.semanticscholar.org/b1a5/2186ffaeef6009a47c71a492051e07ca5fdb.pdf [Consultation in jun. 4 (2018)]

[32] Buehler W, Gilfrich J and Riley R 1963 Effect of low temperature phase changes on the mechanical properties of alloys near composition Ti-Ni *J. Appl. Phys.* **34**

[33] Song C 2010 History and Current Situation of Shape Memory Alloys Devices for Minimally Invasive Surgery *Open Med. Devices J.* **2** 24–31

[34] Yamabe-Mitarai Y, Hara T, Kitashima T, Miura S and Hosoda H 2013 Composition dependence of phase transformation behavior and shape memory effect of Ti(Pt, Ir) *J. Alloys Compd.* **577** S399–403

[35] Arockiakumar R, Takahashi M, Takahashi S and Yamabe-mitarai Y 2013 Microstructure , mechanical and shape memory properties of Ti – 55Pd – 5 x (x ¼ Zr , Hf , V , Nb) alloys *Mater. Sci. Eng. A* **585** 86–93

[36] Tello K E, Noebe R D, Garg A, Allaz J and Kaufman M J 2017 Materials Characterization Revisiting the Ti-Pt system relevant to high temperature shape memory alloys **130** 97–104

[37] Biggs T, Cortie M B, Witcomb M J and Cornish L A 2001 Martensitic Transformations , Microstructure , and Mechanical Workability of TiPt *Metall. Mater. Trans. A* **32 A** 1881–6

[38] Olson G B and Cohen M 1982 Stress assisted isothermal martensitic transformation : application to TRIP steels *Metall. Mater. Trans. A* **A13** 1907–14

[39] Hodgson D E, Wu M H and R.J B 1990 Shape memory alloys *Metals Handbook* vol 2 (Ohio: ASM International) pp 897–902

[40] Kurdyumov G and Khandros L 1949 First reports of the thermoelastic behaviour of the martensitic phase of Au-Cd alloys *Dokl. Akad. Nauk SSSR* **66** 211–4

[41] Biggs T, Cortie M B, Witcomb M J and Cornish L A 2003 Platinum Alloys for Shape Memory Applications *Platin. Met. Rev.* **47** 142–56

[42] Otsuka K and Ren X 1999 Recent developments in the research of shape memory alloys *Intermetallics* **7** 511–28

[43] Liu Y and McCormick P . 1996 Criteria of transformation sequence in NiTi shape memory alloys *Mater. Trans.* **37** 691–6

[44] Salzbrenner R J and Cohen M 1979 On the thermodynamics of thermoelastic martensitic transformations *Acta Metall.* **27** 739–48

[45] Yoneyama T and Shuchi Miyazaki 2009 *Shape memory alloys for biomedical applications*

[46] Biggs T, Cornish L A, Witcomb M J and Cortie M B 2004 Revised phase diagram for the Pt-Ti system from 30 to 60 at.% platinum *J. Alloys Compd.* **375** 120–7

[47] Sehitoglu H, Hamilton R, Maier H J and Chumlyakov Y 2004 Hysteresis in NiTi alloys *J. Phys.* **IV** 3–10

[48] Duffy K P, Padula S A and Scheiman D A 2015 Damping of high-temperature shape memory alloys

[49] Dezfuli F H and Alam M S 2013 Shape memory alloy wire-based smart natural rubber bearing *Smart Mater. Struct.* **4**

[50] Browne A L SMA heat engine : Advancing from a scientific curiosity to a SMA heat engines

[51] Oltmans B and Oltmans B A 2000 A Study of the effects of strain on NiTi shape memory alloy

[52] Hideo Nishimura and Tsuyoshi Hiramatsu 1957 On The Corrosion Resistance of Titanium Alloys(2nd Report). Diagram of the Titaniu. m—Platinum System. 469–73

[53] Pietrokowski P 1965 Novel ordered phases *Nature* **206** 291–291

[54] Junod A, Flukiger R and Muller J 1976 Supraconductivite et chaleur specifique dans les alliages A15 a base de titane *J. Phys. Chem. Solids* **37** 27–31

[55] Donkersloot H . and Van Vucht J H . 1970 Martensitic transformations in gold-titanium, palladium-titanium and platinum-titanium alloys near the equiatomic composition *J. less common Met.* **20** 83–91

[56] Dwight A E, Conner Jnr R A and Downey J W 1965 Equiatomic compounds of the transition and lanthanide elements with Rh, Ir, Ni and Pt *Acta Crystallogr.* **18** 835–9

[57] Murray J . 1982 The Pt-Ti (Platinum-Titanium) System *Bull. Alloy phase diagrams* **3** 329–35

[58] Li M, Han W and Li C 2008 Thermodynamic assessment of the Pt–Ti system *J. Alloys Compd.* **461** 189–94

[59] Ball S C 2005 *Electrochemistry of Proton Conducting Membrane Fuel Cells* vol 49

[60] Cornish L A, Shongwe M B, Odera B, Odusote J K, Witcomb M K, Chown L H, Rading G O and Papo M J 2012 Update on the Development of Platinum-Based Alloys for Potential High-Temperature Applications *South African Inst. Min. Metall.*

[61] Ansara I, Dinsdale A T and Rand M H 1998 *Thermochemical database for light metal alloys* vol 2, ed I Ansara, A . Dinsdale and M . Rand (Luxembourg : Office for Official Publication of the European Communiies)

[62] Kostov A, Zivkovic D and Friedrich B 2006 Thermodynamic study of Ti-V and Al-V systems using FactSage *J. Min. Metall. Sect. B Metall.* **42** 57–65

[63] Chinnappan R, Panigrahi B K and van de Walle A 2016 First-principles study of phase equilibrium in Ti–V, Ti–Nb, and Ti–Ta alloys *Calphad Comput. Coupling Phase Diagrams Thermochem.* **54** 125–33

[64] Biggs T, Cortie M B, Witcomb M J and Cornish L A 2001 Martensitic transformations, Microstructure, and mechanical workability of TiPt *Metall. Mater. Trans. A* **32A** 1881–6

[65] Rotaru G M, Tirry W, Sittner P, Van Humbeeck J and Schryvers D 2007 Microstructural study of equiatomic PtTi martensite and the discovery of a new long-period structure *Acta Mater.* **55** 4447–54

[66] Yamabe-Mitarai Y, Hara T, Miura S and Hosoda H 2010 Shape memory effect and pseudoelasticity of TiPt *Intermetallics* **18** 2275–80

[67] Mamiko K, Madoka T, Satoshi T and Yamabe-Mitarai Y 2012 Effect of Zr on phase transformation and high temperature shape memory effect in TiPd alloys *Mater. Lett.* **89** 336–8

[68] Chastaing K, Vermaut P, Ochin P, Segui C, Laval J Y and Portier R 2006 Effect of Cu and Hf additions on NiTi martensitic transformation **440** 661–5

[69] Zhang Y M, Yang S and Evans J R G 2008 Revisiting Hume-Rothery's Rules with artificial neural networks *Acta Mater.* **56** 1094–105

[70] Chen H R 2010 Shape memory alloys: Manufacture, properties and applications *Shape Mem. Alloy. Manuf. Prop. Appl.* 1–546

[71] Bozzolo G, Mosco H . and Noebe R . 2007 Phase structure and site preference behavior of ternary alloying additions to PdTi and PtTi shape-memory alloys *Intermetallics* **15** 901–11

[72] Mashamaite M P, Chauke H R and Ngoepe P E 2018 Mechanical properties and stability of TiPt-M (M = Ru, Co, Cu, Zr and Hf) for high temperature applications *IOP Conf. Ser. Mater. Sci. Eng.* **430**

[73] Quin M . 1985 United States patent钻石打标专利 *Geothermics* **14** 595–9

[74] Yamauchi K, Sato S and Takaara H 1990 United States patent钻石打标专利 *Geothermics* **14** 595–9

[75] Yamabe-mitarai Y 2017 Development of high-temperature shape memory alloys above 673 K *Mater. Sci. Forum* **879** 107–12

[76] Arockiakumar R, Takahashi M, Takahashi S and Yamabe-Mitarai Y 2013 Microstructure, mechanical and shape memory properties of Ti-55Pd-5x (x=Zr, Hf, V, Nb) alloys *Mater. Sci. Eng. A* **585** 86–93

[77] Modiba R, Baloyi E, Chikosha S, Chauke H . and Ngoepe P E 2018 Computational

modelling of Ti50Pt50Vx potential shape memory alloy *Conference of the South African Advanced Materials Initiative (COSAAMI-2018)*

[78] Cotton S A 2005 Titanium, zirconium and hafnium *Annu. Reports Prog. Chem. - Sect. A* **101** 139–48

[79] Zhao J C 2007 *Methods for phase Diagram determination* ed J.C. Zhao (USA: Elsevier B.V.)

[80] Biggs T 2001 *An investigation into displacive transformations in platinum alloys* (University of the Witwatersrand)

[81] Yamabe-Mitarai Y, Takebe W and Shimojo M 2017 Phase Transformation and Shape Memory Effect of Ti–Pd–Pt–Zr High-Temperature Shape Memory Alloys *Shape Mem. Superelasticity* **3** 381–91

[82] Otsuka K and Ren X 2005 Physical metallurgy of Ti-Ni based shape memory alloys *Prog. Mater. Sci.* **50** 511–678

[83] Kim W C, Kim Y J, Kim J S, Kim Y S, Na M Y, Kim W T and Kim D H 2019 Correlation between the thermal and superelastic behavior of Ni 50-x Ti 35 Zr 15 Cu x shape memory alloys *Intermetallics* **107** 24–33

[84] Evirgen A, Karaman I, Santamarta R, Pons J, Hayrettin C and Noebe R D 2016 Relationship between crystallographic compatibility and thermal hysteresis in Ni-rich NiTiHf and NiTiZr high temperature shape memory alloys *Acta Mater.* **121** 374–83

[85] Atli K C, Karaman I and Noebe R D 2014 Influence of tantalum additions on the microstructure and shape memory response of Ti50.5Ni24.5Pd25 high-temperature shape memory alloy *Mater. Sci. Eng. A* **613** 250–8

[86] Frenzel J, Wieczorek A, Opahle I, Maab B, Drautz R and Eggeler G 2015 On the effect of alloy composition on martensite start temperatures and latent heats in Ni-Ti-based shape memory alloys *Acta Mater.* **90** 213–31

[87] Yamabe-Mitarai Y, Takebe W and Shimojo M 2017 Phase Transformation and Shape Memory Effect of Ti–Pd–Pt–Zr High-Temperature Shape Memory Alloys *Shape Mem. Superelasticity* **3** 381–91

[88] Hong S H, Kim J T, Park H J, Kim Y S, Suh J Y, Na Y S, Lim K R, Shim C H, Park J M and Kim K B 2017 Influence of Zr content on phase formation, transition and mechanical behavior of Ni-Ti-Hf-Zr high temperature shape memory alloys *J. Alloys Compd.* **692** 77–85

[89] Saha S, Tareq S . and Galib R . 2016 Effect of Overageing Conditions on Microstructure and Mechanical Properties in Al–Si–Mg Alloy *J. Mater. Sci. Eng.* **5**